

Technische Universität München
TUM School of Engineering and Design

Investigation of Ammonia as Fuel for High-Pressure Direct Injection Combustion

Valentin Johannes Scharl

Vollständiger Abdruck der von der TUM School of Engineering and Design
der Technischen Universität München zur Erlangung eines

Doktors der Ingenieurwissenschaften (Dr.-Ing.)

genehmigten Dissertation.

Vorsitz:

Prof. Dr. Thomas Hamacher

Prüfer der Dissertation:

Prof. Dr.-Ing. Thomas Sattelmayer

Prof. Dr.-Ing. Bert Buchholz

Prof. Dr. David R. Emberson

Die Dissertation wurde am 29.11.2023 bei der Technischen Universität München
eingereicht und durch die TUM School of Engineering and Design am 08.04.2024
angenommen.

Vorwort

Die vorliegende Dissertation entstand während meiner Forschungstätigkeit am Lehrstuhl für Thermodynamik der Technischen Universität München. Sie wurde vom Bundesministerium für Wirtschaft und Klimaschutz im Rahmen des Verbundprojekts "AmmoniaMot - Regenerativ erzeugtes Ammoniak als Kraftstoff der Zukunft für Marine-Verbrennungsmotoren" (Förderkennzeichen: 03SX534D) gefördert. Ich danke den Verbundpartnern MAN Energy Solutions, Neptun Ship Design, Woodward L'Orange und WTZ für die freundliche und erfolgreiche Zusammenarbeit.

Mein besonderer Dank gilt Prof. Thomas Sattelmayer für die Betreuung meiner Arbeit. Ich schätze das mir entgegengebrachte Vertrauen und die Freiheit, die er mir bei der Gestaltung des Forschungsprojekts ließ. Gleichzeitig haben mir die technischen Diskussionen und Besprechungen die entscheidenden Impulse für die erfolgreiche Forschungsarbeit gegeben.

Ich danke Prof. Bert Buchholz und Prof. David Emberson für die inhaltliche Begutachtung und Prof. Thomas Hamacher für die Übernahme des Prüfungsvorsitzes.

Ebenso möchte ich den Mitarbeitern des Lehrstuhls für Thermodynamik für Ihre Unterstützung und Zusammenarbeit danken. Insbesondere danke ich Utkarsh Pathak und Dominik Krnac für die freundschaftliche Zusammenarbeit im Projekt. Auch Christoph Hirsch möchte ich für seine handwerkliche und wissenschaftliche Unterstützung danken. Vielen Dank auch an meine ehemaligen Studenten Quentin Daxenberger, Tomislav Lackovic, Tjabbo Reinhardus und Shane Martin, die mich tatkräftig im Labor unterstützt haben.

Abschließend danke ich von ganzem Herzen meiner Familie und Anita. Ohne eure Unterstützung wäre diese Arbeit nicht möglich gewesen.

München, November 2023

Valentin Scharl

Abstract

Ammonia is a carbon-free alternative to fossil fuels. However, its unfavorable combustion characteristics and propensity to form nitrogen oxides challenge its use as a fuel for internal combustion engines. This work investigates the pilot-ignited combustion of ammonia sprays under conditions relevant to engines. Scrutinizing the impact of ammonia's physical properties and combustion chemistry on combustion behavior and pollutant formation reveals the main challenges for ammonia spray combustion. Experiments in a single-shot engine prove the combustion process's feasibility and reveal a strong dependence of ammonia combustion on the interaction with the pilot injection. Investigations of the flame's spectral footprint distinguish the contributions of pilot fuel and ammonia to combustion. Further optical studies show that the ammonia flame cannot self-stabilize and drifts off from the injector nozzle after ignition by the pilot injection. A validated spray model attributes the lack of flame stabilization to low temperatures and equivalence ratios within the ammonia spray. The work discusses implications on engine operation, draws conclusions on the flame stabilization mechanism, and relates the non-stabilized flame to ammonia combustion's strong dependence on pilot interaction. The extensive lift-off length, resulting from the drifting ammonia flame, motivates pilot fuel intermediate or post-injections (PIs), which significantly reduce unburned ammonia emissions.

Kurzfassung

Ammoniak ist eine kohlenstofffreie Alternative zu fossilen Kraftstoffen. Seine ungünstigen Verbrennungseigenschaften und seine Neigung zur Bildung von Stickoxiden stellen jedoch eine Herausforderung für seine Verwendung als Kraftstoff für Verbrennungsmotoren dar. In dieser Arbeit wird die pilotgezündete Verbrennung von Ammoniaksprays unter motorrelevanten Bedingungen untersucht. Die Auswirkungen der physikalischen Eigenschaften von Ammoniak und der Verbrennungschemie auf das Verbrennungsverhalten sowie die Schadstoffbildung zeigen die größten Herausforderungen für die Verbrennung von Ammoniaksprays auf. Experimente in einer Einhubmaschine beweisen die Machbarkeit des Verbrennungsprozesses und offenbaren eine starke Abhängigkeit der Ammoniakverbrennung von der Interaktion mit der Piloteinspritzung. Untersuchungen des spektralen Fußabdrucks der Flamme unterscheiden die Beiträge von Pilotbrennstoff und Ammoniak zur Verbrennung. Weitere optische Untersuchungen zeigen, dass die Ammoniakflamme sich nicht selbst stabilisieren kann und nach der Zündung durch die Piloteinspritzung von der Einspritzdüse abdriftet. Ein validiertes Spraymodell führt die fehlende Flammenstabilisierung auf niedrige Temperaturen und Äquivalenzverhältnisse innerhalb des Ammoniaksprays zurück. Die Arbeit erörtert die Auswirkungen auf den Motorbetrieb, zieht Schlussfolgerungen zum Mechanismus der Flammenstabilisierung und verbindet die nicht stabilisierte Flamme mit der starken Abhängigkeit der Ammoniakverbrennung von der Piloteinspritzung. Die aus der driftenden Ammoniakflamme resultierende lange Abhebelänge motiviert die Zwischen- oder Nacheinspritzung von Pilotkraftstoff, die die unverbrannten Ammoniakemissionen deutlich reduziert.

Previous Publications

Parts of this thesis were published by the author in conference proceedings and journal papers [1–6] beforehand. All of these prior printed publications are registered according to the valid doctoral regulations. However, not all of them are quoted explicitly, as they are part of the work presented here. Whether these publications were referenced, depends on maintaining comprehensibility and providing context, where necessary.

Contents

Contents	vi
List of Figures	ix
List of Tables	xv
Nomenclature	xvi
1 Introduction	1
1.1 Background	1
1.2 Research Objectives and Thesis Outline	3
2 Fundamentals	7
2.1 Fuel Injection and Mixture Formation	7
2.2 Phenomenological Description of Diesel Combustion	12
2.3 Flame Stabilization	15
2.3.1 Flame Stabilization by Flame Propagation	16
2.3.2 Flame Stabilization by Auto-Ignition	17
2.4 Pollutant Formation	20
2.5 Chemiluminescence	22
3 Characterization of Ammonia as High-Pressure Direct Injection Fuel	27
3.1 Mixture Formation	28
3.2 Flame Stabilization	30
3.3 Ammonia Oxidation Pathways	32
3.4 Pollutant Formation Characteristics	34

3.5	Challenges for Ammonia Spray Combustion	41
4	Experimental Setup	43
4.1	Rapid Compression Expansion Machine	43
4.2	Fuel Injection	46
4.3	Optical Measurement Setup	50
4.3.1	Shadowgraphy Imaging	50
4.3.2	OH* Chemiluminescence Imaging	52
4.3.3	Mie-Scattering Imaging	53
4.3.4	Spectroscopy	54
4.4	Exhaust Gas Analysis	54
4.5	Controls and Data Acquisition	58
4.6	Uncertainty	60
5	Methods	63
5.1	Thermodynamic Model	63
5.2	Image Processing	66
5.2.1	Shadowgraphy and Mie-Scattering	66
5.2.2	Simultaneous SG and OH* CL	68
5.2.3	Spectroscopy	70
5.3	Spray Model	73
6	Ignition and Pilot Interaction Requirements	77
6.1	Geometrical Arrangement and Injection Timing	77
6.2	Charge Conditions	82
6.3	Pilot Characteristics	83
7	Optical Characterization	86
7.1	Integral Flame Spectra	87
7.2	Temporal and Spatial Evolution of Flame Emissions	90
7.3	Temporal Evolution of Background Corrected Intensities	95
8	Mixture Formation and Flame Stabilization	99
8.1	Mixture Formation Model Validation	99
8.2	Combustion Experiments	101
8.3	Mixture Formation	105

CONTENTS

8.4	Spray Stabilization by Auto-Ignition	107
8.5	Implications on Combustion Characteristics and Pollutant Formation	109
9	Diesel Fuel Post-Injections	112
9.1	Lift-Off Length Evolution	112
9.2	Ammonia Conversion	114
9.3	Pollutant Formation	117
10	Summary and Conclusions	122
A	Engineering Correlation on Liquid Lengths of Arbitrary Fuels	144
B	Fuel Injection Velocity Profiles	146

List of Figures

2.1	Scheme of nozzle flow, spray breakup, and spray penetration of a diesel spray. Adapted from [7].	8
2.2	Schematic of a control volume used to derive basic spray properties. Adapted from [8].	10
2.3	Schematic of a conceptual model for conventional diesel combustion. Adapted from [9].	14
2.4	Schematic of flame stabilization by a triple flame. Adapted from [10].	17
2.5	Schematic of the lift-off stabilization mechanism after an upstream ignition event. Adapted from [11].	19
2.6	$\Phi - T$ map showing air pollutant forming conditions (NO, C ₂ H ₂) for the combustion of n-heptane at 120 bar after 2 ms residence time. The lines indicate the states resulting from mixing and adiabatic combustion in the RCEM at OP4 after fuel injection at 293 K.	21
2.7	Schematic of energy levels of a diatomic molecule. Each electronic state (e.g. A or X) is divided into vibrational states (v' or v'') and rotational states (not shown). The blue transition arrow indicates the A-X(0,6) electron transition. Adapted from [12].	23
2.8	Emission bands from selected electrochemically excited species occurring in ammonia and hydrocarbon flames. Adapted from [13].	25
3.1	Scheme of a reaction pathway diagram for ammonia oxidation. Adapted and extended from [14].	32

LIST OF FIGURES

3.2	$\Phi - T$ maps showing air pollutant forming conditions (NO, N ₂ O) for the combustion of ammonia at 120 bar after 2 ms residence time. The lines indicate the states resulting from mixing and adiabatic combustion of ammonia and air. Mixing and adiabatic combustion lines are included for charge air temperatures of 820 K, 920 K (thick line), and 1020 K at a fuel injection temperature of 293 K (left), and fuel injection temperatures of 293 K (thick line), 343 K, and 393 K at a charge air temperature of 920 K (right).	36
3.3	$\Phi - T$ map showing NO concentrations in thermodynamic equilibrium for ammonia combustion.	37
3.4	$\Phi - T$ map showing 500 ppm iso-lines for N ₂ O (left) and NO (right) for charge pressures of 10 bar, 50 bar, 200 bar (top) and residence times of 0.1 ms, 0.5 ms, 4 ms (bottom).	39
4.1	RCEM driving system: ① driving-air bottles, ② driving piston, ③ hydraulic fluid, ④ flow orifice, ⑤ working piston, ⑥ combustion chamber, ⑦ cylinder head.	44
4.2	Cylinder head: ① diesel injector, ② ammonia injector, ③ inner eccentric, ④ outer eccentric, ⑤ pressure transducer, ⑥ mirror, ⑦ reduction ring.	47
4.3	Ammonia injection system: ① intermediate storage tank, ② ammonia pump, ③ ammonia injector, ④ back-pressure valve, ⑤ acid trap.	50
4.4	SG, MS, and CL optical setup: ① xenon arc lamp, ② UV filter, ③ pin hole, ④ concave mirror, ⑤ planar mirror, ⑥ quartz-glass piston, ⑦ cylinder head with mirror, ⑧ beam splitter, ⑨ focusing lens, ⑩ bandpass filter, ⑪ image intensifier, ⑫ high-speed camera (CL), ⑬ high-speed camera (SG/MS), ⑭ continuous laser 532nm, ⑮ sheet-forming optics, ⑯ planar mirror, ⑰ 45° mirror.	51
4.5	Schematic of an SG setup and its working principle. Adapted from [15].	52
4.6	High-speed spectroscopy setup: ① UV lens, ② monochromator, ③ image intensifier, ④ high-speed camera.	55

4.7	Scheme of the exhaust gas analysis system.	56
4.8	Exemplary piston position (blue) and combustion chamber pressure curves (orange) for an experiment in the RCEM. The figure indicates the measurement range and trigger criteria.	59
5.1	Scheme of the thermodynamic model of the combustion chamber indicating the different zones, mass transfer, and heat loss.	64
5.2	Determination of key figures from the HRR and injected mass fluxes.	65
5.3	Procedure for determining gaseous and liquid spray penetration from SG (top) and MS (bottom) images.	67
5.4	Procedures for superimposing SG and OH* CL images. Top: Transferring the entire information of both images using a 2-D color map. Bottom: Transferring the SG spray contour onto the OH* CL images.	69
5.5	Spectroscopy raw image of the light emitted by the mercury arc lamp obtained with grating 3 (top left), corresponding intensity plotted over the pixel scale of the light emitted by the mercury arc lamp (bottom left), and conversion rule from the pixel scale to the wavelength scale for the setup used (right).	71
5.6	Reference spectrum of a calibrated halogen lamp, measured spectrum, and calibration factor of the setup employed.	71
5.7	Typical CL spectrum of ammonia combustion. Left: UV range obtained using grating 2, right: UV-VIS range obtained using grating 3. The colored peak areas represent the background corrected CL intensity of the corresponding species.	72
5.8	Schematic of the 1-D model. Adapted from [16].	74
5.9	Approximated injection velocity profiles vs. injection velocity profile from experimental volume flux measurements for the three nozzles investigated at OP4.	75
6.1	Relative burnout rate for different interaction angles α and relative injection timings for 10 mg (left) and 5 mg (right) diesel pilots.	79

LIST OF FIGURES

6.2	Pilot, main, and relative ignition delay for different interaction angles α and relative injection timings for 10 mg (left) and 5 mg (right) diesel pilot injections.	81
6.3	Fuel mass flux and averaged apparent HRRs for different operating points with slightly advanced (+500 μ s) 10 mg diesel injections and converging sprays ($\alpha = -7.5^\circ$).	83
6.4	Diesel mass fluxes (bottom), ammonia mass flux (top), and averaged apparent HRRs (top) for different, slightly advanced (+500 μ s) diesel pilots at OP4 and converging sprays ($\alpha = -7.5^\circ$).	84
7.1	Spatially and temporally integrated spectra obtained at OP3. (a) and (b) were obtained using grating 3, while (c) was obtained using grating 2. (b) and (c) are obtained by temporal integration from 1600 – 6000 μ s after SOI, while (a) is integrated until 900 μ s after SOI.	88
7.2	HRR and mass fluxes of the investigated combustion cases featuring a slightly advanced diesel pilot injection (+500 μ s). . .	89
7.3	SG (top), OH* CL with overlaid SG contours (middle) and NL (bottom) imaging at OP3. The left section contains images taken during pilot ignition ($t = 700 - 850 \mu$ s after SOI). The right section contains images taken during the flame transition from diesel to ammonia ($t = 1000 - 1600 \mu$ s after SOI). . . .	91
7.4	SG (top), OH* CL with overlaid SG contours (middle) and NL (bottom) imaging at OP3. OH* intensities are γ -corrected ($\gamma = 0.4$). The images are taken during the main fuel combustion phase, in which ammonia is burning ($t = 2000 - 5000 \mu$ s after SOI).	92
7.5	Spatially integrated flame emission spectra at different times during diesel pilot ignition (a), the flame transition from diesel to ammonia (b), and ammonia combustion (c) at OP3.	93
7.6	Temporal evolution of background corrected CL intensities. Top: OH*, NH ₂ *, and broadband luminosity for OP3. Bottom: OH* and NH* for OP3 and OP4.	96

8.1	Experimental results at OP4 for ammonia penetration, liquid length, and spray angle, as well as model predictions for penetration and stationary liquid length for the 0.94 mm nozzle at 530 bar with an injection mass of 210 mg (left) and the 0.98 mm nozzle at 265 bar with an injection mass of 125 mg (right). . .	101
8.2	Simultaneously acquired and superimposed SG and CL images of diesel-piloted ammonia combustion at OP4 with 190 mg ammonia (injection pressure of 460 bar, 0.98 mm nozzle).	102
8.3	Normalized mean OH* intensities (top), lift-off length evolutions (top), averaged HRRs (middle), and parametrized injection mass fluxes of diesel and ammonia (bottom) for ammonia mass and injection pressures of 125 mg/265 bar, 160 mg/360 bar 190 mg/460 bar and 220 mg/560 bar.	104
8.4	Modeled equivalence ratio contours and temperature contours (top), as well as center line and radially averaged equivalence ratios and gas phase temperatures (bottom) for the ammonia sprays examined.	106
8.5	Temperature constraints for flame stabilization by auto-ignition for diesel and ammonia. ①: cold educts, owing to high latent heat of vaporization and low air entrainment in upstream regions of the spray. ②: low product temperature, owing to lean equivalence ratios in downstream regions of the spray. Adapted from [17].	108
9.1	Combined SG and CL images of four diesel fuel injection cases with an ammonia injection via the 0.75 mm nozzle. Left: No PI, middle left: PI at $t = 1.2$ ms, middle right: PI at $t = 2.2$ ms, right: PI at $t = 3.2$ ms. Blue circles indicate the first occurrence of OH* CL due to the PI.	113
9.2	HRRs and fuel mass fluxes (top), as well as lift-off lengths (bottom) of four different diesel fuel injection cases with an ammonia main injection via the 0.75 mm nozzle.	115

LIST OF FIGURES

9.3	Conversion rate of ammonia for different diesel injection cases (left: 0.98 mm nozzle with an injection pressure of 265 bar, right: 0.75 mm nozzle operated with 435 bar). The case without PI features a 10 mg diesel pilot injection, while cases with PI feature a 5 mg diesel pilot followed by a 5 mg PI.	116
9.4	Ammonia conversion rates for three different diesel fuel PI amounts (0.98 mm nozzle). The PI starts at $t = 2.2$ ms after SOI ammonia.	117
9.5	Production rates, HRRs, and fuel injection mass fluxes for 5 mg (blue) and 10 mg (orange) pilot injections without PIs, and for a 5 mg pilot injection followed by a 5 mg PI at $t = 2.2$ ms (green). (a): HRRs 0.98 mm nozzle, (b): HRRs 0.75 mm nozzle, (c): production rates 0.98 mm nozzle, (d): production rates 0.75 mm nozzle.	119
9.6	Ammonia mass and equivalence ratios over time in the spray volume between nozzle exit and lift-off length at EOI (40 mm for the 0.98 mm nozzle, 50 mm for the 0.75 mm nozzle). . . .	120
B.1	Approximated injection velocity profiles vs. injection velocity profile from experimental volume flux measurements for the investigations presented in Chapter 9.	146

List of Tables

3.1	Selected physical properties of ammonia, diesel/n-dodecane and methanol [14, 18–22]. Properties at standard conditions (293 K, 1 bar), if not specified otherwise.	27
3.2	Estimated parameters for liquid length calculations based on Higgins et al. [23] for ammonia, diesel and methanol at OP4. .	29
4.1	Investigated operating points.	46
4.2	Ammonia injection parameters.	48
4.3	Diesel injection parameters.	49
4.4	Overview of signals, sensors, and data acquisition specifications.	59
4.5	Calculated and measured injection masses for two injection cases at OP4.	62
5.1	1-D spray model input parameters.	76
A.1	Physical properties of ammonia (293 K, 10 bar), diesel (293 K, 1 bar), methanol (293 K, 1 bar). Properties from [18, 19, 22, 23].	145
A.2	Physical properties of air at TDC of OP4 [18] and parameters used for the presented engineering correlation [23].	145
B.1	1-D spray model input parameters for the investigations presented in Chapter 9.	147

Nomenclature

Abbreviations

AEGL	acute exposure guideline level
CFD	computational fluid dynamics
CL	chemiluminescence
DME	dimethyl ether
DUVRAS	differential ultra-violet resonance absorption spectroscopy
EGR	exhaust gas recirculation
EOI	end of injection
FPGA	field-programmable gate array
FWHM	full width at half maximum
HCCI	homogenous charge compression ignition
HPDF	high-pressure dual-fuel
HRR	heat release rate
IMO	International Maritime Organization
LHV	lower heating value
MS	Mie-scattering
NDIR	non-dispersive infrared
NDUV	non-dispersive ultra-violet
NL	natural luminosity
OP	operating point
PI	post-injection
rpm	revolutions per minute
RCEM	rapid compression expansion machine
RCM	rapid compression machine
SCR	selective catalytic reduction
SG	Shadowgraphy

SOI	start of injection
TDC	top dead center
UV	ultra-violet
VIS	visible

Latin Letters

a	constant factor for spray angle correction [–]
A	flow area [m ²]
c	speed of light [m/s]
c_p	specific heat at constant pressure [J/kg/K]
C	constant coefficient [–]
d_0	nozzle diameter [m]
h	enthalpy [J/kg]
H	lower heating value [J/kg]
h_p	Planck constant [Js]
L_f	lift-off length [m]
L_{liq}	liquid length [m]
m	fraction of area occupied by fuel [–]
\dot{m}	mass flux [kg/s]
M	molar mass [kg/mol]
n	number of nozzles [–]
N	number of mole [mol]
p	pressure [Pa]
P	partial pressure [Pa]
Q	heat [J]
r	distance in radial direction [m]
r_p	production rate [mg/kJ]
s	piston stroke [m]
S	penetration [m]
S_L	laminar flame speed [m/s]
S_T	turbulent flame speed [m/s]
t	time [s]
Δt	ignition delay [s]

LIST OF TABLES

T	temperature [K]
ΔT	temperature difference [K]
U	velocity [m/s]
v	specific volume [m ³ /kg]
x	distance in downstream direction [m]
x_i	species concentration [-]
X	mixture fraction [-]
y	distance in lateral direction [m]
Z_{st}	oxygen content [-]

Greek Letters

α	relative spray angle [°]
α_N	spray angle for model development [°]
α_p	parameter for radial spray shape [-]
β	infinitesimal angle [-]
ϵ	compression ratio [-]
Θ	spray angle [°]
κ	ratio of specific heat [-]
λ	wavelength [nm]
ν	frequency [Hz]
ξ	non-dimensional radial distance [-]
ρ	density [kg/m ³]
Φ	equivalence ratio [-]

Subscripts

a	ambient
ai	auto-ignition
b	boiling
c	center line
ch	combustion chamber
eff	effective
ex	exhaust gas

f	fuel
gas	gaseous
inj	injection
l	laminar
liq	liquid
ll	at liquid length
m	main
mix	mixture
mp	main relative to pilot
p	pilot
prod	product
reac	reactant
red	reduced
s	saturation
t	turbulent
Tr	trigger
vap	vaporization
w	wall
wet	wet exhaust gas

Superscripts

*	excited molecule
---	------------------

1 Introduction

1.1 Background

Extensive greenhouse gas emissions affect the climate and threaten ecosystems, public health, and the economy. The Paris Agreement, signed in 2015 by 195 nations, aims to reduce the risks caused by global climate change by keeping the global average temperature rise well below 2°C above pre-industrial levels. Therefore, emissions of greenhouse gases have to be reduced drastically. Global shipping contributes about 3% to current global greenhouse gas emissions [24, 25]. Following the ambitions of the Paris Agreement, the International Maritime Organization (IMO) declared the goal to reach net zero emissions from international shipping close to 2050. This goal requires decarbonizing fossil fuel-based ship propulsion systems. Given the 20 – 30 years lifetime of marine vessels, zero-emissions propulsion systems must be developed swiftly [24]. However, shipping propulsion is particularly challenging to decarbonize, as high energy densities are required.

Synthetic fuels offer the energy density and low-cost storage required by shipping applications. Furthermore, using synthetic fuels in existing ship engines after minor modifications loosens the time urge for renewing vessels. In addition, an operation on conventional fuels will be possible during low availability of renewably produced synthetic fuels, e.g. during winter in the northern hemisphere. Among the synthetic fuels available, only hydrogen and ammonia are carbon-free. Liquefied ammonia offers a higher volumetric energy density and is safer to handle and store than hydrogen [26]. Although gaseous at standard conditions, ammonia liquefies at temperatures of only -33°C at atmospheric pressures, which is significantly easier to obtain than the -253°C required for liquefying hydrogen at atmospheric pressures. Therefore, ammonia is projected to fuel future vessels [27, 28]. While the case for ammonia

is particularly strong in the shipping industry, further possible applications include power generation [26, 29] and vehicular applications [21, 30].

Since the development of the Haber-Bosch process a century ago, ammonia has become essential for modern society. Ammonia-based fertilizers boost agricultural productivity and increase food security. Therefore, it is one of the world's most produced chemicals, consuming 2% of worldwide primary energy consumption [31]. The existing distribution networks, tankers, port infrastructure, and experience in handling ammonia may serve as the starting point for its future use as a fuel. Currently, ammonia production relies heavily on fossil fuels, mainly natural gas. Ammonia production has to include carbon capture and storage technologies or rely on renewably produced power to achieve climate neutrality. Countries with high potential for producing renewable power, such as Morocco, may act as ammonia hubs in the future for fueling vessels and exporting renewably produced ammonia at large scales [27].

Ammonia can be used as fuel in engines, gas turbines, and fuel cells. Internal combustion engines offer a good trade-off regarding fuel economy, robustness, and cost-effectiveness for applications such as shipping. However, ammonia offers several challenges for engine designers. Its high auto-ignition temperature, slow laminar burning velocities, high enthalpy of evaporation, and narrow flammability limits require measures to improve its combustion behavior [32]. These measures include hydrogen addition [32], ammonia dissociation prior to combustion [33], employing additional pilot fuels [34], and boosted engine conditions [32]. Another major concern for ammonia combustion in engines is the extensive formation of air pollutants [32, 34]. In particular, the potent greenhouse gas N_2O and the toxic gases NO and NO_2 , as well as unburned NH_3 , need to be controlled.

Ammonia was sporadically investigated as an alternative engine fuel during phases of short supply, e.g. during World War II and the oil crisis (e.g. [32–34]). However, intense research on ammonia combustion has just recently started with the background of climate action. Therefore, the potential performance of ammonia in modern heavy-duty engines still needs to be clarified. Recent research focuses on reducing unburned ammonia and nitrogen-based emis-

sions, particularly the greenhouse gas N_2O . Most investigations use homogeneous, gaseous ammonia or ammonia/hydrogen mixtures [14, 35]. So far, the diesel-like process, relying on the diffusive combustion of directly injected ammonia, has received much less attention, and its performance still needs to be explored. However, the high-pressure direct injection can reduce unburned ammonia emissions by reducing near-wall quenching and fuel accumulation in piston crevices. In addition, the absence of knocking allows higher compression ratios, leading to higher thermal efficiencies compared to the combustion of homogenous mixtures. An additional pilot fuel injection (e.g. diesel) is still necessary to ignite the ammonia spray. This combustion process, in which main fuel and pilot fuel are both injected close to the top dead center (TDC), is known as high-pressure dual-fuel combustion (HPDF) and has been applied mainly to methane (e.g. [36, 37]) and methanol (e.g. [38–40]), so far.

The physical properties of ammonia and pollutant formation mechanisms of ammonia combustion are significantly different compared to conventional fuels. Therefore, basic research on the mechanisms governing diesel-piloted ammonia spray combustion is required to develop suitable engines, injection systems, and operating strategies.

1.2 Research Objectives and Thesis Outline

While ammonia spray combustion has received little attention, a vast body of knowledge exists for diesel spray combustion. This thesis aims to establish a fundamental understanding of the piloted combustion of ammonia sprays by conducting basic experiments and transferring concepts and methods established for diesel combustion to ammonia. Furthermore, the thesis elucidates the particular challenges for the HPDF combustion of ammonia by comparing ammonia’s combustion behavior to other HPDF fuels (methane and methanol). The improved understanding will help develop suitable operating strategies for ammonia engines. In addition, the experimental database obtained can validate CFD simulations.

The experiments are conducted at well-defined, engine-relevant boundary con-

ditions in a rapid compression expansion machine (RCEM) acting as a single-shot engine using diesel as pilot fuel. The machine allows the variation of operating conditions, injection parameters, and geometrical arrangements. These variations enable broad parameter studies that reveal their influence on combustion. Combustion and mixture formation are analyzed via heat release rates (HRR), exhaust gas compositions, as well as optical data, including Shadowgraphy (SG), OH* chemiluminescence (CL), Mie-scattering (MS), natural flame luminosity (NL), and spectroscopic imaging. Mixing-limited 1-D spray models and $\Phi - T$ maps assist in interpreting the experimental results.

The investigations aim at the following objectives:

- Theoretically characterize ammonia as a fuel for high-pressure direct injection combustion and derive suitable combustion strategies.
- Elucidate the challenges for ammonia's spray combustion and reveal research needs.
- Show the feasibility of diesel-piloted ammonia spray combustion by determining charge conditions, spray interaction patterns, and pilot amounts required for ignition and combustion.
- Identify suitable wavelengths for optically investigating the combustion process using natural flame emissions.
- Characterize the combustion and mixture formation process in detail using optical imaging techniques.
- Obtain validation data for spray models and CFD simulations under inert and reacting conditions.
- Explain the observed combustion behavior using 1-D spray model simulations.
- Derive operating strategies from the observed behavior and test them experimentally.

The thesis is structured as follows: First, Chapter 2 presents important fundamentals, including fuel injection, mixture formation, flame stabilization, a

phenomenological description of diesel combustion, and pollutant formation behavior of diesel combustion. In addition, the fundamentals of chemiluminescence are outlined, including a short review of optical studies using ammonia's natural flame emissions.

Based on the fundamentals presented, Chapter 3 theoretically characterizes ammonia as fuel. Therefore, the effects of ammonia's physical properties on mixture formation and flame stabilization are discussed. In addition, the chapter elucidates ammonia oxidation pathways and explores engine-relevant pollutant formation behavior using $\Phi - T$ maps. Based on this characterization, challenges for ammonia spray combustion are introduced.

Chapter 4 presents the experimental setup. The chapter includes a description of the RCEM, the fuel injection system, as well as the optical measurement systems, including the optical setups for SG, MS, NL, and spectroscopic imaging. Furthermore, it describes the exhaust gas analysis setup and the controls and data acquisition system. In addition, estimates for the experimental uncertainties are provided.

Chapter 5 describes the methods used in this thesis. The chapter includes descriptions of the thermodynamic model used to infer HRRs from the measured quantities, procedures for post-processing imaging results, and the 1-D spray model.

The subsequent chapters present experimental and modeling results. Chapter 6 identifies the conditions under which HPDF combustion of ammonia is feasible by examining the ignition and combustion characteristics of ammonia sprays ignited by diesel pilot injections. A systematic variation of ammonia and diesel's temporal and spatial interaction identifies suitable injector configurations and injection strategies. Charge conditions and pilot characteristics are varied based on a suitable configuration.

Chapter 7 characterizes the diesel-piloted ammonia spray combustion optically. First, temporally and spatially integrated flame spectra reveal, which species contribute significantly to the natural flame emissions observed. Subsequently, SG, OH* CL, NL images, and time-resolved flame spectra are discussed in context to the HRR to characterize the combustion process. Finally,

the chapter discusses the individual contribution of excited species to ammonia's flame emissions by analyzing background-corrected species intensity evolutions.

Chapter 8 discusses mixture formation and flame stabilization characteristics of ammonia sprays. First, SG and MS measurement results under non-reacting conditions validate the 1-D spray model. Then, lift-off length evolutions deduced from OH* CL illustrate the lift-off length evolution and the lack of flame stabilization. Subsequently, the validated spray model reveals equivalence ratio and temperature distributions within ammonia sprays. A combination of low spray temperatures, high auto-ignition temperature, and fast lean-out of ammonia sprays inhibits flame stabilization. Finally, the implications of increasing lift-off length on engine performance and emission formation are discussed, and countermeasures are suggested.

Chapter 9 investigates the effect of diesel fuel post-injections (PIs) and intermediate-injections into the wake region of ammonia sprays with lifted reaction zones. First, unburned ammonia emissions are investigated for different PI timings and amounts. In addition, the chapter discusses the influence of PIs on pollutant formation characteristics.

Finally, Chapter 10 provides a summary and the main conclusions.

2 Fundamentals

Spray characteristics determine the diesel combustion process and resulting engine performance. In addition to pure fuel delivery into the combustion chamber, the highly turbulent spray rapidly mixes fuel and air. This mixing interacts with various combustion-relevant processes such as fuel evaporation and heat-up, ignition, flame stabilization, and emission formation. While the high-pressure direct injection of ammonia has not yet received much attention, extensive knowledge exists on conventional diesel fuel spray formation. This chapter presents the fundamentals of fuel injection, mixture formation, flame stabilization, diesel spray combustion, and pollutant formation in diesel engines. Even though the models and concepts were developed for conventional diesel fuel, they are a starting point for carving out ammonia's particularities in Chapter 3. In addition, the fundamentals of chemiluminescence are presented, including a more detailed discussion of ammonia's flame emissions.

2.1 Fuel Injection and Mixture Formation

While diesel injection systems have various types and implementations (e.g. needle form, nozzle type), the underlying physical processes are similar. The following section first summarizes the general processes during fuel injection as found in various standard textbooks, e.g. [41–43]. Subsequently, models for macroscopic spray characteristics are presented in more detail.

The spray breakup is illustrated in Figure 2.1. Lifting the injector needle initiates spray injection by enabling highly pressurized fuel to flow into the sack hole connected to the nozzle. The resulting nozzle flow is highly turbulent and subject to cavitation, which governs the subsequent phases of spray formation. At the nozzle exit, the liquid spray body disintegrates into single droplets, a

process called the primary breakup. During the following secondary breakup, the formed droplets reduce further in size due to aerodynamic forces. The impulse of the fuel spray leads to air entrainment into the spray region and mixing between fuel and air. In engine applications, the ambient air entrained into the fuel spray causes vaporization of the fuel droplets. The vaporization can coincide with breakup and combustion processes, making the diesel combustion process highly complex. While the gas phase penetration S into the combustion chamber grows until intercepted, all liquid droplets will eventually evaporate at a certain distance from the injector. This maximum penetration is the liquid length L_{liq} . Due to mass flux transients during the needle lift at the start of injection, a fuel-rich head vortex forms [44], in which less air entrains. On the contrary, the transient mass flux at the injection's end causes increased air entrainment. This entrainment wave starts at the rear part of the jet and spreads towards its tip [16].

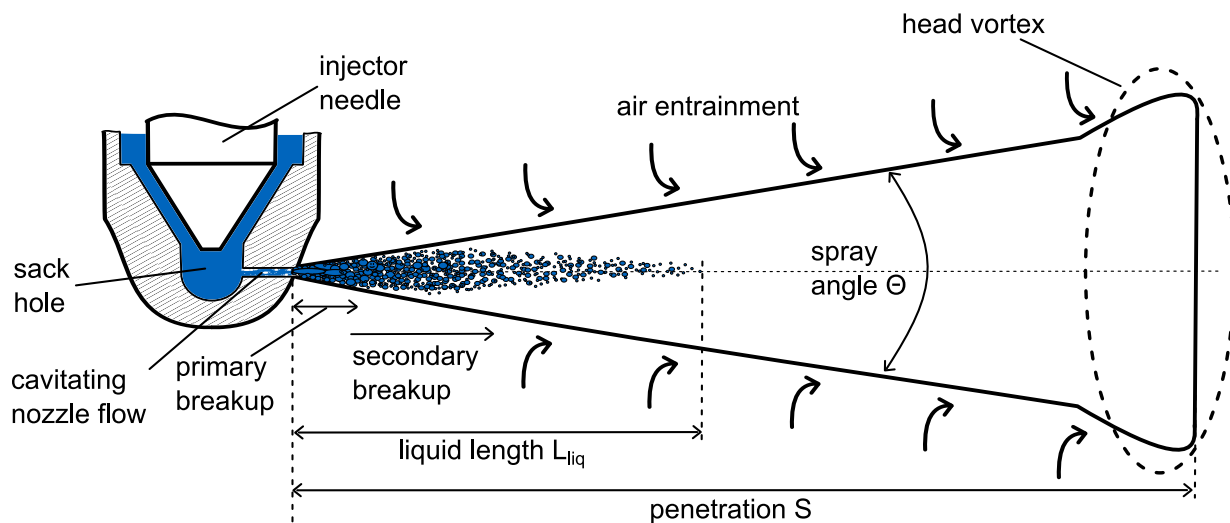


Figure 2.1: Scheme of nozzle flow, spray breakup, and spray penetration of a diesel spray. Adapted from [7].

High ambient densities and high injection pressures are particular for diesel injection. The resulting large aerodynamic forces disintegrate the liquid bulk into small droplets immediately after leaving the nozzle. Therefore, the droplet velocity quickly aligns with the velocity of entrained ambient gas, and the assumption of a two-phase flow with zero relative velocity becomes valid [45]. Under the additional assumption of non-vaporizing sprays, basic spray prop-

erties can be derived based on the conservation of mass and momentum. The conservation of mass for a control volume in a spray with a constant velocity profile, as depicted in Figure 2.2, can be formulated as follows:

$$A_f(0) \rho_f U_f(0) = A(x) \rho_m U(x) - (1 - m) A(x) \rho_a U(x). \quad (2.1)$$

The conservation of momentum yields:

$$\rho_f A_f(0) U_f^2 = \rho_m A(x) U(x)^2. \quad (2.2)$$

The quantities ρ_f , ρ_a and ρ_m represent the fuel, air and mixture density, $U_f(0)$ is the initial fuel velocity, $A_f(0)$ the nozzle area, $A(x)$ the spray area at the axial location x , and $U(x)$ the spray velocity at x . The fraction of the spray area occupied by fuel is represented by m . The initial fuel velocity $U_f(0)$ can be obtained via the Bernoulli equation:

$$U_f(0) = \sqrt{2 \frac{p_f - p_a}{\rho_f}}, \quad (2.3)$$

with the fuel pressure before the nozzle p_f and the ambient pressure in the combustion chamber p_a .

Under consideration of geometrical relationships and some additional simplifying assumptions, correlations for spray penetration over time can be derived from the equations above. Exemplary derivations can be found in [8, 45, 46]. Following the work by Naber [8], which assumes the fuel flow area in the spray to be zero ($m = 0$) and fixes constants by comparison with experimental data, the fuel spray penetration can be written as follows:

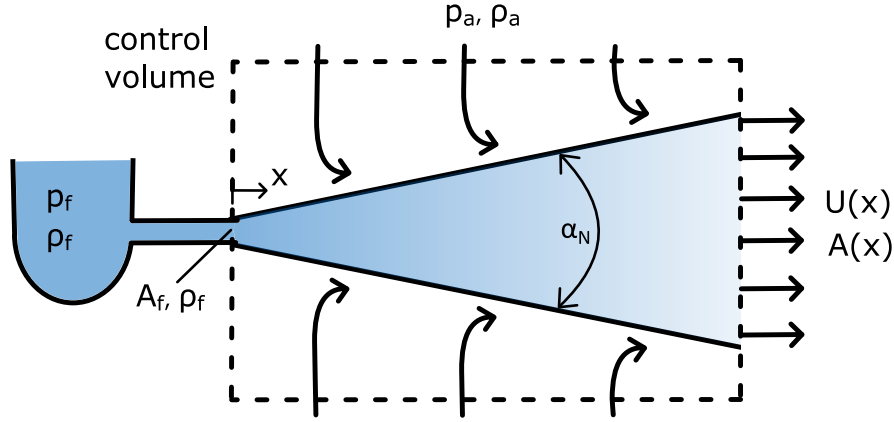


Figure 2.2: Schematic of a control volume used to derive basic spray properties. Adapted from [8].

$$S(t) = \sqrt{\frac{C_v \sqrt{2} C_a}{a \tan(\Theta/2)}} \sqrt{\sqrt{\frac{(p_f - p_a)}{\rho_a}} d_0 t}, \quad (2.4)$$

where the factor C_v accounts for head losses in the nozzle flow, C_a accounts for fuel flow area loss in the nozzle (e.g. due to cavitation), and a is a constant factor relating the measured spray angle Θ to the angle α_N used for developing the model (see Figure 2.2). The constant a accounts for effects due to radial gradients within the spray which are not explicitly considered in the model.

The vaporization of fuel sprays generally leads to slightly lower dispersion angles and slower penetration up until the liquid length compared to non-evaporating sprays. This effect is caused by a volume contraction due to evaporative cooling and can be considered an effect of the fuel used [8]. In addition to vaporization, orifice parameters (e.g. conicity, edge form) and the density ratio of fuel to ambient air influence the spray spreading angle Θ [47]. The other terms in Equation 2.4 can be separated into ambient effects (p_a , ρ_a) and injection/nozzle effects (C_v , C_a , p_f , d_0). Spray penetration correlations are used for injector and combustion chamber design. In addition, they are used to estimate the influence of different fuel properties on spray penetration.

The equations for conservation of mass and momentum for the control volume

of the conceptual schematic shown in Figure 2.2 (Equations 2.1 and 2.2) also yield relationships for fuel and air mass flow rates \dot{m}_a and \dot{m}_f at a distance x from the injector [48]:

$$\dot{m}_a \propto n \sqrt{\rho_a \rho_f} d_0 U_f \tan(\Theta/2) x, \quad (2.5)$$

$$\dot{m}_f \propto n \rho_f d_0^2 U_f, \quad (2.6)$$

where n has been added to represent the number of nozzles of a fuel injector. The ratio of the two mass fluxes follows as:

$$\frac{\dot{m}_a}{\dot{m}_f} \propto \sqrt{\frac{\rho_a}{\rho_f}} \frac{\tan(\Theta/2)}{d_0} x. \quad (2.7)$$

As shown by [48], the behavior of the liquid length can be well predicted by assuming that only the supplied enthalpy of entrained ambient air limits the vaporization of fuel droplets. This assumption implies that interfacial mass and heat transport phenomena do not limit the vaporization of fuel droplets. Therefore, only the air-to-fuel ratio necessary for vaporization and the actual air-to-fuel ratio in the spray (Equation 2.7) determine the maximum liquid length. Other injection parameters, such as the injection pressure, do not alter the liquid length by increasing the driving force for atomization processes.

Fuel effects on liquid length are incorporated via the fuel density in Equation 2.7 and the air-to-fuel ratio required for complete vaporization. The air-to-fuel ratio required for complete vaporization is reached when the fuel is saturated in thermodynamic equilibrium with the ambient gas at a common temperature T_s . This air-to-fuel ratio is a function of T_s , the partial pressure of fuel P_f , and the partial pressure of air P_a [48]:

$$\frac{\dot{m}_a}{\dot{m}_f} = \frac{h_f(T_f) - h_f(T_f, P_a)}{h_a(T_a, P_a) - h_a(T_s, P_a - P_s)}. \quad (2.8)$$

T_s results from iteratively solving mass- and energy balances and the real gas equation of state [48]. The procedure is similar to determining surface temperatures of droplets in vaporizing environments [43]. For droplet evaporation, the equilibrium surface temperature T_s can be substituted by the boiling temperature T_b at the corresponding pressure if gas temperatures are high [49]. Higgins et al. [23] use a similar approach for predicting liquid lengths of different multi-component fuels due to simplicity and the lack of exact fluid properties.

While the discussed macroscopic spray models assume uniform radial mixture fractions and velocity profiles, actual sprays show higher velocities and richer mixtures in the core region. The resulting profiles are similar to a Gaussian error function [50]. 1-D models that incorporate more realistic profiles are presented by [16] and [51]. In addition, transient effects (e.g. entrainment waves) can be considered by numerically solving the equations obtained from the conservation of mass, momentum, and energy based on control volumes. The accuracy of these mixture fraction predictions is sufficient for primary estimates [52].

2.2 Phenomenological Description of Diesel Combustion

The understanding of the processes and mechanisms governing diesel combustion has evolved over the last decades. Increasingly sophisticated optical imaging techniques provided more profound insight into mixture formation, ignition, combustion, and pollutant formation. Laser-sheet imaging studies, such as laser-induced fluorescence of key species, have provided the data on which the current state of understanding builds (e.g. [9, 53–55]). The following section presents a phenomenological description of diesel combustion based

on Dec [9] and modifications by [53–56]. This model applies to conventional diesel combustion as encountered in heavy-duty engines. The model assumes a quasi-steady period, in which the fuel burns mixing-controlled. At low loads, modern diesel engines often feature partially premixed low-temperature combustion, which reduces soot and NO_x formation by increasing the degree of mixing of fuel and oxidizer before combustion. Extensions of the presented model for partially premixed combustion can be found in the literature (e.g. [56]).

Liquid fuel is injected into the combustion chamber close to TDC, leading to mixing with air, heat-up, and fuel evaporation. Average equivalence ratios decrease with increasing distance from the nozzle as more air entrains while the spray penetrates into the combustion chamber. At the liquid length, sufficient air is entrained into the spray to fully vaporize the fuel (see Section 2.1). The gas phase continues to penetrate and forms the typical head vortex. Then, first-stage ignition reactions commence, indicated by the occurrence of intermediate species, such as formaldehyde (HCOH). While the heat release is low during the first-stage ignition, it rises sharply as the highly exothermic second-stage ignition initiates the combustion of combustible fuel/air mixtures formed during the earlier stages of fuel injection. This phase is referred to as the premixed combustion phase.

As temperatures rise in the fuel-rich combustion products, fuel molecules break down to form polycyclic aromatic hydrocarbons, a soot precursor. During the premixed combustion phase, a thin diffusion flame forms on the jet periphery, which consumes the intermediate products of the fuel-rich combustion. The diffusion flame encircles the downstream portion of the jet and extends up to the lift-off length in the upstream direction. The combustion of near-stoichiometric mixtures in the diffusion flame leads to high temperatures. Therefore, nitrogen oxides form via the Zeldovich mechanism near the diffusion flame. This mechanism represents the primary NO_x formation mechanism for engine combustion of fuels that do not contain significant amounts of nitrogen [57]. As fuel mixes with air upstream of the lift-off length, a standing reaction zone forms near the lift-off length. The fuel-air mixture entering the standing reaction zone first undergoes first-stage ignition, forming inter-

mediate products (e.g. HCOH , H_2O_2). Subsequently, second-stage ignition reactions cause a rapid rise in temperatures. As hot combustion products of the standing reaction zone and the diffusion flame mix, the resulting hot and fuel-rich mixtures cause ongoing soot formation in the core of the jet. The equivalence ratios in the standing reaction zone change with the lift-off length. Longer lift-off lengths generally lead to lower equivalence ratios and less soot formation [58]. Figure 2.3 shows the resulting jet appearance, which is typical for the quasi-steady period. The HRR during this period is constant and similar to the heating value flux of the fuel injection.

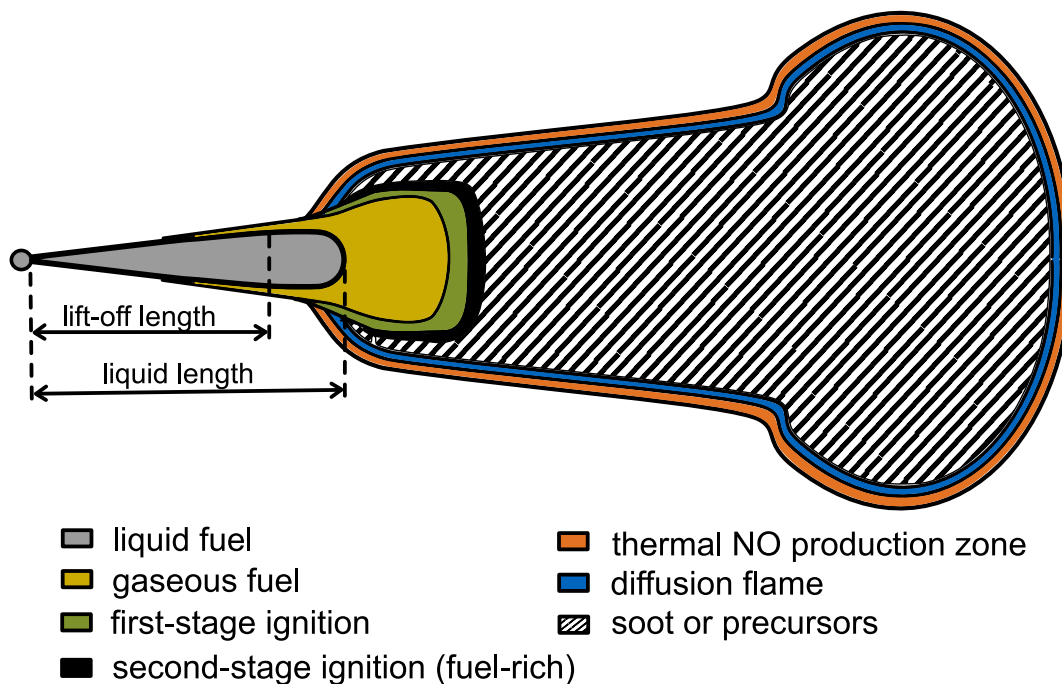


Figure 2.3: Schematic of a conceptual model for conventional diesel combustion. Adapted from [9].

The key features of the spray appearance only start changing during the end of fuel injection. The work of Dec does not cover this phase, which was only described later by Musculus et al. [56]. During the fuel's injection rate ramp-down, a prominent feature is the formation of entrainment waves [16, 59]. Continuity requires additional air entrainment into the spray as the fuel injection mass flux decreases. Therefore, equivalence ratios rapidly decrease near the nozzle during injection rate ramp-downs. As a result of increased air entrainment, auto-ignition may occur in the wake region, causing the flame to

propagate to the nozzle exit.

2.3 Flame Stabilization

After auto-ignition, diesel diffusion flames stabilize at a certain distance from the nozzle exit [60]. This lift-off length L_f influences soot formation during diesel combustion, as it determines the amount of air entrained into the spray up to the flame front [58]. The following relationship for the lift-off length is based on experimental investigations by [61–63]:

$$L_f \propto p_{\text{inj}}^{0.5} T_a^{-3.74} \rho_a^{-0.85} d_0^{0.34} Z_{\text{st}}^{-1}, \quad (2.9)$$

where p_{inj} represents the injection pressure, T_a the ambient temperature and Z_{st} the oxygen content.

The mechanisms underlying flame stabilization of spray flames under diesel engine conditions still have to be clarified. So far, various flame stabilization mechanisms have been proposed in the literature, including flame stabilization by flame propagation, triple flame propagation, auto-ignition, recirculation of burnt gases, and critical scalar dissipation. A recent comprehensive overview is provided by Tagliante-Saracino [64]. Recent experimental and numerical evidence shows that auto-ignition processes cause flame stabilization for diesel fuel. The first experimental observation supporting this was made by Picket et al. [65], who showed an influence of the fuel’s ignition quality on the lift-off length and observed ignition processes in stationary attached diesel sprays upstream of the lift-off length. Nonetheless, models for atmospheric gas jets predict certain features of the diesel lift-off behavior, even though they cannot capture the exact physical process [66]. Experimental evidence for flame stabilization by auto-ignition has not yet been obtained for alternative fuels without two-stage ignition. For those fuels, significantly different physical properties, such as higher auto-ignition requirements, may alter the spray stabilization mechanism. The following sections briefly outline the current understanding

of the most prominent flame stabilization mechanisms, i.e. flame propagation and auto-ignition, based on [10, 64, 67, 68]. The focus is on the current understanding of flame stabilization at engine-relevant conditions.

2.3.1 Flame Stabilization by Flame Propagation

Flame stabilization by flame propagation relies on an equilibrium between local flow velocity and flame propagation speed. Fuel mixes with oxidizer starting from the injector outlet up to the lift-off length in diffusion flames. The flame will stabilize at a distance where the turbulent flame speed S_T equals the mean flow velocity. The turbulent flame speed S_T can be estimated using the following equation [10]:

$$S_T = S_L^0 \frac{A_T}{A}, \quad (2.10)$$

where S_L^0 is the laminar flame speed, $\frac{A_T}{A}$ is the ratio of the turbulent flame area A_T within a control volume, and A is the area of the control volume. As the ratio exceeds unity, the increase in flame speed facilitates flame stabilization. Predicting the ratio $\frac{A_T}{A}$ via semi-phenomenological models poses great difficulty and shows considerable scatter [67].

In most technical applications, the mixing of fuel and oxidizer up to the flame front is incomplete. As a result, triple flames (also called edge-flames), consisting of a fuel-rich flame, a fuel-lean flame, and a central stoichiometric flame branch, have been suggested as a mechanism for flame stabilization (see Figure 2.4). Flow divergence before the triple point facilitates flame stabilization via triple flames. The flow velocity is larger than the laminar flame speed upstream of the triple point. However, at the triple point, stagnation effects due to heat release and subsequent volume expansion in the burnt zone cause the flow to stagnate. As a result, the flame speed matches the local flow velocity [69]. When strongly deviating from the stoichiometric mixture line, flame

speeds decrease and cannot match the flow velocity. Thus, they only stabilize further downstream, where flow velocities are lower, which explains the characteristic shape of triple flames.

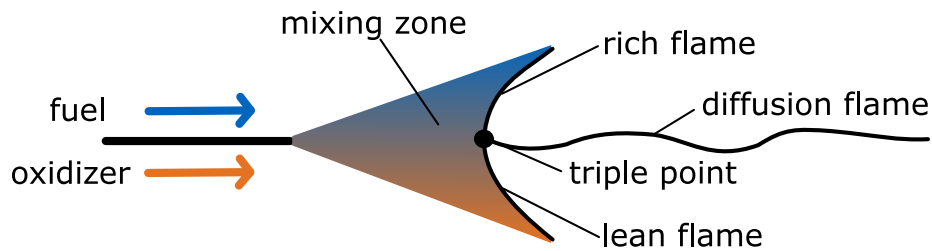


Figure 2.4: Schematic of flame stabilization by a triple flame. Adapted from [10].

While triple flames have become widely accepted as flame stabilization mechanisms for lifted diffusion flames under various conditions, auto-ignition has emerged as the primary stabilization mechanism under diesel engine conditions using diesel fuel. However, recent studies using alternative fuels challenge the auto-ignition stabilization mechanism prevailing for diesel fuel. Jet flames of methane and hydrogen have been observed to stabilize under conditions insufficient for auto-ignition after induced ignition by diesel pilot injections (e.g. [70, 71]). Furthermore, Yip et al. [72] investigated laser-ignited hydrogen jets under conditions insufficient for auto-ignition. After upstream propagation, the flame stabilized at a constant lift-off length. By considering flame propagation on the jet edges via triple flames as the stabilization mechanism, they could explain the trends observed for temperature and oxygen content variations. However, the current understanding of flame stabilization by auto-ignition, outlined in the following section, involves a crucial role of re-entrained combustion products that assist the auto-ignition events. Considering this re-entrainment, the studies above cannot rule out flame stabilization mechanisms relying on product gas assisted auto-ignition.

2.3.2 Flame Stabilization by Auto-Ignition

After Picket et al. [65] observed auto-ignition events upstream of the lift-off length, follow-up studies investigated the underlying mechanisms. The lift-off

length of diesel sprays, whose ignition is induced by a laser upstream of their naturally occurring lift-off length, persists upstream of its natural lift-off position [11]. The lift-off returns to its natural position only after a significant time longer than the time usually available in engines. This observation contradicts theories assuming flame propagation to stabilize diesel spray flames, as spray velocities are high near the nozzle. Furthermore, stabilization by auto-ignition of the reactants alone cannot explain the long stabilized period upstream of the ignition event due to the shorter residence times at high jet velocities far upstream. Therefore, Picket et al. [11] suggest a stabilization mechanism based on the re-entrainment of hot product gas from high-temperature product reservoirs on the jet edges into the reaction propagation zone. The resulting increase in temperature after re-entrainment causes auto-ignition of the mixture in the reaction propagation zone. Figure 2.5 shows a schematic of the lift-off stabilization mechanism. In a stationary condition at the natural lift-off length, the mass flux between the reaction propagation zone and the high-temperature product reservoir on the spray edge near the lift-off length is balanced. If an upstream ignition event shifts the lift-off upstream, the high-temperature product reservoir will also shift further upstream. When the lift-off starts moving downstream again, the high-temperature product reservoir slowly depletes and delivers the necessary enthalpy to the fuel and air region to undergo auto-ignition. This process adds the observed inertia to flame stabilization models based on auto-ignition.

The presented lift-off stabilization mechanism via auto-ignition of the fuel/air mixture implies an important role of the ignition delay. The ignition delay phase encompasses a chemical and a physical contribution [57]. The time needed for auto-ignition after forming a combustible mixture defines the chemical ignition delay. The physical ignition delay comprises the processes until this mixture is obtained, such as vaporization and heat-up. Small amounts of ignition-enhancing additives increase the fuel's ignition quality (i.e. the cetane number). Due to overall small mass fractions, the ignition enhancers do not significantly alter the fuel's physical properties and the physical contribution to the ignition delay. Instead, ignition enhancers mainly alter the chemical ignition delay. The effect of ignition-enhancing additives on the lift-off length is weak, suggesting that the chemical ignition delay only plays a minor role

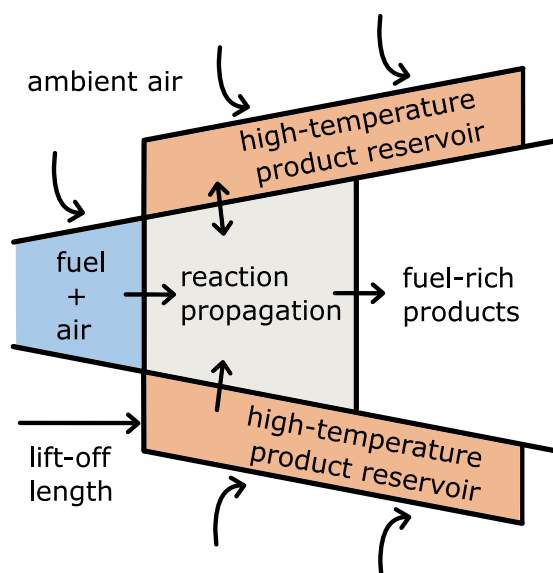


Figure 2.5: Schematic of the lift-off stabilization mechanism after an upstream ignition event. Adapted from [11].

in lift-off stabilization [17]. Instead, factors that affect the reactant and product temperatures, such as ambient oxygen content, strongly influence lift-off. Therefore, Persson et al. [17] attribute fuel effects on flame stabilization mainly to the fuel's mixing requirements of high-temperature combustion products with fuel/air mixtures to reach auto-ignition conditions.

Direct numerical simulations by Tagliante et al. [73] support auto-ignition as the key stabilization mechanism for diesel diffusion flames. They found that the lift-off length of stabilized flames repeatedly jumps upstream due to auto-ignition events. Subsequently, the reaction zone convects downstream until the next auto-ignition event occurs. Combustion products recirculated in the highly turbulent jet edges induce the major part of auto-ignition events. However, some auto-ignition events occur without the assistance of additional combustion products. Flame propagation, e.g. triple flames, cannot match the downstream convection at any time and does not contribute to flame stabilization. However, flame propagation still retains an important role, as flame propagation after auto-ignition is vital for producing the combustion products that cause auto-ignition after re-entrainment.

In engines, several sources, such as neighboring sprays and residual or prod-

uct gases from earlier injection phases, cause ignition events upstream of the natural lift-off length. For example, Chartier et al.[74] showed an influence of the proximity of a diesel spray to its neighboring sprays on the lift-off length. In addition, the entrainment of burned gases into the spray and the general pressure rise due to combustion causes a continuous reduction of the lift-off length during injection events (e.g. [74, 75]).

2.4 Pollutant Formation

Pollutant formation in engines is complex and influenced by the interaction of various parameters, including fuel injection and vaporization, charge composition, charge motion, fuel type and many more. However, $\Phi - T$ maps are a widespread and simple tool to illustrate soot and NO_x formation mechanisms [76, 77]. The $\Phi - T$ maps build on constant pressure reactor simulations with a constant temperature constraint in *Cantera*. Further details on the simulation procedure are presented in Section 3.4. This section uses $\Phi - T$ maps to introduce the conditions under which air pollutants form in diesel engines.

For this purpose, Figure 2.6 shows an exemplary $\Phi - T$ map for n-heptane combustion obtained with the Chalmers mechanism [78]. Using n-heptane as surrogate for diesel fuel limits the complexity of the underlying simulations. The map considers NO and acetylene (C_2H_2) formation. Acetylene is a soot precursor that qualitatively predicts conditions under which soot forms without requiring additional sub-models [77]. In addition, the mixing line in the $\Phi - T$ map indicates states that result from mixing n-heptane injected at 293 K and charge air at 920 K (see OP4 in Section 4.1). The adiabatic combustion line indicates the conditions obtained after mixtures at the corresponding state on the mixing line burn adiabatically.

C_2H_2 forms under intermediate temperatures and high equivalence ratios, while NO mainly forms at lean and close to stoichiometric conditions that show high combustion temperatures (see Section 2.2). NO production is kinetically limited and increases for longer residence times, as its formation occurs mainly via the Zeldovich mechanism for diesel fuel (see Section 3.3). Reaction

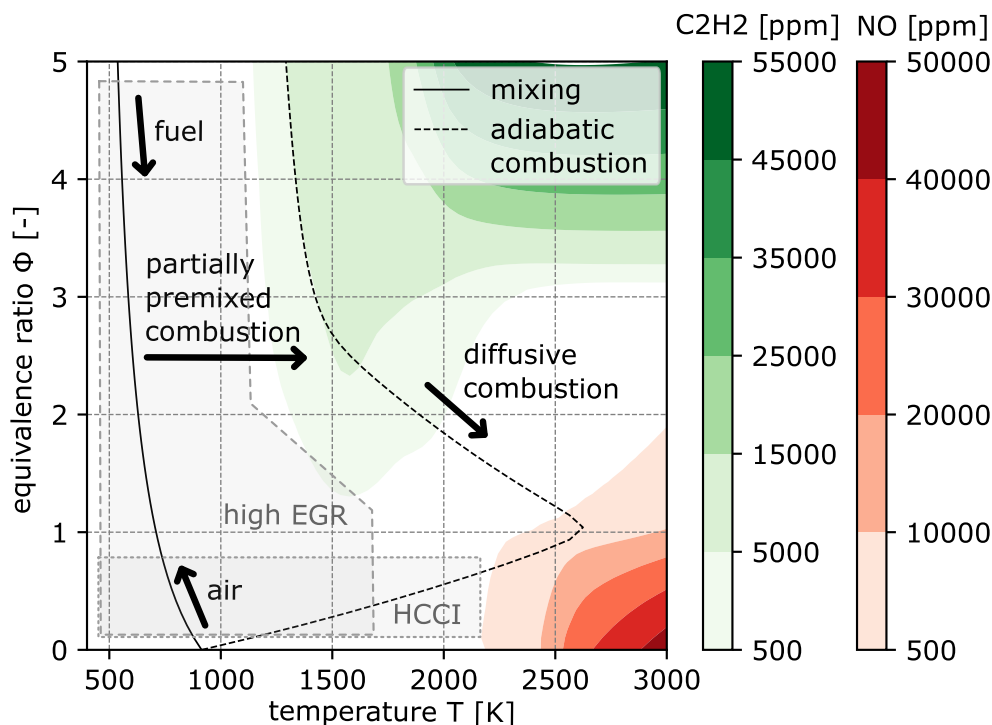


Figure 2.6: $\Phi - T$ map showing air pollutant forming conditions (NO , C_2H_2) for the combustion of n-heptane at 120 bar after 2 ms residence time. The lines indicate the states resulting from mixing and adiabatic combustion in the RCEM at OP4 after fuel injection at 293 K.

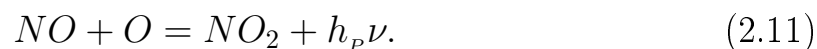
rates are particularly low for temperatures below 2200 K, which explains that almost no NO forms for lower temperatures.

Combustion strategies for hydrocarbon fuels increase premixing and decrease combustion temperatures to avoid soot and NO_x formation. Exhaust gas recycling (EGR) lowers combustion temperatures by adding product species, such as CO_2 and H_2O to the charge air [76, 77]. This addition of products lowers the oxygen's partial pressure in the mixture leading to reduced combustion temperatures. Therefore, the adiabatic combustion curve in Figure 2.6 shifts to the left when EGR is used and less NO and soot form. Strong mixing of fuel with air prior to combustion, as used in Homogenous Charge Compression Ignition (HCCI) combustion strategies, avoids pollutant formation by burning fuel lean of stoichiometry. This mixing beyond stoichiometry

lowers combustion temperatures due to an increased heat capacity per fuel mass. Furthermore, the low equivalence ratios obtained decrease soot formation. Figure 2.6 indicates the conditions relevant for high EGR and HCCI combustion.

2.5 Chemiluminescence

First reports on ammonia flames describe a visible yellowish inner cone with an almost non-luminous outer flame region [79]. The inner cone was later attributed to be the result of flame radiation, e.g. due to the recombination reaction of nitric oxide and atomic oxygen according to the following reaction:



This continuous spectrum is only one of several observable flame emissions of ammonia flames. Observing natural flame emissions is regularly used to analyze combustion processes. The following section briefly summarizes the working principle of CL based on [13, 80]. Subsequently, emission spectra of ammonia and hydrocarbon flames are discussed to identify emission bands suitable for analyzing the diesel-piloted combustion of ammonia. In addition, the present section reviews recent optical studies relying on the natural flame emissions of ammonia.

Flame emissions result from the transition of electrons from an excited state to their ground state. This transition emits a photon whose energy corresponds to the energy difference between the higher and lower states. The inverse process, where photons are absorbed to excite electrons into a higher energy state, co-occurs in flames. As most flames are optically thin, molecules emit more photons than they absorb, and the flame radiation is visible from the outside. The excitation of molecules can be caused by absorption of photons, thermal collision with other molecules, or chemical reactions (CL). Chemical excitation dominates over thermal excitation below 2700 K for radiation from OH*

molecules, which is often observed in literature [80]. Flame spectra result from a superposition of emissions of various species in the flame. Free atoms lead to distinct peaks in emission spectra where each line corresponds to another electronic transition. However, the primary resonance lines of C, O, N, and H atoms are in the short ultra-violet (UV) range and are usually not observed in flames. For molecules, similar transitions cause changes in the molecule's internal vibrational and rotational energy. Therefore, each electronic transition leads to numerous lines in emission spectra called emission bands. In this work, A-X or B-X refers to the electron state transition from the excited state (A or B) into the ground state X. (v', v'') refers to the vibrational states of the electrons in their upper (v') and lower (v'') states. Figure 2.7 shows the electronic ground state and an excited state including vibrational states for an exemplary di-atomic molecule. Furthermore, the figure includes an exemplary electron transition causing chemiluminescence.

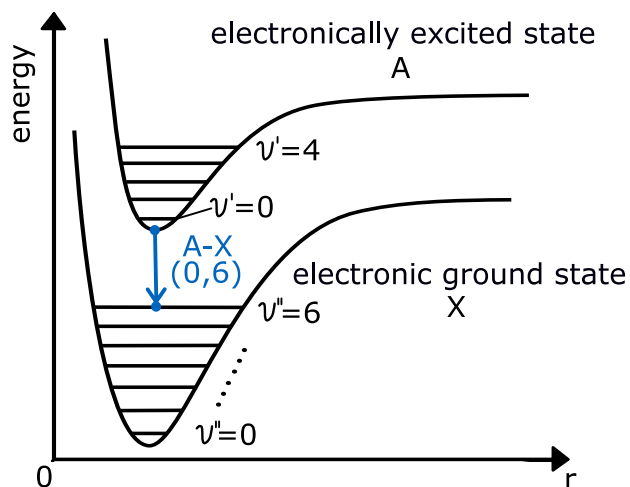


Figure 2.7: Schematic of energy levels of a diatomic molecule. Each electronic state (e.g. A or X) is divided into vibrational states (v' or v'') and rotational states (not shown). The blue transition arrow indicates the A-X(0,6) electron transition. Adapted from [12].

Band spectra from free radicals (e.g. OH^* and NH^*) are commonly observed in combustion diagnostics. Their emission bands lie in the visible or near UV range, and they are excited more strongly during combustion than free atoms [13]. While emission bands from di-atomic radicals (e.g. OH, CH, C_2 , CN, NO, NH) show sharp lines, which can be detected precisely, polyatomic molecules

(e.g. HCOH, HCO, CO₂, NO₂, H₂O) also show broadened and diffuse emission characteristics. Sooting flames emit continuous thermal radiation following Planck's law. Soot radiation overshadows band spectra in a wide range of wavelengths if soot intensity and temperatures are high. Soot intensity is typically high in the visible range and becomes negligible in the UV range, as soot temperatures in diesel engines usually range between 1000 – 2800 K [57].

Imaging of the flame's natural luminosity is used in experimental combustion research to infer important features of combustion processes, such as flame front location, ignition time and location, or HRR distribution [81, 82]. However, the chemiluminescent signature of flames generally depends strongly on the fuel used, combustion temperatures and pressures, equivalence ratios, and strain rates. In addition, most investigations target specific wavelength ranges using bandpass-filtered 2-D imaging techniques. Therefore, interference between the CL of several excited species emitting in the investigated band or with other sources of luminosity, such as soot, distorts the information obtained. For example, under high-temperature conditions, OH* CL is known to interfere with soot radiation [9, 83]. Under low-temperature combustion conditions, OH* CL interferes with CO₂* and HCO* broadband CL [84, 85]. Spectroscopic investigations can help distinguish the flame emissions' source by dispersing flame emissions based on their wavelengths. Figure 2.8 summarizes prominent emission bands of species in ammonia and diesel flames for wavelengths below 550 nm. [13] gives a more detailed overview of natural flame emissions from various flames.

The strong OH* bands in the UV range result from the A-X transitions, with the most prominent band around 308 nm corresponding to the (0,0) vibrational states. This well-known band is commonly observed in flames of various hydrogen-containing fuels, including ammonia and organic flames, such as diesel. The A-X (0,0) transition of CH* is characteristic of organic flames' CL signatures and emits strongest around 431.5 nm. CL of HCOH* (Emeleus's Cool Flame Band of formaldehyde) and HCO* (Vaidya's Hydrocarbon Bands of the formyl radical) occur in cool flames and during first-stage ignition of long-chained hydrocarbons, making it valuable for combustion diagnostics [13, 86]. The NH₂ α band extends from the visible into the UV range

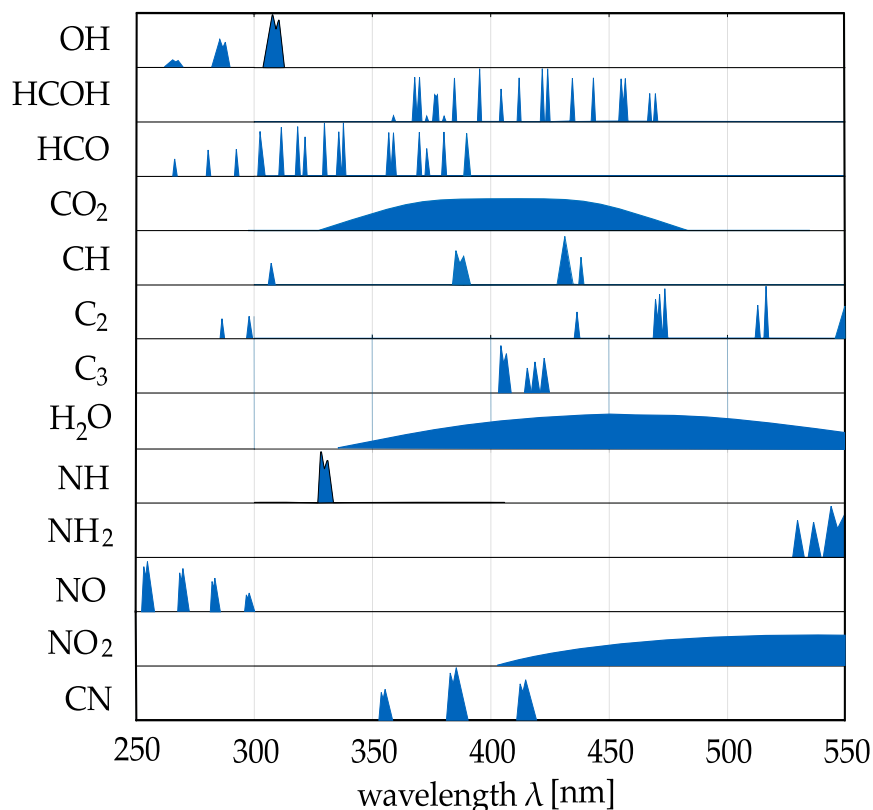


Figure 2.8: Emission bands from selected electrochemically excited species occurring in ammonia and hydrocarbon flames. Adapted from [13].

and is strongest in the yellow and green wavelength range. The band features distinct peaks superimposed on a broadband contribution. Furthermore, the NH^* (A-X (0,0)) peak system at 336 nm constitutes a distinct feature of ammonia's natural flame emissions. The NH^* (A-X (0,0)) band may be partly masked by the A-X (0,0) OH^* flame emissions [13]. Emission bands resulting from NH^* and NH_2^* are only apparent in ammonia flames and do not occur in diesel flames.

Only a few studies investigated the flame luminosity under engine-relevant temperatures and pressures for ammonia. Wang et al. [87] used visible flame luminosity to study pure ammonia spray combustion. They observed a transparent-like, orange-red flame with less intense luminosity than sooting diesel flames under similar conditions. Wüthrich et al. [88] used simultane-

ously acquired Schlieren and OH^* CL imaging to analyze the combustion of homogenous ammonia mixtures ignited by diesel pilots (low-pressure dual-fuel combustion), which allowed a detailed description of pilot fuel ignition, as well as flame transition to the premixed ammonia charge and subsequent flame propagation. Spectroscopic measurements of premixed mixtures containing ammonia have been carried out at atmospheric pressures for $\text{CH}_4/\text{NH}_3/\text{air}$ mixtures by Zhu et al. [89] and for $\text{CH}_4/\text{NH}_3/\text{H}_2/\text{air}$ by Mashruk et al. [90]. The studies detected NO^* , OH^* , NH^* , CN^* , CH^* , NH_2^* peaks, as well as CO_2^* , H_2O^* and NO_2^* broadband radiation. The intensity of all peaks (including NH^*) except NH_2^* decreased for increasing ammonia shares. While the behavior of CH^* and CN^* results from the reduced availability of carbon atoms, the decline of NH^* CL intensity was attributed to the reduced OH^* concentration in ammonia flames, as NH^* is mainly produced via the reaction $\text{NH}_2 + \text{OH} \rightarrow \text{NH} + \text{H}_2\text{O}$ [90]. Ichikawa et al. [91] reported the flame emission profiles obtained from stratified spray injection of ammonia and n-hexadecane through a single nozzle under engine-relevant conditions. By detecting the NH_2^* peaks, they corroborated that the supporting fuel successfully induced ammonia combustion.

3 Characterization of Ammonia as High-Pressure Direct Injection Fuel

Ammonia is an inorganic molecule and does not contain carbon. Therefore, its physical and chemical properties differ remarkably from conventional, carbon-based fuels. Table 3.1 shows selected physical properties of ammonia, typical diesel fuel (or n-dodecane if the value is unavailable for diesel), and methanol, a liquid alternative fuel already used for HPDF combustion (e.g. [38, 92]).

Table 3.1: Selected physical properties of ammonia, diesel/n-dodecane and methanol [14, 18–22]. Properties at standard conditions (293 K, 1 bar), if not specified otherwise.

Parameters	Ammonia	Diesel	Methanol
LHV [MJ/kg]	18.8	≈ 43.4	19.9
Latent heat of vaporization [kJ/kg]	1371	≈ 256	1101
Latent heat of vaporization / LHV [%]	7.3	≈ 0.6	5.5
Flammability limit [vol%]	16 – 25	$\approx 0.6 – 6.5$	6.7 – 36
Maximum flame speed [$\frac{m}{s}$]	0.067	0.8 (n-dodecane)	0.56
Adiabatic flame temperature [K]	2123	≈ 2326	2143
Minimum auto-ignition temperature [K]	924	$\approx 527 – 558$	738
Boiling temperature [K]	240	$\approx 555 – 611$	338
Fuel density ρ_f (at 293 K, 10 bar) [kg/m ³]	610	≈ 870	792
Stoichiometric air demand [kg _{air} /kg _f]	6.05	≈ 14.5	6.47
Critical temperature [K]	406	658 (n-dodecane)	513
Critical pressure [bar]	114	18 (n-dodecane)	81

Both ammonia and methanol show reduced lower heating values (LHV) and increased latent heats of vaporization compared to diesel. As a result, the ratio of latent heat of vaporization to heating value is particularly high for

both fuels. Therefore, a strong cooling effect in the combustion chamber is to be expected for the alternative fuels. Ammonia's comparably high lower flammability limit results in unburned fuel emissions from fuel-lean mixtures within the combustion chamber. In addition, ammonia's exceptionally high auto-ignition temperature and low flame speed will negatively impact its ability to form a stabilized flame (see Sections 2.3 and 3.2). The low fuel density requires the injection of large volume fluxes, e.g. via larger nozzles. Furthermore, the low stoichiometric air demand causes fuel/air mixtures to lean out rapidly after injection. The proximity of injection conditions to the two-phase region of ammonia, indicated by its low critical temperature and high critical pressure, facilitates flash-boiling effects. Furthermore, pollutant formation mechanisms differ significantly from hydrocarbons due to the nitrogen atom contained in the ammonia molecule. While ammonia combustion does not emit CO_2 , it forms nitrogen-based pollutants, such as laughing gas (N_2O) with a global warming potential of 265 times that of CO_2 [93].

Designing suitable combustion devices for ammonia requires detailed experimental and numerical investigations. However, fundamental considerations can contribute to understanding the mechanisms at work. This section characterizes ammonia as a fuel for high-pressure direct injection combustion. The considerations reveal general guidelines for injection and combustion strategies. First, differences in mixture formation behavior are elucidated. The subsequent section considers the impact of ammonia's physical properties on its flame stabilization behavior. Then, ammonia's oxidation pathways are summarized, and the pollutant formation characteristics are discussed using $\Phi - T$ maps. The final section of the chapter introduces the main challenges for the spray combustion of ammonia.

3.1 Mixture Formation

Fuel effects on mixture formation processes presented in Section 2.1 influence the combustion behavior. For example, extensive liquid lengths might cause impingement of liquid fuel on the piston bowl wall and lead to high unburned fuel emissions. Typical droplet sizes in ammonia sprays are, on average, 50 %–

70 % lower than in diesel sprays [94]. Therefore, assuming a two-phase flow with zero relative velocity and mixing-limited evaporation, as required for the diesel-based models presented in Section 2.1, is also valid for ammonia sprays. The following evaluation of ammonia’s mixture formation behavior gives insight into its suitability as a high-pressure direct injection fuel.

Based on non-dimensional groups deduced from theoretical considerations presented in Section 2.1, Higgins et al. [23] suggest an engineering correlation, which enables estimating the liquid lengths of arbitrary fuels from their properties at atmospheric conditions. The simple estimate neglects several effects, such as the increase of boiling temperature with increasing pressure (which is particularly high for ammonia due to the curvature of the boiling curve), temperature-dependent physical properties, and the fact that fuels evaporate below their boiling temperature in fuel/air mixtures. Section 3.4 introduces a detailed method to calculate the thermodynamic state within fuel sprays. Appendix A includes the values of the physical properties and the correlations used in this section. As ammonia is gaseous at atmospheric conditions, the estimates use the physical properties of ammonia at 10 bar instead of at atmospheric conditions as suggested by Higgins et al. [23]. Table 3.2 lists the resulting ratios for the liquid length L_{liq} to nozzle orifice diameter d_0 at an ambient air temperature of 920 K and an ambient pressure of 125 bar (see OP4 in Section 4.1). Although ammonia’s vaporization enthalpy is high, its liquid length-to-nozzle diameter ratio is estimated to be smaller than the ratios of diesel and methanol due to its low boiling temperature.

Table 3.2: Estimated parameters for liquid length calculations based on Higgins et al. [23] for ammonia, diesel and methanol at OP4.

	Ammonia	Diesel	Methanol
$\frac{L_{\text{liq}}}{d_0}$ [–]	47.8	82.0	58.5
$\frac{d_0}{d_{0,\text{diesel}}}$ [–]	1.81	1	1.55
$\frac{L_{\text{liq}}}{L_{\text{liq,diesel}}}$ [–]	1.06	1	1.11

When considering ammonia as an engine fuel, indirect effects on the liquid length caused by the comparatively low heating value and low fuel density must be considered (see Table 3.1). When comparing ammonia to diesel, a significantly larger volume flux is required to supply the same heating value flux to a combustion chamber for ammonia. The volume flux increases with the number of nozzles n , the nozzle diameter d_0 , and the injection velocity U_f (see Equation 2.6). Increasing the nozzle diameter to increase the volume flux will decrease the relative air entrainment at a certain distance from the nozzle (see Equation 2.7). Therefore, less enthalpy is supplied per fuel mass, and liquid length increases. Table 3.2 includes the relative nozzle diameters required to supply the same LHV flux as diesel under the assumption of a constant injection velocity. Furthermore, Table 3.2 shows the resulting liquid lengths relative to diesel when considering the required nozzle diameters. Based on the estimates, ammonia's liquid length is similar to the liquid length of conventional diesel fuel and methanol. While the latent contribution to the energy required for ammonia's vaporization is particularly high due to the large enthalpy of vaporization, the sensible contribution is low as ammonia evaporates already at low temperatures.

As a result of the high latent heat of vaporization and the low evaporation temperature, gas temperatures of ammonia/air mixtures at the liquid length will be low. While the minimum auto-ignition temperature is similar to the boiling temperature for diesel fuel, ammonia will be gaseous several hundred Kelvin below its auto-ignition temperature. In summary, the combination of ammonia's high latent heat of vaporization, low evaporation temperature, low density, and low heating value leads to sprays with cold and less reactive fuel/air mixtures. However, the liquid lengths of ammonia sprays will be moderate, and the impingement of liquid fuel on the cylinder walls may be avoided.

3.2 Flame Stabilization

The flame stabilization behavior of ammonia is vital for its use as direct injection fuel. The following section analyzes the impact of ammonia's physical

properties on the flame stabilization mechanisms introduced in Section 2.3.

The flame speed required for flame stabilization by edge-flame or triple flame propagation is lower than the flow velocity of the fuel/air mixture, as the flow stagnates before the flame front due to volume expansion. However, ammonia's maximum laminar flame speed at atmospheric conditions is almost an order of magnitude lower than that of diesel and methanol (see Table 3.1). In addition, the air mass required per fuel mass to obtain stoichiometric conditions is lower for ammonia than for other fuels (see Table 3.1). As a result, the average flow velocity of ammonia/air mixtures at stoichiometric conditions, i.e. near the triple flame, will be higher than for other fuels due to the conservation of momentum. Therefore, ammonia's physical properties may inhibit flame stabilization via triple flame propagation.

The dominant flame stabilization mechanism for diesel spray flames is auto-ignition supported by re-entrainment of hot combustion products (see Section 2.3). For diesel, the re-entrainment of small amounts of hot combustion products is sufficient to lift the air/fuel mixture to its auto-ignition temperature. This re-entrainment has to be much higher for ammonia than for diesel. In particular, the high auto-ignition temperature of ammonia will harm its ability to develop a stabilized flame via this mechanism. Natural lift-off lengths will increase as more time and space are needed to entrain the amount of products required to undergo auto-ignition. Therefore, the equivalence ratio at the lift-off length will decrease. As a result, the product temperature will decrease as ammonia tends to lean out quickly due to its low stoichiometric air demand. This lower product temperature will again increase the mixing requirements of reactants with products for auto-ignition. A negative feedback loop starts, and the flame may not be able to stabilize in the auto-ignition assisted regime. Chapter 8 elucidates this effect in more detail, supported by simulations and experiments.

3.3 Ammonia Oxidation Pathways

Understanding the chemistry of ammonia oxidation and pollutant formation mechanisms in ammonia flames is crucial when developing new combustion processes for ammonia. While most experimental investigations on ammonia oxidation have been carried out under low temperatures to investigate NO_x removal, newer studies focus on ammonia combustion under higher temperatures and pressures relevant to combustion applications. This section outlines the current understanding of essential oxidation pathways and pollutant formation mechanisms. It is a basis for discussing suitable operating conditions for ammonia combustion in engines (see Section 3.4). The following publications [14, 95, 96], upon which large parts of this section are built, provide more detailed discussions of the relevant mechanisms. Figure 3.1 shows an overview of relevant ammonia oxidation pathways:

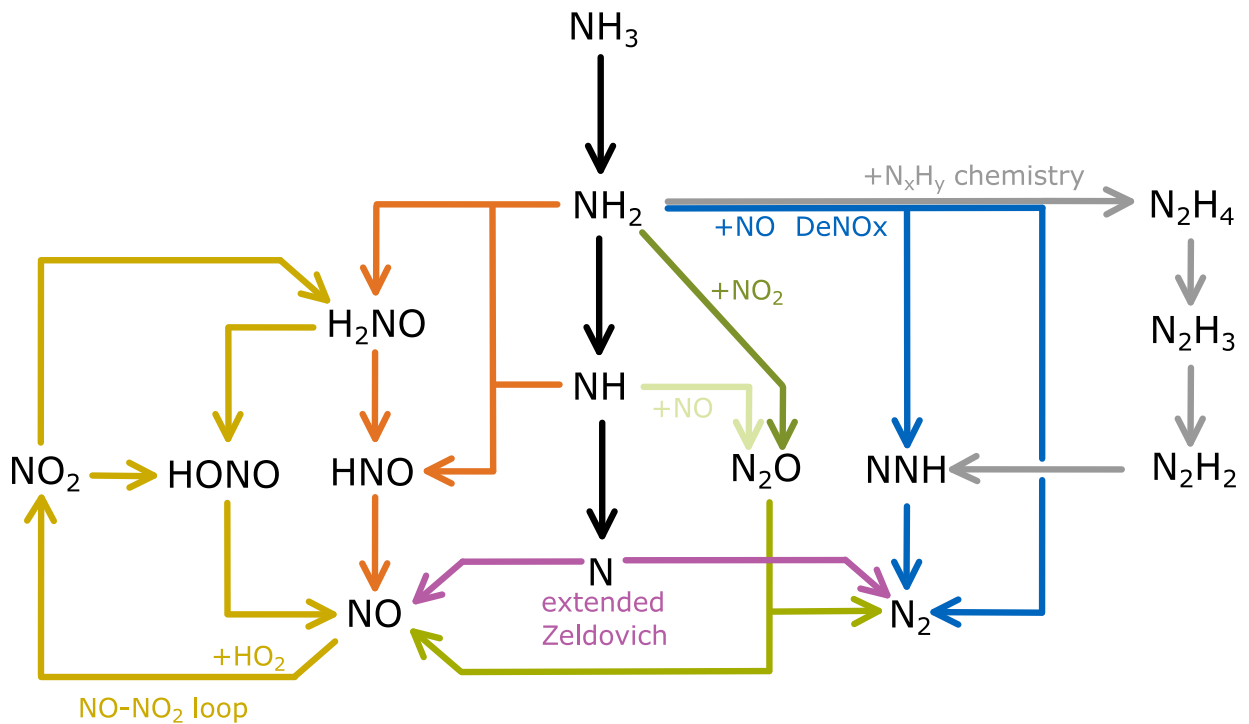


Figure 3.1: Scheme of a reaction pathway diagram for ammonia oxidation. Adapted and extended from [14].

For a molecule used as fuel, ammonia is relatively stable. This stability results from the covalent bonds of the central N atom with the three hydrogen atoms

that require high amounts of energy for dissociation. The molecule undergoes a dehydrogenation reaction to NH_2 in the first step of ammonia oxidation. This reaction generally consumes highly reactive OH, O, and H radicals. For example, the reaction $\text{NH}_3 + \text{OH} \leftrightarrow \text{NH}_2 + \text{H}_2\text{O}$ produces less reactive NH_2 radicals out of highly reactive OH radicals. Therefore, this reaction contributes to the increased first-stage ignition delay of hydrocarbon fuels in the presence of ammonia [97].

Under fuel-rich conditions, the relative importance of O and OH in the radical pool decreases. As a result, the reactions of NH_2 with H (black pathway in Figure 3.1) and other NH_2 radicals (gray pathway) increase, which leads to substantial formation of H_2 . If a lack of oxygen suppresses the oxidation of NH_i , less NO is produced under these conditions. Instead, N atoms become more abundant, which may combine to N_2 via the Zeldovich mechanism (purple pathway) [96]. This recombination represents the reverse reaction of the rate-determining step in thermal NO formation.

The relevance of ammonia oxidation via HNO intermediates (orange pathway) increases for fuel-lean conditions. As HNO explicitly oxidizes to NO, this pathway represents the main route for NO formation in ammonia flames under all conditions [96, 98]. As a result, NO concentrations during ammonia combustion may exceed the thermodynamic equilibrium. The NO formation mechanism marks an essential difference from hydrocarbon flames, where the main route for NO formation is via the Zeldovich mechanism. In the case of hydrocarbons, the rate-determining step is the splitting of the bond of the N_2 molecule contained in the charge air (purple pathway, reversed). As the splitting of the N_2 bonds is slow, the amount of NO generated in hydrocarbon flames is kinetically limited and not by chemical equilibrium. However, the reaction rate increases strongly with increasing temperature, leading to higher NO emissions.

The reduction of NO by adding NH_3 within a specific temperature window was first described by Lyon et al. [99]. Miller et al. [100] later attributed this phenomenon to NO reacting with NH_2 (blue pathway). This thermal DeNO_x mechanism exceeds NO formation between 1100 K and 1400 K. For higher temperatures, NO formation via HNO intermediates exceeds its consumption.

The reaction of NO and NH₂ may form NNH intermediates or react directly to N₂, referred to as tunneling. While the tunneling reaction NH₂ + NO ↔ N₂ + H₂O is chain-terminating, the reaction via NNH intermediates is chain-branching and produces reactive H and OH radicals. Therefore, determining the branching fraction is crucial for modeling ammonia combustion [101].

N₂O is either generated by the reaction of NH with NO that dominates for low O₂ levels, or by the reaction of NH₂ with NO₂ that dominates for high O₂ concentrations (green pathway) [102]. Subsequently, N₂O is mainly consumed via reaction with H radicals and its thermal decomposition to form either N₂ or NO [103]. Therefore, N₂O emissions result from low combustion temperatures, where H radicals are scarce and thermal decomposition is slow [104].

The primary mechanism for NO₂ formation is NO oxidation via the reaction NO + HO₂ ↔ NO₂ + OH. The NO₂ formed is then recycled to ammonia directly or via intermediate species, such as H₂NO (NO-NO₂ loop, yellow pathway) [98]. This process converts less reactive HO₂ radicals into more reactive OH radicals. Significant amounts of HO₂ may be formed during ammonia ignition and at large excess air ratios, leading to increased conversion of NO to NO₂ [95].

In summary, ammonia combustion processes that favor the the black and gray pathways lead to low NO_x and N₂O formation. These pathways are particularly active for fuel-rich conditions.

3.4 Pollutant Formation Characteristics

This section elucidates the pollutant formation behavior of ammonia combustion under engine-relevant conditions. Therefore, $\Phi - T$ maps reveal ammonia combustion's pollutant formation characteristics. In addition, the impact of various combustion strategies and engine measures is discussed.

The $\Phi - T$ maps build on constant pressure reactor simulations with a constant temperature constraint in *Cantera*. The constant pressure reactor does not consider mass fluxes out of or into the reactor. The simulations are conducted

with a pressure of 120 bar, a residence time of 2 ms, and an oxygen content of 21% to resemble the conditions in the RCEM employed. 2 ms is a representative time scale for engine combustion and corresponds to 12 CAD at 1000 rpm. The reaction mechanism by Glarborg et al. is used [95]. The ammonia maps consider NO and N₂O formation. In addition, the $\Phi - T$ maps in this work include states that result from mixing liquid fuel injected at 293 K and charge air at 920 K in the RCEM. The analysis only includes states at which fuel is completely vaporized. The mixture fraction at which fuel completely evaporates corresponds to a saturated condition in thermodynamic equilibrium with the ambient gas. The temperature at this saturated condition defines the fuel's partial pressure via the saturation curve. The fuel mass fraction, at which this saturated state is obtained, can be determined by solving mass- and energy balances and the real gas equation of state for two mixing streams of fuel and ambient air. The calculation method is outlined in Siebers et al. [105] and similar to droplet evaporation considerations. The physical properties are from the NIST database [18]. Complete ammonia evaporation occurs for an equivalence ratio of 3.2 at 356 K under the investigated conditions. In contrast, n-heptane evaporates fully at an equivalence ratio of 9.8 at 490 K. The lower stoichiometric air demand of ammonia causes this difference. Furthermore, the maps show states corresponding to the adiabatic combustion of the mixtures obtained.

The $\Phi - T$ map for ammonia combustion (Figure 3.2) reveals that notable amounts of NO already form for combustion temperatures as low as 1500 K. In addition, N₂O forms at low temperatures regardless of the equivalence ratio. The formation of NO via HNO intermediates, introduced in Section 3.3, causes a rapid rise of NO concentrations above the thermodynamic equilibrium at fuel-lean conditions. As a result, NO formation is not kinetically limited via the Zeldovich mechanism and does not require high temperatures. Figure 3.3 shows NO concentrations at chemical equilibrium for the same conditions as in Figure 3.2. NO concentrations in equilibrium are slightly lower than after 2 ms residence time. Therefore, opposite to hydrocarbon combustion, the Zeldovich mechanism reduces super-equilibrium NO concentrations over a wide range of conditions for ammonia combustion (see Section 3.3). Nonetheless, the temperature dependence of the thermodynamic equilibrium will lead to

more NO formation for higher combustion temperatures. Furthermore, Figure 3.2 shows that NO formation drops sharply compared to hydrocarbons (see Section 2.4) when conditions become slightly fuel-rich. This drop results from a surplus of NH_2 and NH radicals for these conditions, leading to NO reduction.

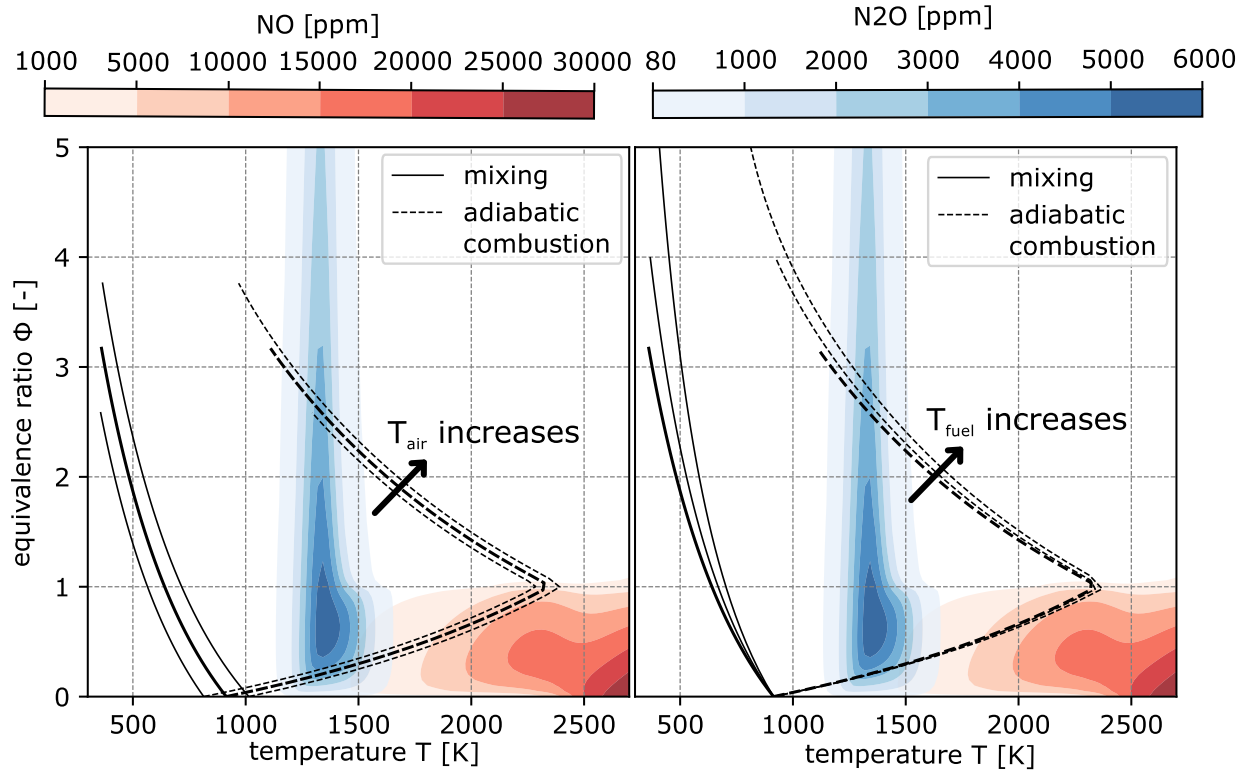


Figure 3.2: $\Phi - T$ maps showing air pollutant forming conditions (NO, N_2O) for the combustion of ammonia at 120 bar after 2 ms residence time. The lines indicate the states resulting from mixing and adiabatic combustion of ammonia and air. Mixing and adiabatic combustion lines are included for charge air temperatures of 820 K, 920 K (thick line), and 1020 K at a fuel injection temperature of 293 K (left), and fuel injection temperatures of 293 K (thick line), 343 K, and 393 K at a charge air temperature of 920 K (right).

N_2O concentrations in thermodynamic equilibrium are close to zero for all temperatures and equivalence ratios investigated (and are therefore not included in Figure 3.3). As N_2O is an intermediate product of ammonia com-

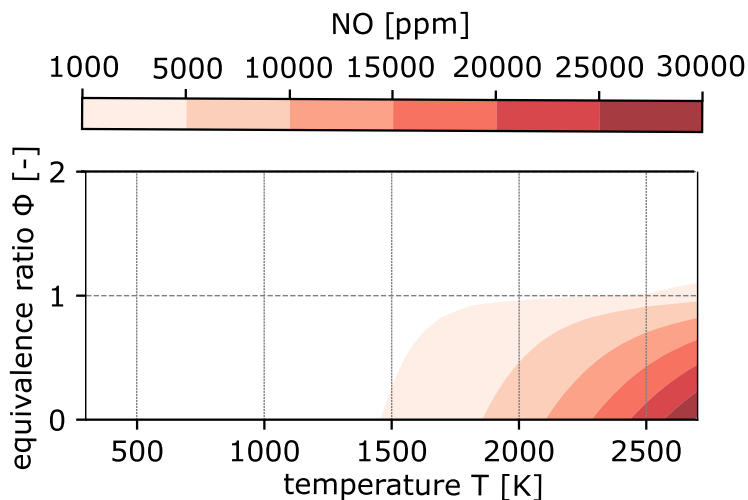


Figure 3.3: $\Phi - T$ map showing NO concentrations in thermodynamic equilibrium for ammonia combustion.

bustion, it only persists for incomplete conversion. According to the adiabatic combustion lines in Figure 3.2, N_2O forms at intermediate or extremely low equivalence ratios. If N_2O forms at intermediate equivalence ratios, it will continue mixing with air and burn diffusively, increasing the temperature. Therefore, N_2O will thermally decompose or react with H radicals (see Section 3.3). As a result, the N_2O present in the exhaust gas of engines is likely to originate from ultra-lean combustion, where subsequent mixing will decrease temperatures and inhibit further reactions of N_2O . In addition, quenching of ongoing reactions that are not accounted for in the $\Phi - T$ maps discussed, e.g. due to wall interaction, may contribute to N_2O emissions.

Fuel-rich combustion of ammonia has the potential to avoid NO and N_2O formation almost entirely. Okafor et al. [103] used this effect under gas turbine conditions. They achieved high fuel conversion and low pollutant formation using staged combustion, with the primary stage operating slightly rich in stoichiometry. The following lean stage converted the remaining fuel. For diesel combustion, the fuel-rich partially premixed combustion and subsequent burnout in the diffusion layer (see Section 2.2) represent conditions similar to staged combustion. However, equivalence ratios differ spatially and temporally for spray combustion and are challenging to control. In general, mean equivalence ratios decrease with increasing distance from the injector

nozzle, which presents a possible method to influence equivalence ratios (see Section 2.1).

$\Phi - T$ maps can evaluate further engine measures and combustion strategies. Figure 3.2 includes the effects of charge air and fuel injection temperature variations. Increasing the fuel temperature causes ammonia to evaporate already at higher equivalence ratios, leading to higher mixing and combustion temperatures. The effect is limited as the sensible contribution to the energy required for ammonia vaporization is small (see Section 3.1). Furthermore excessive preheating causes flash-boiling due to the sudden pressure drop during injection, which significantly alters spray behavior (e.g. [106, 107]). The effect of preheating is stronger for fuel-rich conditions, as the share of the mixture's enthalpy from the fuel decreases for leaner conditions. Therefore, the small increase in temperature at fuel-lean conditions only slightly changes NO and N₂O formation for a given equivalence ratio. However, the increased mixture reactivity at fuel-rich conditions might lead to a larger share of fuel burning at fuel-rich conditions. In contrast, increasing the charge air temperature shifts the mixing and combustion curves at all equivalence ratios shown to higher temperatures (it only does not shift the curves at infinite equivalence ratios). As a result, more NO and less N₂O form by lean combustion. In addition, higher reactivity of fuel-rich mixtures will again facilitate fuel-rich combustion.

Figure 3.4 shows the effect of charge pressure and residence time via the 500 ppm iso-lines of NO and N₂O. The other parameters remain unchanged compared to the maps above. Ammonia combustion, and therefore N₂O formation, shifts to lower temperatures for increased pressures. In addition, the N₂O formation region broadens. NO formation at slightly fuel-rich conditions reduces for increasing pressures, which increases the range of conditions at which low NO formation can be achieved. Therefore, increasing pressures may lower NO formation, while the effect on N₂O formation is rather weak. Increasing residence times enable ammonia combustion for lower temperatures and increase the conversion of N₂O for the same temperatures. As a result, N₂O forming regions shift to lower temperatures. The increasing residence times also enable NO to approach the thermodynamic equilibrium. Therefore, super-

equilibrium NO in the reaction zone is consumed, and NO only persists under fuel-lean conditions. Consequently, longer residence times decrease NO and N₂O emissions for ammonia combustion. However, the intermittent working principle of reciprocating engines limits the residence time available.

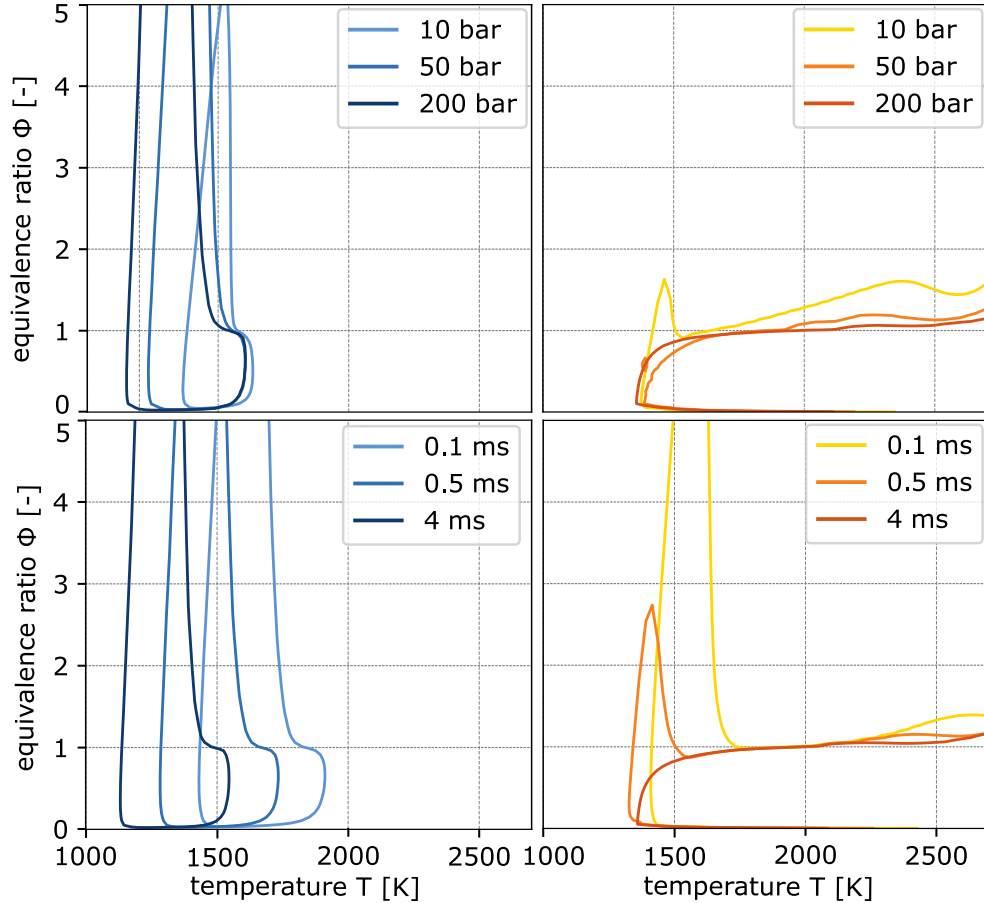


Figure 3.4: $\Phi - T$ map showing 500 ppm iso-lines for N₂O (left) and NO (right) for charge pressures of 10 bar, 50 bar, 200 bar (top) and residence times of 0.1 ms, 0.5 ms, 4 ms (bottom).

The $\Phi - T$ maps discussed in this work only consider pure ammonia as fuel. By including n-heptane into similar considerations, Pedersen et al. [108] illustrate the impact of various ammonia/diesel blending ratios on pollutant formation, including ammonia's impact on soot formation characteristics. However, for the combustion process investigated in this work, Section 7 reveals that most ammonia burns without the influence of diesel combustion species.

In summary, the pollutant formation behavior observed for ammonia differs remarkably from that described for hydrocarbons in Section 2.4. As NO and N₂O formation occur for lean conditions for all temperatures relevant for engines, conventional low-temperature combustion techniques are unsuitable for avoiding air pollutant formation for ammonia. In contrast, slightly fuel-rich or staged combustion shows promising pollutant formation behavior. Furthermore, lower lift-off lengths, increased fuel and charge temperatures, as well as longer residence times are beneficial regarding air pollutant formation. These conditions are typical for large heavy-duty engines operating at high loads making them particularly promising for achieving low air pollutant emissions when using ammonia as fuel.

Engine designers must consider the air pollutant emissions of engines in conjunction with exhaust gas after-treatment system characteristics. For example, selective catalytic reduction (SCR) after-treatment systems require equal amounts of NO_x and NH₃ to convert both air pollutants to mainly N₂ and H₂O. Therefore, additional NO_x formation may be desired if NH₃ emissions are high. However, initial investigations on ammonia spray combustion should explore pathways and measures to directly reduce all kinds of air pollutants in the engine.

3.5 Challenges for Ammonia Spray Combustion

The considerations in this chapter reveal characteristics of ammonia sprays under diesel engine conditions:

- Temperatures in ammonia sprays are extremely low, leading to unreactive fuel/air mixtures.
- Ammonia's low flame speed and high auto-ignition temperature, in combination with low educt and product temperatures, may inhibit flame stabilization via the most accepted flame stabilization mechanisms.
- The air pollutants NO and N₂O form excessively under fuel-lean conditions.

This behavior results in the following challenges for ammonia spray combustion:

- The fuel/air mixtures in ammonia sprays are cold and unreactive. Therefore, an additional pilot fuel injection is required to ignite the ammonia sprays. The requirements for successful ignition and combustion of the ammonia sprays via the diesel pilot are unknown.
- A lack of flame stabilization might lead to a blow-out of the ammonia flame.
- A fundamental conflict of ammonia combustion arises from an interaction of the abovementioned effects. Poor flame stabilization behavior leads to longer lift-off lengths, enabling more air to be entrained up to the lift-off. As a result, fuel/air mixtures lean out at the jet edges facilitated by ammonia's low stoichiometric air demand. Combustion of the resulting cold and lean mixtures causes excessive pollutant formation.
- The low reactivity of ammonia sprays facilitates high levels of unburned ammonia emissions.

The following chapters of this dissertation attempt to advance the knowledge of piloted ammonia spray combustion beyond the understanding provided by the theoretical considerations conducted in this chapter.

4 Experimental Setup

The experiments are conducted in a pneumatically driven RCEM that allows the direct injection of ammonia. Additional diesel pilot injections ignite the ammonia sprays. The first section outlines the setup and operating principle of the RCEM. Then, the fuel injection system is introduced. Subsequently, the optical measurement techniques applied are presented, including SG, MS, OH* CL, NL, and spectroscopic imaging. Furthermore, the chapter introduces the exhaust gas analysis setup, as well as the controls and data acquisition system. The final section of this chapter estimates the experimental uncertainties.

The test rig and the experimental procedure incorporate several safety measures to account for ammonia's toxicity. Most importantly, a separate control room is used to limit the risk of exposure to the operator. Furthermore, gas masks are kept available when the test rig is operated. A stationary gas warning system controls the ammonia concentration at four locations. At 30 ppm, which corresponds to the acute exposure guideline level (AEG) 1, at which reversible symptoms of intoxication occur [109], the control system triggers a signal light and increases the laboratory ventilation strongly. At 60 ppm, the ammonia supply is shut off, and a siren sounds.

4.1 Rapid Compression Expansion Machine

The machine acts as a single-shot engine, simulating isolated strokes of internal combustion engines. In contrast to rapid compression machines (RCMs) used for chemical kinetic studies, the RCEM shows engine-like piston trajectories close to TDC. A glass piston enables optical access into the combustion chamber. The main advantage of the RCEM is its large flexibility, as charge conditions, injection pressures, injection timings, and the injector arrange-

ment can be altered swiftly. The large bore diameter (220 mm) allows a long free penetration length of the fuel sprays before wall-impingement occurs. Therefore, the RCEM allows investigating undisturbed, freely propagating fuel sprays. In addition, the variable stroke (up to 380 mm) enables varying, high compression ratios. The RCEM was designed by Dorer et al. (e.g. [110]) and has already been used to investigate the diesel-piloted combustion of methane [70, 111].

Figure 4.1 shows the driving mechanism of the RCEM. The RCEM consists of two concentrically arranged ring pistons coupled kinetically by hydraulic oil. Before each experiment, the driving-air bottles are filled with pressurized air. After starting the experiment, the outer piston, which is hydraulically coupled to the inner piston, accelerates. As a result, the inner working piston accelerates in the opposite direction, which cancels net momentum and reduces unwanted vibrations. The compression stroke ends at TDC when a dynamic equilibrium is reached, and the expansion stroke starts.

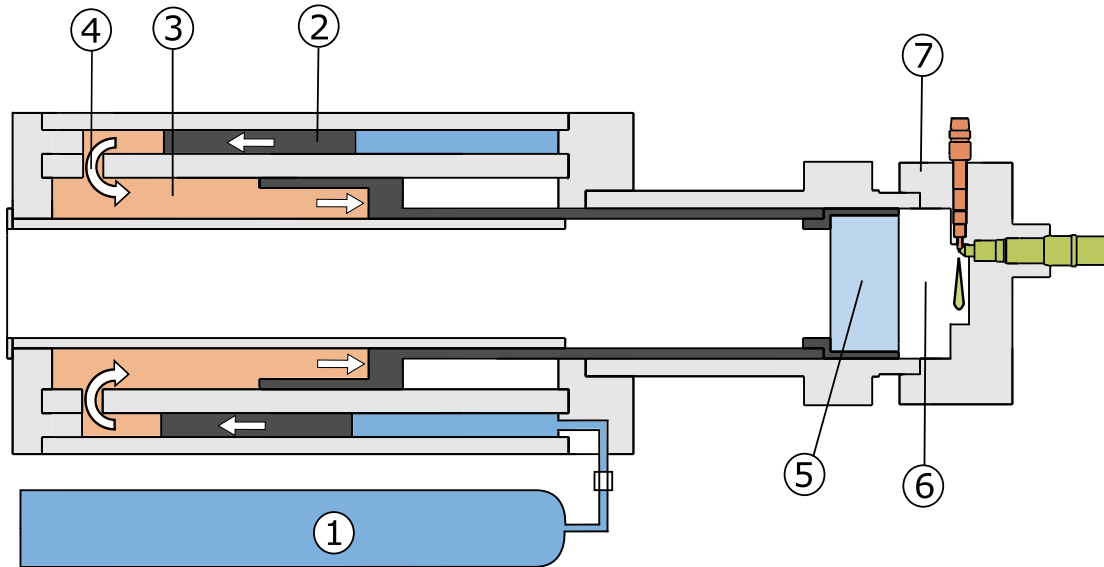


Figure 4.1: RCEM driving system: ① driving-air bottles, ② driving piston, ③ hydraulic fluid, ④ flow orifice, ⑤ working piston, ⑥ combustion chamber, ⑦ cylinder head.

Driving pressure, flow resistance, and the initial combustion chamber pressure determine the piston trajectory. Therefore, the piston trajectory depends on

the operating conditions. For the operating points investigated in this dissertation, the piston moves similar to an engine operating at 800 – 1000 rpm (see Table 4.1). The combustion chamber pressure is measured during the experiment using a Kistler 7061C piezo-electric pressure transducer. An inductive linear incremental encoder measures the piston position. A thermocouple measures the temperature before the experiment. During the experiment, the temperature is calculated under the assumption of an undisturbed gas core that undergoes isentropic compression. This assumption is valid when flat pistons and large crevice volumes prevent charge motion and roll-up of the boundary layer [112], as in the RCEM employed. As a result, the core temperature of the charge follows the equation:

$$T = T_0 \epsilon_{\text{eff}}^{\kappa(T)-1}. \quad (4.1)$$

Cold walls and large crevice volumes lead to significant heat losses during compression. Thus, the effective compression ratio of the adiabatic core is calculated from the pressure ratio:

$$\epsilon_{\text{eff}} = \frac{v_0}{v} = \left(\frac{p}{p_0}\right)^{1/\kappa(T)}. \quad (4.2)$$

The investigated operating conditions at TDC of unfired experiments are listed in Table 4.1 and represent a load range from low-load (OP1) to medium-to-high-load (OP4) engine conditions. The total air mass and the global equivalence ratio in the RCEM depend on the initial charge pressure, which differs between the OPs. However, this has little effect on combustion, which is mainly determined by local equivalence ratios within the spray. In engines, temperature and pressure increase during combustion. However, this increase is negligible in the RCEM due to the small amounts of fuel used (see Section 4.2).

Figure 4.2 shows the cylinder head and injector arrangement. Two single-hole injectors inject each fuel separately. The fuel sprays interact in a plane parallel

Table 4.1: Investigated operating points.

parameter	OP1	OP2	OP3	OP4
TDC temperature [K]	780 ± 8	829 ± 10	865 ± 10	920 ± 10
TDC pressure [bar]	75 ± 1.5	88 ± 2	98 ± 2	125 ± 2
$\epsilon_{\text{eff}}[-]$	12.9	14.6	17.2	20.5
equivalent engine rpm [$\frac{1}{\text{min}}$]	≈ 800	≈ 880	≈ 920	≈ 1000

to the cylinder head. The ammonia injector can be rotated to obtain different relative spray angles α . Reduction rings decrease the effective diameter of the combustion chamber and allow for sufficient distance between the quartz-glass piston surface and the mirror surface for an undisturbed spray propagation of ammonia and diesel. The mirror used for the optical double-pass measurement techniques, described in Section 4.3, consists of a polished stainless steel plate. The pressure sensor is mounted behind the reduction rings. A large orifice connecting the cavity of the pressure sensor and the combustion chamber reduces pressure oscillations between the two chambers. An inner and outer eccentric can be rotated freely to adjust the position of the ammonia injector. The distance between the two nozzles is small and resembles the geometric configuration of HPDF injectors in four-stroke engines. These injectors usually only consist of one injector body with closely spaced nozzles. A distance of $x = 10 \text{ mm}$ and $y = 5 \text{ mm}$ is chosen (see Figure 4.2), which resembles the distances of the full HPDF injector used by Stenzel et al. [5]. The interaction angle α varies between -15° and $+15^\circ$ to investigate the effect of different spatial spray interactions.

4.2 Fuel Injection

Single-hole injectors inject the fuels on a plane parallel to the flat piston surface to study the interaction between the two sprays in detail. The diesel injection timing is kept constant at 2ms before TDC, while the ammonia injection timing is shifted relative to TDC. Thus, the setup allows the variation of the temporal and spatial interaction of the two sprays. While the diesel

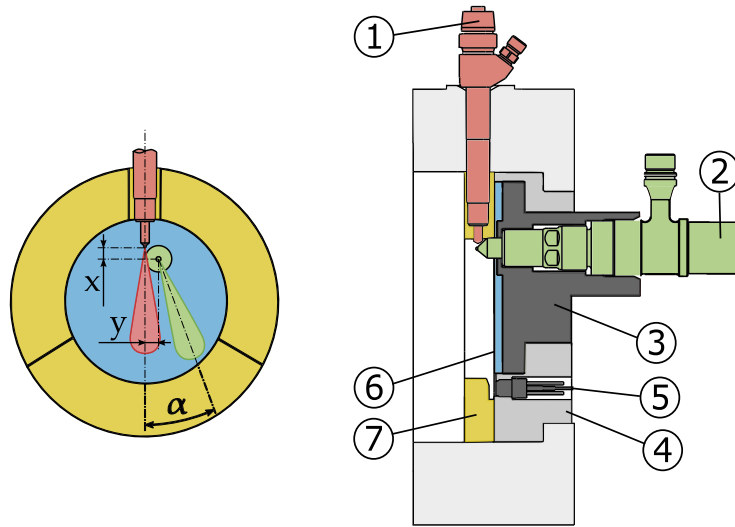


Figure 4.2: Cylinder head: ① diesel injector, ② ammonia injector, ③ inner eccentric, ④ outer eccentric, ⑤ pressure transducer, ⑥ mirror, ⑦ reduction ring.

injection pressure is not adapted to part-load cases, the ammonia injection pressure is adapted to the back pressure of the respective OP to keep the injected amount of ammonia and the injection time constant. The ammonia injection time and the injected LHV of ammonia match those of methane in previous works on methane/diesel HPDF combustion at the test rig [70, 111].

The injectors were analyzed in an IAV injection analyzer using calibration fluid. Coppo et al. [113] showed that the opening and closing behavior of injectors is not affected by changing the fuel. Therefore, the shape of the injection mass flux remains unchanged for ammonia (e.g. the injection rate ramp-up during injector opening and the injection duration). Gaucherand et al. [114] pointed out that ammonia may show significantly lower injection volume fluxes than other fuels due to intense cavitation under engine-relevant conditions, particularly when the fuel is preheated. This behavior results from the proximity of ammonia to the two-phase region. Therefore, ammonia was injected into the RCEM combustion chamber under non-reacting conditions (i.e. no pilot injection) for two exemplary test cases. The resulting concentration in the combustion chamber was measured using the exhaust gas analysis system described in Section 4.4. As the air mass in the RCEM is known, the

injected ammonia masses could be calculated. The experimentally determined injection masses were similar to the calculated ammonia injection masses when assuming the same volume flux for ammonia as measured for hydraulic oil. Therefore, this method is used to calculate ammonia injection masses in this work. Section 4.6 presents the associated uncertainties. Following Bernoulli’s equation, the injected ammonia volume flux should be slightly higher than the hydraulic oil volume flux injected with the same injection pressure due to ammonia’s lower density. This discrepancy hints at increased cavitation when injecting ammonia. Determining more accurate mass flux profiles of ammonia requires injection analyzers operating directly with ammonia. As discharge coefficients depend on fuel temperature and counter pressure for ammonia, these injection analyzers must consider these parameters additionally. Furthermore, only a finite number of injection cases were tested in the IAV injection analyzer. Therefore, the rate profiles are parametrized and approximated by top-hat profiles to allow interpolation between the tested combinations, as described in [115].

Three different single-hole nozzles with injection hole diameters of 0.75 mm, 0.94 mm, and 0.98 mm respectively, are mounted on a custom Woodward L’Orange injector to inject ammonia. Table 4.2 shows the ammonia injection parameters. The standard configuration features the 0.94 mm nozzle and injects 210 mg of ammonia in 2700 μs with a relative injection pressure of 405 bar. Therefore, absolute injection pressures of the standard configuration range from 480 bar to 530 bar.

Table 4.2: Ammonia injection parameters.

nozzle diameter [mm]	ammonia mass [mg]	injection pressure [bar]	injection duration (hydraulic) [μs]	used in Chapters [-]
0.94	125, 210	480 – 530	2700	6, 7, 8
0.98	125 – 220	265 – 560	2700	8,9
0.75	125	435	2700	9

For diesel, two different nozzle tips with orifice diameters of 110 μm and 200 μm , respectively, are attached to a type CRI 2.20 Bosch injector. This

procedure permits the variation of the injected diesel amount over a wide range without extremely different injection timings and pressures. Table 4.3 shows important characteristics of the examined diesel injections. The standard configuration used for most experiments injects 5 mg of diesel in 520 ms via the 0.2 mm nozzle.

Table 4.3: Diesel injection parameters.

nozzle diameter [μm]	diesel mass [mg]	injection pressure [bar]	injection duration (hydraulic) [μs]	LHV fraction for 210 mg ammonia [–]
200	10	2000	830	10.0%
200	5	2000	520	5.2%
110	5	2000	1460	5.2%
110	3	2000	850	3.2%
110	1.5	2000	570	1.6%
110	0.9	1100	560	1.0%

Air-driven high-pressure pumps (Maximator G400-2 for diesel and Maximator G150-2 with EPDM gaskets for ammonia) supply the fuels. Figure 4.3 shows the ammonia injection system. The ammonia is pre-pressurized in an intermediate storage tank to avoid cavitation during the suction stroke of the ammonia pump. This approach is similar to the setup of Ryu et al. [116] for ammonia/DME mixtures. The ammonia fuel line features an additional counter-pressure valve that creates a back-pressure of 15 bar in the leakage stream after the fuel injector. The increased pressure inhibits fuel evaporation within the injector, which would deteriorate injector behavior. The ammonia leakage stream is directed into a large water container, which acts as an acid trap. Most fuel supply system components are located in a ventilated gas cabinet. Furthermore, the fuel line includes burst disks to protect the system from too high pressures. In addition, the fuel line includes pressure transducers and filters.

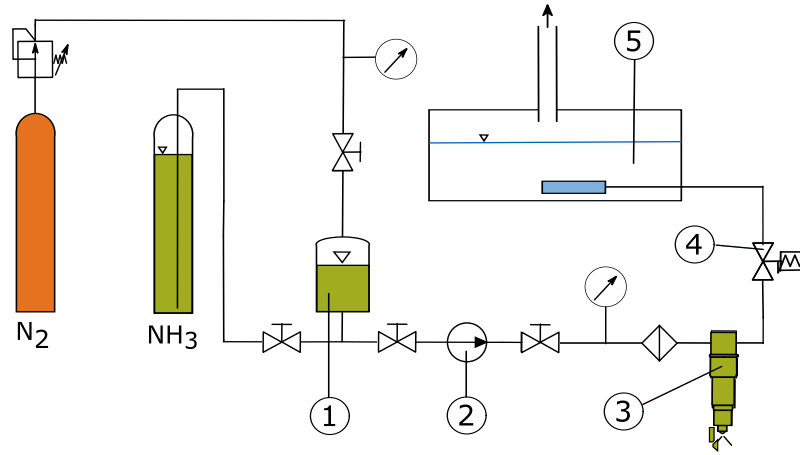


Figure 4.3: Ammonia injection system: ① intermediate storage tank, ② ammonia pump, ③ ammonia injector, ④ back-pressure valve, ⑤ acid trap.

4.3 Optical Measurement Setup

This section presents the optical measurement techniques used in this work. While MS, NL, and spectroscopic imaging can only be applied one at a time, SG and OH* CL images are taken simultaneously during the experiments. Combining these two measurement techniques allows a detailed spatial allocation of OH* CL emissions to the spray structures. The optical access is reduced to the piston only, which reduces leakage and increases the HRR's quality. The following subsections introduce the SG, MS, OH* CL, and spectroscopic imaging setups. In addition, the underlying fundamentals are outlined briefly. The natural flame emission imaging setup is not described in more detail, as it consists only of the Photron Fastcam SAX high-speed camera and a lens. Figure 4.4 shows the SG, OH* CL, and MS setup.

4.3.1 Shadowgraphy Imaging

The Shadowgraphy method is similar to the Schlieren method. The structures visible on SG images result either from light attenuation (e.g. on droplets) or deflection of light passing through density gradients. In addition, light emitted

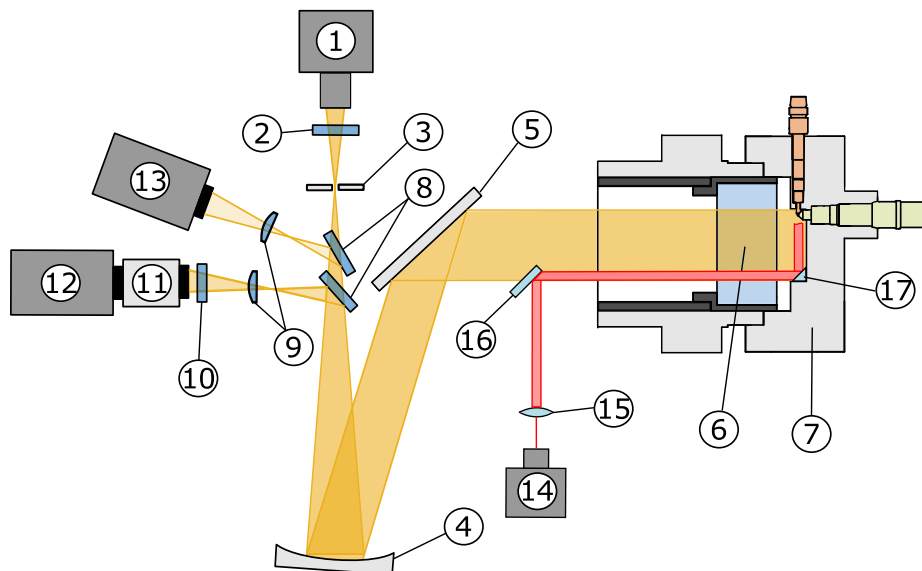


Figure 4.4: SG, MS, and CL optical setup: ① xenon arc lamp, ② UV filter, ③ pin hole, ④ concave mirror, ⑤ planar mirror, ⑥ quartz-glass piston, ⑦ cylinder head with mirror, ⑧ beam splitter, ⑨ focusing lens, ⑩ bandpass filter, ⑪ image intensifier, ⑫ high-speed camera (CL), ⑬ high-speed camera (SG/MS), ⑭ continuous laser 532nm, ⑮ sheet-forming optics, ⑯ planar mirror, ⑰ 45° mirror.

from the observed test model can also be detected (e.g. soot luminosity from diesel flames). While the deflected light is blocked for Schlieren imaging by a knife edge, it passes on to the screen for SG imaging and creates an irregular distribution of light. Therefore, regions with density gradients appear darker in SG images as light is deflected from the corresponding path. Due to the deflected light, areas surrounding density gradients appear brighter. Figure 4.5 depicts a schematic SG setup and its working principle. Local differences in light speed cause light deflection in density gradients. The two points on the wavefront 1 (A and B) are located at a distance, dr , propagating with the respective light velocities of c and $c + dc$. After the time interval dt , the new wavefront 2 will have moved a larger distance at point B than it has at point A . This results in a rotation of the propagation direction by the infinitesimal angle β . Further information can be found in the literature (e.g. [15]).

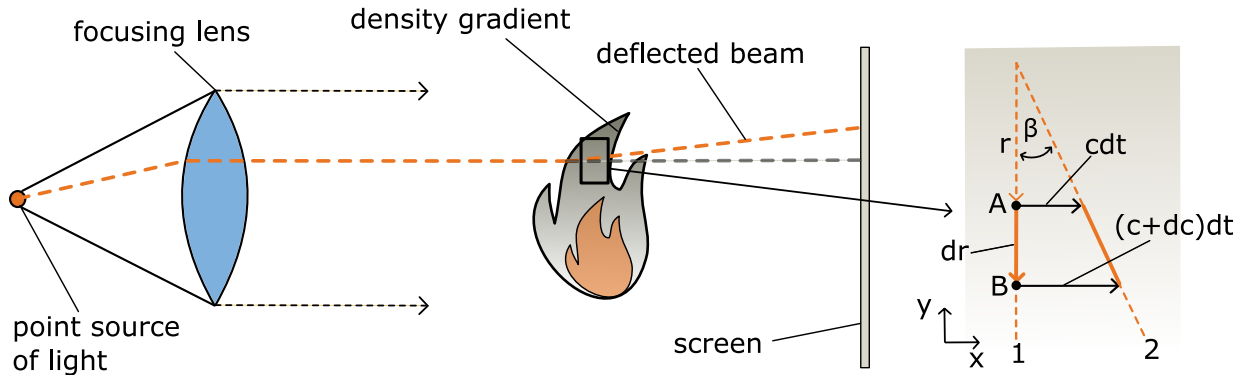


Figure 4.5: Schematic of an SG setup and its working principle. Adapted from [15].

The employed SG setup (see Figure 4.4) uses a xenon arc lamp ① as the light source which, in combination with a pin-hole ③, serves as the point source of light. The pin-hole is located at the focal point of a large concave mirror ④, which replaces the focusing lens. A planar mirror ⑤ redirects the light into the RCEM, where it is reflected on a polished stainless steel surface in the cylinder head ⑦ (see Figure 4.2). As the light beam is redirected along the same trajectory, it illuminates the injection and combustion event twice. However, as the distance between the first and second pass is low compared to the whole optical length, this has a minor influence on the resulting SG image. A beam splitter ⑧ redirects the reflected light beam into a focusing lens ⑨ and on the camera's sensor ⑬. The employed double-pass setup enables SG measurements in the plane parallel to the piston without a second optical access, which loses design restraints and enables the injector setup used in this work.

4.3.2 OH* Chemiluminescence Imaging

OH* CL is observed simultaneously with SG imaging (see Figure 4.4). The flame emissions, which follow the same trajectory as the light beam used for the SG imaging, are redirected by a UV beam-splitter ⑧ and focused via a focusing lens ⑨. A bandpass filter centered at 307 nm with an FWHM of ± 10 nm ⑩ filters the incoming light. Any UV radiation from the xenon

arc lamp is filtered with a UV long-pass filter ② directly after the lamp. A Hamamatsu C10880 image intensifier ⑪ increases the incoming light intensity before it is detected by the camera ⑫. Section 2.5 describes the fundamentals of CL in more detail.

4.3.3 Mie-Scattering Imaging

The MS technique is commonly applied to investigate the liquid phase of fuel sprays (e.g. [48, 117, 118]). MS is an elastic scattering process that does not alter the wavelength of scattered light. It occurs if light interacts with scattering particles, such as dust particles or droplets, that are large compared to the wavelength. Droplets in diesel sprays usually have mean diameters of several μm and, therefore, meet this criterion [119]. Changes in electrical and magnetic properties near the particle determine the scattering process, which the Mie theory and the 3-D Maxwell equations can describe. The outgoing light changes phase, amplitude, and polarization. Light waves originating from different spots of the particle interact and form a characteristic pattern. Therefore, the intensity of scattered light strongly depends on the angle of observation. The highest intensities result through forward scattered light. However, most practical applications of MS observe light scattered perpendicularly (e.g. [48, 117, 118]).

The MS setup (see Figure 4.4) uses the SG setup's camera, lens, and beam splitter. A continuous laser (Coherent Genesis CX 514-4000), with an output power of 2 W, supplies the laser beam for MS. Subsequently, sheet forming optics create a laser sheet, and a planar mirror redirects the light sheet into the combustion chamber. After passing the quartz-glass piston, a 45° mirror mounted inside the combustion chamber redirects the laser sheet onto the ammonia spray axis. The laser sheet covers a distance of approximately 25 mm to 65 mm from the injector nozzle. The scattered light that follows a trajectory onto the camera sensor is detected. Furthermore, the mirror redirecting the laser sheet into a plane parallel to the piston surface has to be covered from the camera's field of view to avoid too high light intensities from reflections. Therefore, the spray is rotated by 15° for MS experiments to increase

the distance between the spray and the mirror, which facilitates covering the mirror.

4.3.4 Spectroscopy

Figure 4.6 shows a scheme of the spectroscopy setup. A Cerco UV lens with a focal length of 100 mm collects light emitted by the combustion event and projects it onto the 10 μm slit of the monochromator. The SpectraPro 275 spectroscope from Acton Research Corporation is a Czerny-Turner type monochromator. It allows changing between different gratings, which feature different densities of grooves per mm and result in different spectral dispersions. In this work, a grating with 150 grooves per mm is used to resolve the CL in the UV-VIS range from 275 – 750 nm with a spectral resolution of 1 nm (grating 3), while 600 grooves per mm are used to resolve the UV range from 275 nm to 400 nm with a higher spectral resolution of 0.25 nm (grating 2). The Hamamatsu C10880 image intensifier, coupled with Photron Fastcam SAX2, records the spectra at the outlet of the monochromator. For OP3, flame emissions in the UV-VIS range are recorded with 20000 fps, while longer exposure times are necessary for the UV range, resulting in a frame rate of 10000 fps. For the highly reactive case OP4, the soot luminosity of the pilot fuel prohibits any investigations in the visible wavelengths, as soot intensity exceeds the chemiluminescence intensity by far. The UV emissions are brighter than in the less reactive case and are recorded at 20000 fps. Different image intensifier gains prohibit a comparison of the flame emission intensities obtained for different combustion cases. Therefore, the results do not provide absolute intensity values for some cases. Section 5.2.3 presents the post-processing and calibration procedures.

4.4 Exhaust Gas Analysis

During the expansion stroke following the combustion event, in-cylinder temperatures drop quickly due to charge expansion and rapid heat loss to the cold cylinder walls. This process is accompanied by homogenization of the charge,

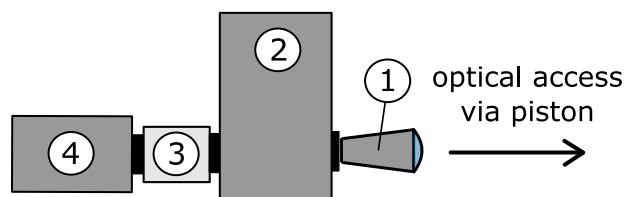


Figure 4.6: High-speed spectroscopy setup: ① UV lens, ② monochromator, ③ image intensifier, ④ high-speed camera.

resulting in extremely lean mixtures due to the low global equivalence ratios of $\Phi \approx 1/30$. As a result, ongoing reactions quench. As compressed air still pressurizes the piston directly after the experiment, the charge is recompressed and kept at elevated pressures and temperatures for several seconds before the piston moves back into its starting position. The effect of these elevated charge conditions on the charge composition is evaluated using constant volume reactor simulations with the chemical kinetic mechanism developed by Glarborg et al. [95] in *Cantera*. The simulations assume a homogenous charge equal to the measured exhaust gas composition or slightly more reactive mixtures. The simulation results show no significant changes in charge composition during the relevant timescales. This low reactivity results from the low overall global equivalence ratios. Therefore, the measured exhaust gas compositions result from the initial combustion event. In addition, condensation on the unheated walls of the RCEM must be carefully avoided. Therefore, only small amounts of ammonia (125 mg) and diesel (5 mg) are burned to keep the condensation temperature of the burned charge after combustion below 18 °C. The room is heated to 25 °C. As a result, the charge temperature before combustion and after expanding the charge into the initial position ranges between 26 °C and 28 °C. Higher global equivalence ratios than those used in this work cannot be reliably investigated in the RCEM, as a higher vapor content in the exhaust gas causes condensation, and reactions would resume during recompression of the charge.

After each experiment, the piston quickly moves into its starting position, the exhaust gas valves open, and the charge flows through the exhaust gas analysis system. Each experiment's exhaust gas concentrations are measured for 10 minutes after initial transients. An exhaust gas analysis system by

ABB (Advanced Optima 2020 series) analyzes the gas composition. Figure 4.7 shows a scheme of the exhaust gas system. First, a Limas 21 HW gas analyzer detects NH_3 using component-specific non-dispersive UV (NDUV) absorption. Then, a reaction section fed with phosphoric acid removes NH_3 to avoid the formation of ammonium bicarbonate - a salt that is formed below 59°C by the reaction of NH_3 with CO_2 and H_2O . The deposition of this salt in the gas analyzers causes damage and leads to erroneous measurements. In addition, removing NH_3 increases the accuracy of measurements downstream by eliminating possible cross sensitivities. After the reaction section, a condensation dryer removes phosphoric acid and water. Then, a Limas 11 HW unit measures NO and NO_2 concentrations. While NO_2 is detected via NDUV absorption, NO is detected via the differential resonant absorption UV spectroscopy technique (DUVRAS). Subsequently, a Magnos 206 analyzer relying on the paramagnetism of O_2 molecules detects O_2 . Finally, an Uras 26 photometer using non-dispersive infrared (NDIR) absorption measures CO , CO_2 , and N_2O .

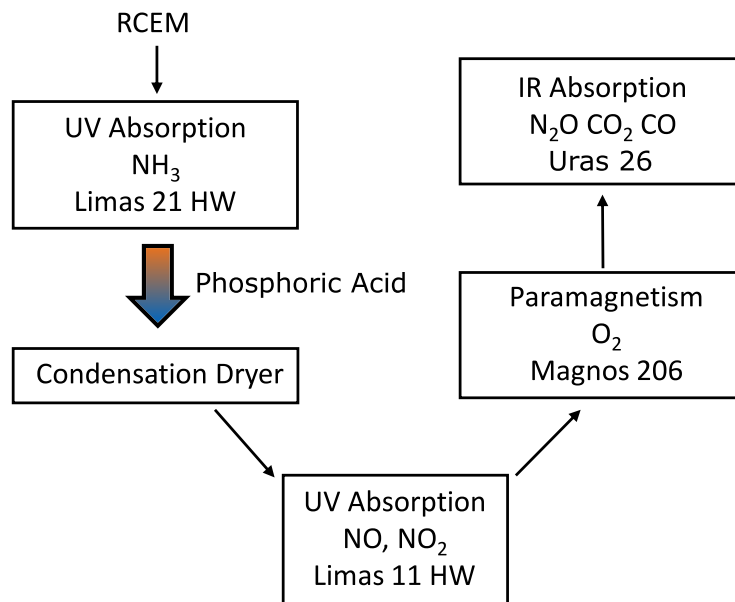


Figure 4.7: Scheme of the exhaust gas analysis system.

Emission measurement results from combustion devices, such as engines and gas turbines, are commonly normalized to ensure comparability between different operating conditions and devices. Frequently used methods are the cor-

rection of exhaust gas concentrations to a specified oxygen concentration (e.g. ppm at 15 % O₂) or the correction of pollutant mass to work performed (e.g. mg/kWh). However, in the RCEM, no work is extracted. In addition, ammonia has a different air demand per LHV than hydrocarbon fuels and hydrogen (see Table 3.1). As a result, when operated with different fuels, exhaust gas oxygen concentrations do not directly relate to a combustion device's power output. Therefore, this work quantifies pollutants formed during combustion in the RCEM via production rates r_p . The production rate of the species i (i.e. NO, NO₂, N₂O) is calculated via the equation:

$$r_{p,i} = \frac{M_i x_i N_{\text{ex}}}{H_{\text{inj}}}, \quad (4.3)$$

where M_i is the molar mass of the species i , x_i is its concentration in the dry exhaust gas, N_{ex} is the number of moles of dry exhaust gas in the RCEM assuming complete combustion, and H_{inj} is the total injected LHV including diesel and ammonia. The molecular weight of NO₂ is used to calculate the production rate of overall NO_x. As the air pollutants (except NH₃, see below) are measured in the dry exhaust gas, water removal in the condensation dryer is considered when calculating the number of moles of dry exhaust gas, N_{ex} , from the total moles of exhaust gas after combustion, $N_{\text{ex,wet}}$. The effect of this correction is small, as the RCEM operates with extremely lean mixtures for experiments where exhaust gases are analyzed. In contrast to engines and gas turbines, the amount of exhaust gas can be accurately determined, as the RCEM volume, initial pressure, and the injected amount of fuel per cycle are known.

Furthermore, the ammonia conversion rate results from comparing the ammonia concentration in the wet exhaust gas $x_{\text{NH}_3,\text{wet}}$ to the total number of injected moles of ammonia $N_{\text{NH}_3,\text{inj}}$ via the equation:

$$\eta_{\text{NH}_3} = \frac{N_{\text{NH}_3,\text{inj}} - x_{\text{NH}_3,\text{wet}} N_{\text{ex,wet}}}{N_{\text{NH}_3,\text{inj}}}. \quad (4.4)$$

As ammonia is analyzed before the condensation dryer, a correction for the water removed by condensation is not required. The reaction section and the condensation dryer only absorb small fractions of the NO and NO₂ emissions. This absorption was tested by supplying calibrated gas mixtures to the exhaust gas analysis after the system operated with exhaust gas in a steady state.

4.5 Controls and Data Acquisition

This section introduces the main features of the RCEM's control and data acquisition system. A National Instrument CompactRIO system featuring a field-programmable gate array (FPGA) enables the execution of calculations and control operations during the experiment. Furthermore, various available I/O cards allow for a wide range of control operations. In particular, two NI9751 cards drive the solenoid injectors with a tailored current profile.

Table 4.4 lists the recorded signals, including the corresponding sensor specifications and data acquisition details. The analog voltage signals of the chamber pressure sensor, the fuel supply pressure, and the chamber temperature are sampled every 10 μ s. The digital signal for the piston position is sampled at higher rates to capture the fast piston movement measured with the high resolution of the incremental encoder. Furthermore, camera shutter timings are fast (down to 1.25 μ s) and require higher sampling rates. The piston position signal is directly processed by the FPGA. As a result, the piston position is known at any time during the experiment.

Figure 4.8 depicts piston position and chamber pressure during an exemplary experiment in the RCEM. The compression stroke is followed by expansion after a dynamic equilibrium has been reached (see Section 4.1). As a result, the piston oscillates around the position of the static force equilibrium. The region of interest for the combustion consists only of the first compression stroke, during which the piston moves like the piston of a crankshaft-driven engine. Due to fast homogenization of the charge and globally extremely lean equivalence ratios, no reactions occur during the subsequent oscillations of the

Table 4.4: Overview of signals, sensors, and data acquisition specifications.

signal	sensor			acquisition		
	type	max.	accuracy	module	rate	resolution
chamber pressure	Kistler 6061 incl. 5018A	250 bar	< 0.05 bar	NI9215	10 μ s	10 V/16bit
chamber temperature	Thermocouple Type K	200 K	< 1 K	NI9201	10 μ s	10 V/12bitL
fuel supply pressure	ADZ Nagano SML600	600 bar	< 0.3 bar	NI9201	10 μ s	10 V/12bitL
piston position	incremental encoder	10 m/s	0.05 mm	NI9401	100 ns	5 V / TTL
camera I/O				NI9401	100 ns	5 V / TTL

piston, which recompress the charge (see Section 4.4).

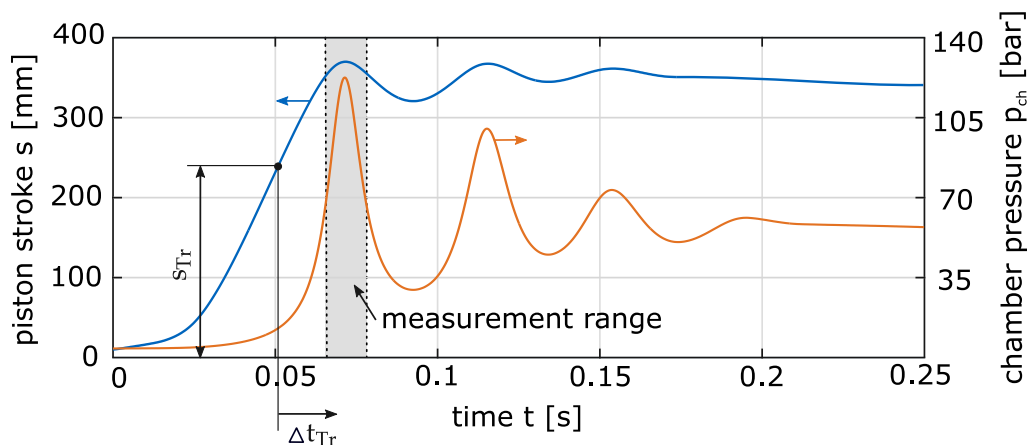


Figure 4.8: Exemplary piston position (blue) and combustion chamber pressure curves (orange) for an experiment in the RCEM. The figure indicates the measurement range and trigger criteria.

Fuel injection and the start of camera recording are triggered based on the piston position s_{Tr} and an additional time delay Δt_{Tr} (see Figure 4.8). This criterion is required, as the piston moves slowly and not consistently during the first parts of the stroke. The combined criterion allows triggering fuel injection and camera recordings reproducibly with respect to TDC. However, the correct time delays and piston positions must be determined for each

operating point. In engines, crank angle-based criteria trigger fuel injection. This procedure is impossible in the RCEM due to the lack of a crankshaft.

For simultaneous SG and OH* CL measurements, the OH* CL camera and the corresponding image intensifier synchronize with the SG camera via a master-slave circuit. While the SG camera only requires a short shutter time of $1.25 \mu\text{s}$, the image intensifier and OH* CL camera require exposure times of at least $20 \mu\text{s}$. The exposure times of the camera sensors are recorded via the control system to enable matching the OH* CL images to the corresponding SG images in the post-processing procedure.

4.6 Uncertainty

The repeatability of experimental conditions in the RCEM is shown to be high by low scatter in experimental results for undisturbed diesel pilot ignition (see Chapter 6 and [111]). Furthermore, the absence of significant charge motion and residual gases from previous cycles produce well-defined boundary conditions suitable for validating CFD simulations [120, 121]. Nonetheless, multiple sources cause uncertainties in the experimental conditions. This section discusses the most important uncertainties for the experiments conducted in this work and quantifies them, where possible.

Compression end temperature and pressure at TDC vary depending on the driving pressure, initial charge pressure and temperature, as well as friction effects due to oil temperature changes. The scatter in TDC pressure is measured directly. The variation in TDC temperature results from superimposing the initial temperature deviation ($296 \text{ K} \pm 2.5 \text{ K}$) and the deviation resulting from different TDC pressures when calculating the TDC temperature based on isentropic relations (see Equation 4.1). Table 4.1 includes the resulting uncertainties for the operating points investigated. Furthermore, the piston trajectory varies depending on the parameters mentioned above. This variation shifts the injection timing relative to TDC by up to $\pm 0.1 \text{ ms}$.

Visualization experiments show that the ammonia injection is delayed with respect to the results obtained from the IAV injection analyzer measurements.

However, as the double-pass Shadowgraphy setup cannot cover the near-field of the ammonia injector, an exact determination of the time delay is impossible. The delay is estimated to be $0.15 \text{ ms} \pm 0.05 \text{ ms}$ by comparing the start of injection predicted by the IAV injection analyzer results to the optically determined start of injection. This delay is in line with the 0.12 ms delay observed during previous investigations at the test rig using natural gas [115]. Therefore, the relative injection timings discussed in this work include a delay of 0.15 ms compared to the injection analyzer measurements. The uncertainty of this delay ($\pm 0.05 \text{ ms}$) translates as uncertainty in relative injection timing.

The injection rate profile measurements were conducted using hydraulic oil injections into the chamber of an AVL injection analyzer at a back-pressure of 50 bar . When using ammonia as fuel in the RCEM, the chamber back-pressures are higher than in the injection analyzer. While the higher back-pressure is accounted for by using relative pressures to determine the injection mass fluxes, the opening and closing behavior will also change with absolute pressure. Furthermore, an additional back-pressure in the fuel leakage line is required to keep ammonia liquid within the injector (see Section 4.2). This measure might also alter opening and closing behavior. In addition, the ammonia pump only allows setting the injection pressure with an accuracy of $\pm 10 \text{ bar}$. Moreover, the different cavitation behavior of ammonia compared to hydraulic oil affects the injected volume flux depending on the operating conditions, discussed in Section 4.2.

While the fuel mass flux in engines can be confirmed by weighing the fuel tank during a large number of cycles, the low repetition rate of experiments in the RCEM prohibits this approach. However, the exhaust gas analysis system can measure the ammonia exhaust gas concentrations after injections into the combustion chamber. The ammonia remains entirely unburned if no pilot fuel is injected. The experimental validation is conducted for two test cases with fuel injections centered around TDC. Table 4.5 shows the respective results. The mean values of injected mass fluxes deviate from the calculated values by approximately 6% and 4% , respectively. However, the measured injection masses are also subject to uncertainties, e.g. the amount of blow-by and leakage during the experiment.

Table 4.5: Calculated and measured injection masses for two injection cases at OP4.

specifications		calculated injection mass	measured injection mass	
nozzle	inj. pressure		mean	std. dev.
0.94 mm	530 bar	210 mg	221.3 mg	6.8 mg
0.98 mm	265 bar	125 mg	120.5 mg	0.94 mg

Piston ring blow-by decreases the air mass in the combustion chamber during the experiment. The main part of the blow-by occurs during the highest chamber pressures close to TDC. Therefore, the blow-by may consist mainly of charge air accumulated in the piston crevices, and the share of fuel in the blow-by might be low. Unfired experiments in OP4 investigate the blow-by. After the experiment, the piston is quickly moved into its starting position, and the pressure loss is measured. This procedure indicates a blow-by typically ranging from 3 % to 5 %. The blow-by impacts the production ratios and conversion rates determined by the exhaust gas analysis system (see Section 4.4). However, the blow-by is not corrected in the post-processing procedure, as its composition, i.e. its fraction of combustion products, is unknown.

5 Methods

This chapter introduces the post-processing methods used to extract the desired information from the experimental data. The first section presents the thermodynamic model that infers heat release rates from the pressure trace. Then, the image post-processing routines for the simultaneously acquired SG and OH* CL images are presented. Afterward, the following section describes the calibration procedure required for the spectroscopy measurements and the extraction of background corrected intensities. Finally, the 1-D spray model is introduced.

5.1 Thermodynamic Model

A multi-zone thermodynamic model calculates the HRR using cylinder pressure and piston position data. Figure 5.1 shows the modeled zones and their interactions. Standard engine-based models (e.g. for wall heat losses) are unsuitable for modeling the RCEM conditions owing to the cold walls and large crevice volumes. The central part of the compressed charge is assumed to consist of an isentropic core I, which undergoes isentropic compression and expansion, as proposed by Lee and Hochgreb [112] for a rapid compression machine (see Section 4.1). Heat losses are calculated based on the model presented in Fink et al. [70]. Heat transfer to the isothermal walls occurs only in the crevices C, which exchange mass with a gap G. In contrast, the isentropic core I does not exchange any mass with the adjacent gap G. The temperature profile along the crevices is modeled by dividing the crevice zone into 8 logarithmically sized crevice elements. The heat loss model is fitted to match the heat loss of the RCEM during unfired experiments at the investigated OPs by adapting the surface area of the crevices.

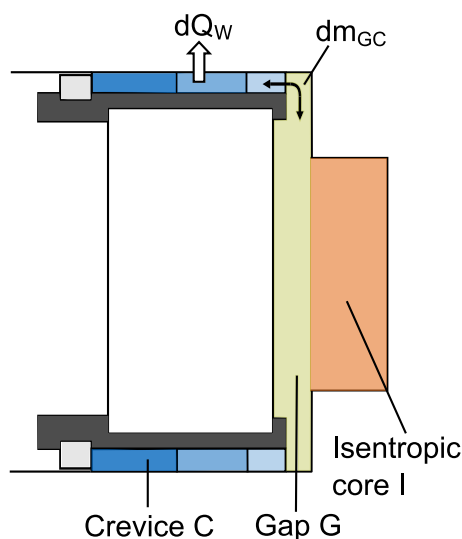


Figure 5.1: Scheme of the thermodynamic model of the combustion chamber indicating the different zones, mass transfer, and heat loss.

The cooling effect of fuel evaporation cannot be considered adequately, as its exact timing is unknown. The same issue applies to the effect of species conversion, as it is unknown which fuel burns at any point in time. Therefore, the model used neglects fuel injection and species conversion effects entirely. This approach is common for calculating apparent HRRs in direct injection engines, as heat release by combustion is larger than evaporation and species conversion effects. However, the neglected effects are more significant for ammonia engines than diesel engines, as the heat of vaporization and the injected number of moles are larger for ammonia. The interaction of hot combustion products with the RCEM walls will lead to heat losses, which are not considered by the fitting to unfired experiments. However, the neglected losses are similar among the conducted experiments, and direct comparisons of the HRRs are valid.

The first law of thermodynamics is used to solve the model for the apparent HRR in the isentropic core, which originates from combustion, fuel injection, evaporation, and species conversion. Figure 5.2 shows an exemplary HRR curve and injection profiles obtained in an experiment at OP4 with converging jets and slightly advanced diesel injection. Pilot ignition is assumed to occur when the HRR exceeds 0.14 MW compared to the HRR at the start

of pilot injection. This relative criterion is necessary, as the apparent HRR drops during the evaporation of ammonia for late diesel injections. A total threshold value of 0.45 MW represents the main ignition of ammonia. This value exceeds the maximum HRR observed for cases with diesel combustion only. The following ignition delay parameters are derived:

- Δt_p : The diesel ignition delay Δt_p is defined as the time between pilot ignition and pilot start of injection.
- Δt_m : The main ignition delay Δt_m is calculated from the time between the first ammonia injection and the detected main ignition.
- Δt_{mp} : The relative ignition delay Δt_{mp} is obtained from the time between pilot and main ignition.

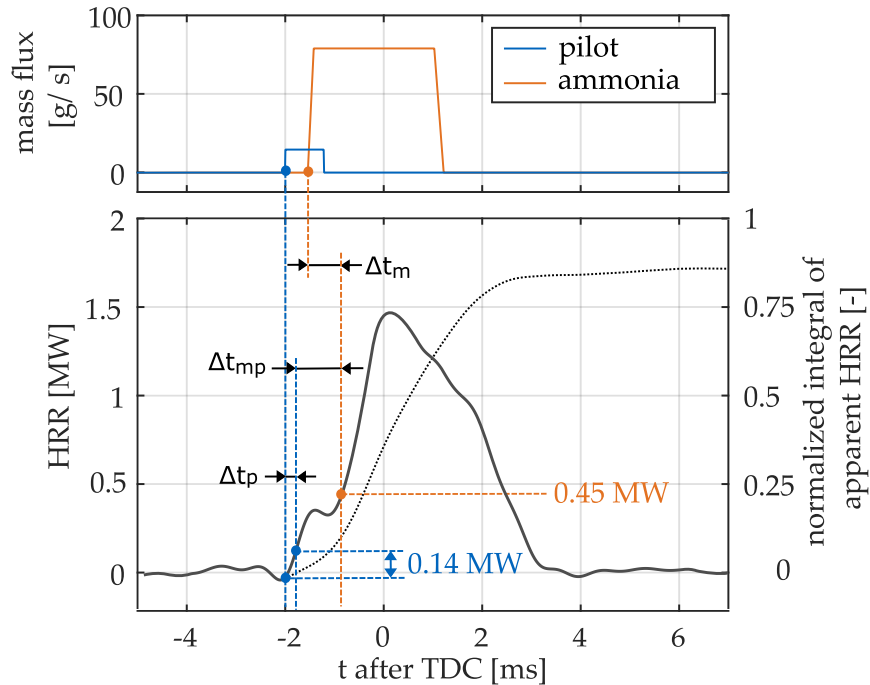


Figure 5.2: Determination of key figures from the HRR and injected mass fluxes.

Misfiring is assumed if the HRR does not exceed the threshold value for the main ignition during combustion. Furthermore, the relative burnout rate of the injected fuels is calculated by integrating the apparent HRR, normalizing

it with the injected LHV of both fuels and subsequently normalizing it with the highest value in the discussed data set. While this does not give an absolute value for the percentage of fuel burnt, it permits a comparison of the presented cases. This method is used for parameter studies where the large amount of ammonia burned causes condensation after the experiment, and the exhaust gas analysis cannot be applied. However, the larger amount of fuel injected increases the quality of the HRRs obtained, which is crucial for determining the ignition delays.

5.2 Image Processing

The optical data obtained requires post-processing to extract the relevant quantities. Therefore, this section introduces the image post-processing routines used. The first subsection presents the routines for extracting gaseous penetration, liquid penetration and spray angles from SG and MS images. Then, the processing routine for simultaneously acquired SG and OH* CL images is presented. The final subsection introduces the calibration procedure for the spectroscopy data and the background correction method.

5.2.1 Shadowgraphy and Mie-Scattering

Gaseous penetration, liquid penetration, and the spray angle are vital parameters to describe sprays. In this work, they are either used as model input (spray angle, see Section 5.3) or for model validation (gaseous and liquid penetration, see Section 8.1). Both imaging techniques are obtained with the same camera and share the same calibration procedure. The setup is described in Section 4.3. However, SG images require the Xenon arc lamp for illumination, while MS imaging requires a laser sheet. Figure 5.3 describes the procedure for extracting gaseous and liquid spray penetration.

First, the scale is extracted from known features of the RCEM combustion chamber, i.e. the reduction ring diameter of 115 mm. The scale typically ranges from 5 px/mm to 5.5 px/mm. Subsequently, the location of the ammonia in-

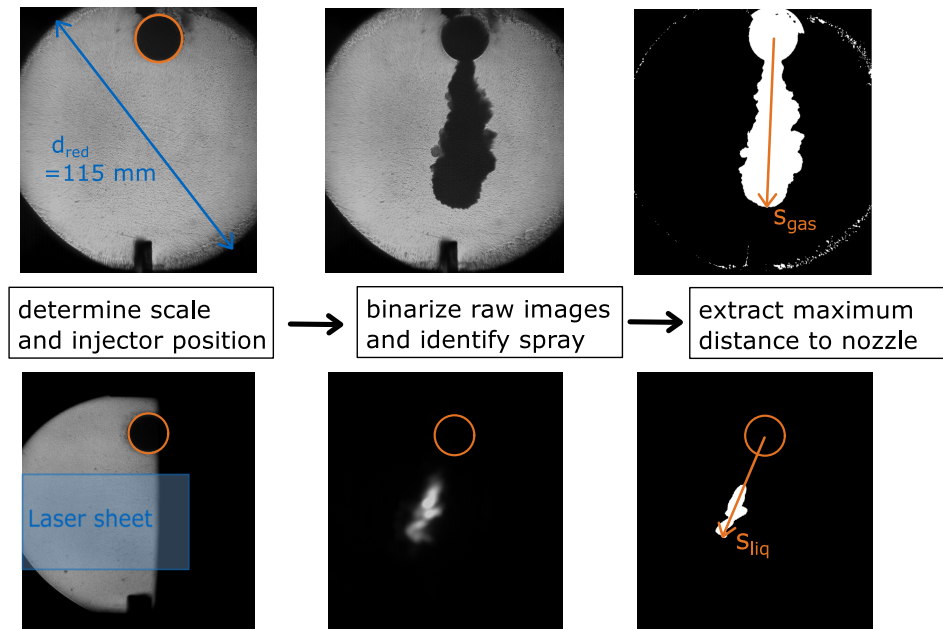


Figure 5.3: Procedure for determining gaseous and liquid spray penetration from SG (top) and MS (bottom) images.

jector is detected. A circular Hough transform detects the ammonia injector reliably, as the injector appears as a dark circular shadow in the SG images. Afterward, the images are binarized, to obtain the spray area. The brightness threshold for binarization results from the average brightness of the images before spray injection. The spray area is the largest area in the combustion chamber not adjacent to the image border, which exceeds (MS) or is less than (SG) the brightness threshold. The spray penetration is the largest distance from the injection hole to a pixel belonging to this spray area. As injector position and combustion chamber dimensions cannot be extracted from MS images, SG images are recorded before the MS experiments for calibration.

The spray angle results from comparing the spray area up to 90% of the maximum gaseous penetration to a triangle with the same height and origin. The angle of this triangle that leads to the same area as the spray is the spray angle. This approach is similar to investigations in the literature [8, 105, 122]. However, the distance from the nozzle exit, at which the area is compared, differs. For example, 50% of spray penetration [8], 1.2 times the liquid length [105] and 60 times the nozzle diameter [122], have been used.

This work chooses a length of 90 % due to the lack of a distinct head vortex in the investigated sprays. This approach maximizes the area considered for spray angle estimation, and turbulent effects on the spray edges have the smallest effect possible.

5.2.2 Simultaneous SG and OH* CL

Superimposing the simultaneously acquired SG and OH* CL images allows allocating the OH* CL emissions to the spray structure. However, the resolution and orientation of SG and OH* images do not match exactly, which requires an image matching procedure. While the combustion chamber features (injector, reduction rings) are visible in the SG images, they cannot be identified in single CL frames. Therefore, the image matching procedure averages 50 OH* images taken before fuel injection, which renders the injector and reduction rings visible. An optimizer in the *Matlab Image Processing Toolbox* searches for the best match between the two images by rotating, scaling, and cropping the averaged OH* CL image. Then, all OH* CL images taken during this experiment are transformed according to the best match.

Figure 5.4 shows two procedures for superimposing SG and OH* CL images. The first procedure (Figure 5.4, top) allocates the intensities of the SG and CL images to a 2-D colormap to compose the superimposed image. Therefore, one image depicts the information contained in both images without any loss of information. As a result, brighter areas in the SG images remain distinct, e.g. the spray tip in the SG images shown in Figure 5.4. This work mainly uses this procedure to condense information comprehensively. However, Section 7 relies on only projecting the SG contour onto the OH* CL images (Figure 5.4, bottom), as this procedure facilitates the undisturbed comparison of OH* CL and natural flame luminosity.

The OH* CL intensity emitted by the ammonia spray flame is lower than the intensity of the pilot flame (see Section 7). The strong CL of the pilot combustion limits the gain and exposure time used for capturing the CL images. As a result, OH* CL intensity is weak during ammonia combustion. The CL intensities are brightness-corrected by potentiating the initial intensity values

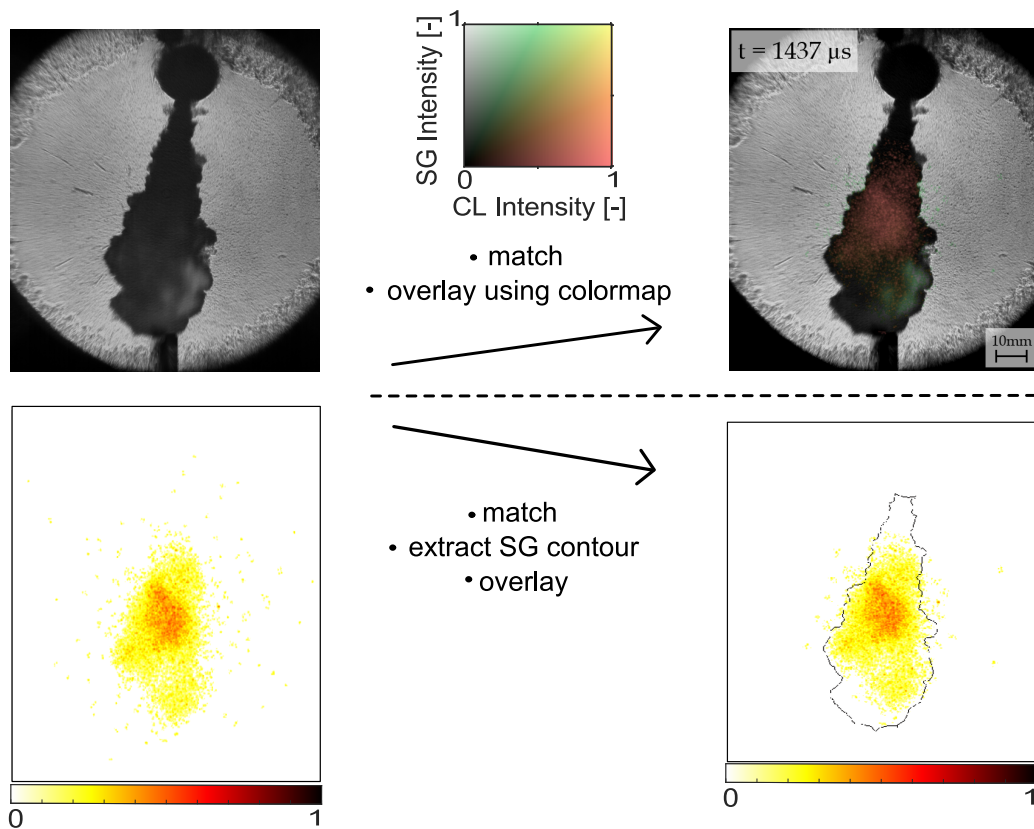


Figure 5.4: Procedures for superimposing SG and OH* CL images. Top: Transferring the entire information of both images using a 2-D color map. Bottom: Transferring the SG spray contour onto the OH* CL images.

ranging from 0 to 1 with values ranging from 0.3 to 0.5 to render the weak OH* CL during late ammonia combustion visible. This correction increases the brightness of regions with weak CL radiation.

The distance from the injector nozzle to the reaction zone determines the lift-off length. The largest contiguous area of CL intensity is assumed to represent the reaction zone. Therefore, small areas of CL intensity resulting from background noise are not considered for determining the lift-off length. This step is necessary, as background noise is high due to the weak OH* CL intensity during ammonia combustion.

5.2.3 Spectroscopy

The monochromator preserves the spatial coordinate along the spray axis (vertical), while the incident light disperses on the coordinate perpendicular to the spray axis (horizontal) depending on its wavelength. Therefore, the horizontal position of the pixels of the images taken reflects specific wavelengths, while the vertical position of the pixels corresponds to a certain height in the combustion chamber. Before the combustion experiments, light emitted by a mercury-arc lamp is recorded. This light consists of several distinct spectral lines specific to mercury-arc lamps. Therefore, specific pixels of the images taken correspond to certain wavelengths, and a conversion rule from the pixel to the wavelength scale is derived based on interpolation. Figure 5.5 shows the spectroscopic image of the light emitted by the mercury arc-lamp (Figure 5.5, top left) and the corresponding intensity distribution along the horizontal pixel coordinate (Figure 5.5, bottom left). In addition, the conversion rule from the pixel to the wavelength scale is shown (Figure 5.5, right). Furthermore, the coordinate along the spray axis is calibrated by varying the position of the mercury-arc lamp within the combustion chamber. For this purpose, the cylinder head is dismantled so that the position of the lamp can be freely adjusted within the combustion chamber.

In addition, a third calibration procedure corrects the wavelength-dependent sensitivity of the setup employed. This calibration requires a light source with a continuous emission spectrum. Therefore, a halogen lamp, whose continuous spectrum is known from the manufacturer, was located centrally in the combustion chamber, and the light emitted was recorded. A wavelength-dependent calibration function was derived by comparing the intensities obtained by the spectroscopy setup to the reference spectrum. This function corrects the spectra obtained during the experiments. The correction considers the wavelength-dependent sensitivity of the entire setup, encompassing the quartz-glass pistons and lens transmissivities, as well as the monochromator's and the image intensifier's sensitivities. Figure 5.6 shows the reference spectrum, the measured spectrum, and the calibration factors for the setup used.

While this work often uses raw spectra obtained with the monochromator

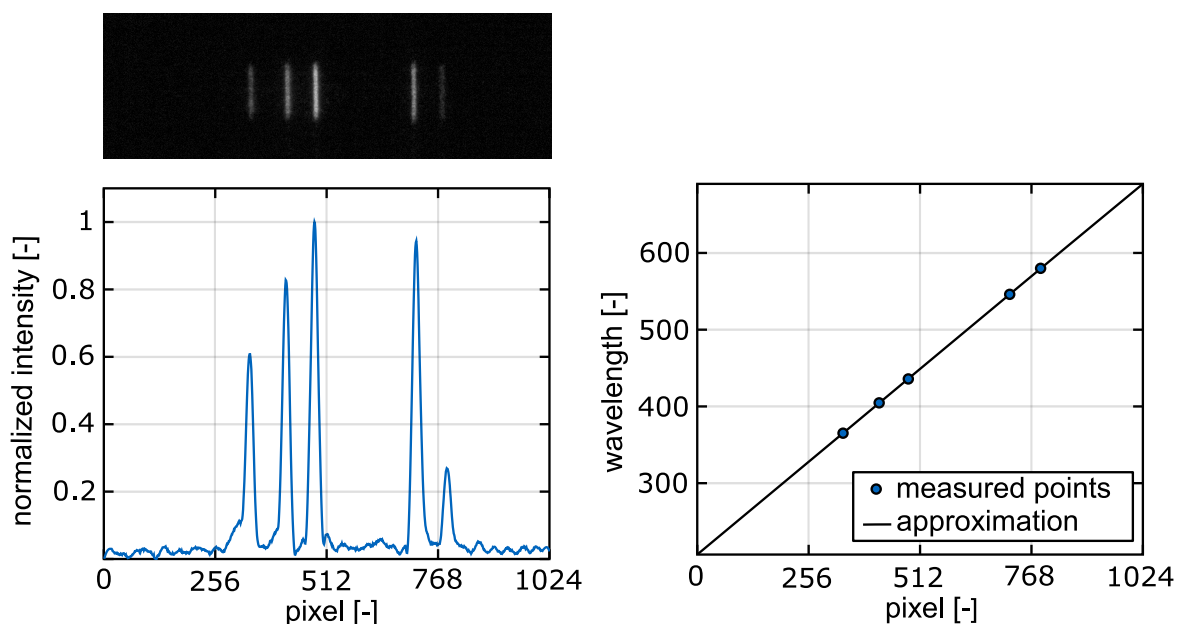


Figure 5.5: Spectroscopy raw image of the light emitted by the mercury arc lamp obtained with grating 3 (top left), corresponding intensity plotted over the pixel scale of the light emitted by the mercury arc lamp (bottom left), and conversion rule from the pixel scale to the wavelength scale for the setup used (right).

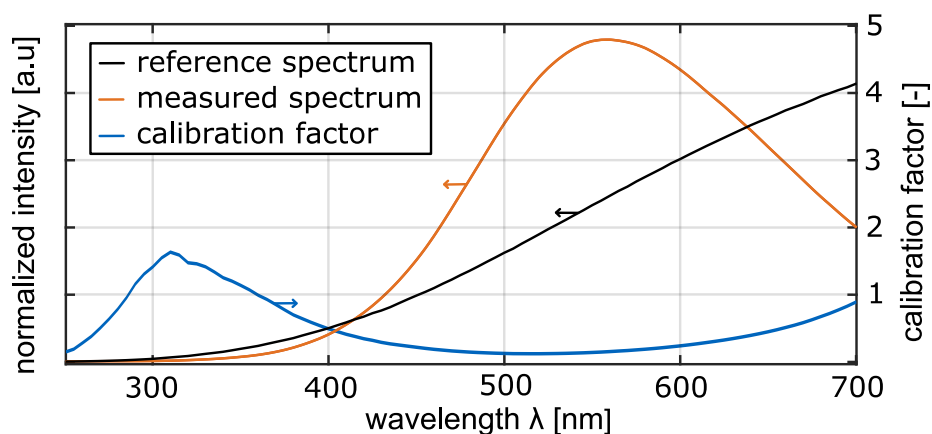


Figure 5.6: Reference spectrum of a calibrated halogen lamp, measured spectrum, and calibration factor of the setup employed.

to discuss the evolution of the dual-fuel combustion process, the results also discuss the background corrected intensities of OH^* , NH^* , NH_2^* , and broadband emissions. The background corrected intensities result from integrating

peak areas corresponding to the respective species' CL emissions. These peak areas superimpose on a continuous background of broadband flame emissions. Figure 5.7 illustrates the areas considered for the background corrected OH^* , NH^* , and NH_2^* intensities. The background radiation is interpolated linearly within the range, in which each considered species causes a peak in CL emissions to distinguish between species-specific and background radiation. The spectra were filtered using a Savitzky-Golay filter in *Matlab* to reduce noise and enable reproducible interpolation of the background radiation. The filter considered 21 interpolation points to approximate fifth-degree polynomials. In addition, broadband luminosity intensity is considered, which is obtained by integrating the intensities over the entire range of investigated wavelengths.

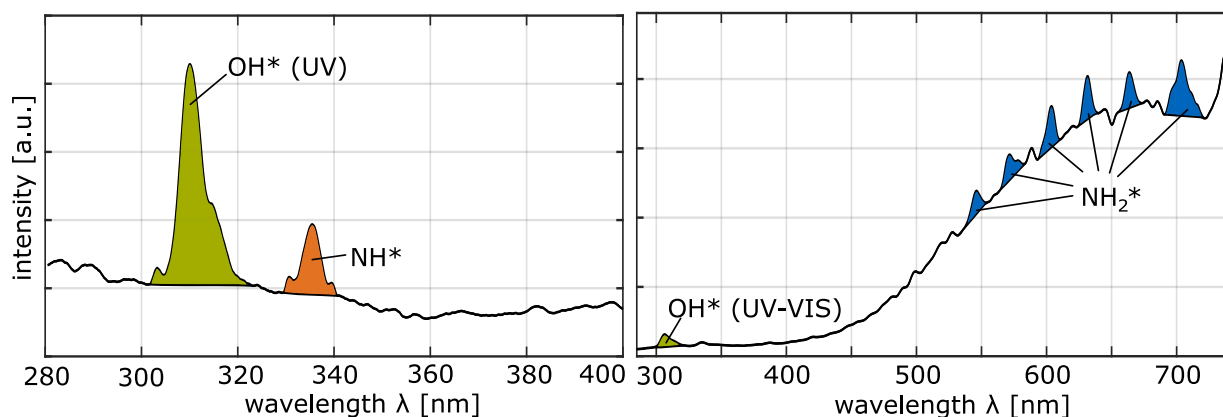


Figure 5.7: Typical CL spectrum of ammonia combustion. Left: UV range obtained using grating 2, right: UV-VIS range obtained using grating 3. The colored peak areas represent the background corrected CL intensity of the corresponding species.

While OH^* and NH^* intensities are obtained by considering the area of individual peaks, the NH_2^* intensity is obtained by adding the intensity of several of its major peaks. NH_2^* flame emissions consist of a multiple-line system appearing as a continuous band with superimposed spikes [13, 123]. Therefore, the approach followed in this work only detects a fraction of the actual NH_2^* intensity. However, the intensity inferred from the peak areas can give information on when NH_2^* radiation occurs and its relative intensity. OH^* intensities were derived from images obtained using both gratings. NH^* intensities are derived using the higher spectral dispersion (grating 2), as the NH^* peak was

not sufficiently prominent for the post-processing routine in the images obtained using the lower spectral dispersion offered by grating 3 (see Section 4.3.4). The broadband radiation can mainly be assigned to CO_2^* at shorter wavelengths and at longer wavelengths to NO_2^* , H_2O^* , and NH_2^* [13]. For diesel combustion, soot might occur additionally.

5.3 Spray Model

To gain insights into equivalence ratios, temperatures, and physical states within the investigated ammonia spray, the Musculus and Kattke 1-D control volume model is used [16, 52]. The model is adapted to ammonia as the fuel and to the conditions in the RCEM employed. This section outlines the model's main features and presents the necessary adaptations to ammonia and the specific experimental environment in the RCEM. Musculus et al. [16] provide more detailed explanations of the underlying model and necessary assumptions.

The 1-D transient model features equally spaced fixed control volumes. The volumes result from the spray angle, which remains constant during injection and is supplied as model input (see Section 8.1). Mass and momentum conservation equations are solved for each control volume to obtain the entrained air mass for each time step. Figure 5.8 shows a schematic of the control volumes. The radial mixture fraction distribution is obtained by assuming an evolution from top-hat-shaped profiles at the nozzle exit to fully developed shapes. As suggested in [124], the shape of the fully developed radial profiles for the mixture fraction follows the expression:

$$\frac{\bar{X}_f}{\bar{X}_{f,c}} = (1 - \xi^{\alpha_p})^2, \quad (5.1)$$

where \bar{X}_f is the turbulent mean fuel volume fraction at the non-dimensional radial distance $\xi = r/R$, $\bar{X}_{f,c}$ is the turbulent mean fuel volume fraction at

the center line and α_p varies from $\alpha_p = \infty$ at the nozzle exit to $\alpha_p = 1.5$ for a fully developed jet profile. In the transition region between the nozzle exit and the fully developed jet, α_p is chosen so that the center line velocity does not exceed the initial velocity at the nozzle exit. Center-line and cross-sectionally averaged values are obtained analytically. The fuel volume fraction on the center-line $\bar{X}_{f,c,l}$ determines the maximum liquid length at which fuel vaporization is complete. Siebers et al. [105] present the calculation of this fuel volume fraction in more detail. This work uses NIST database chemical properties of ammonia and air to determine the respective thermodynamic states [18]. In addition, the model yields the gaseous penetration.

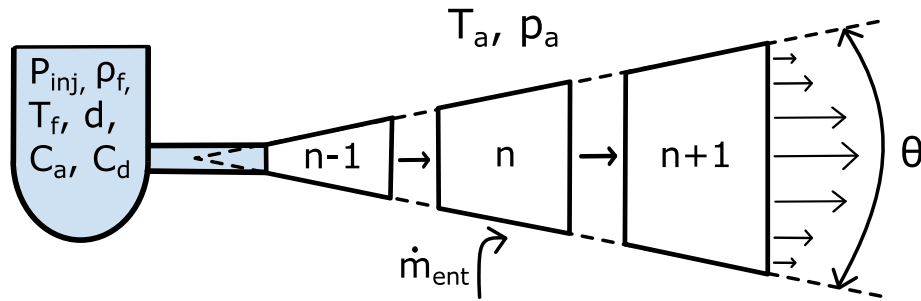


Figure 5.8: Schematic of the 1-D model. Adapted from [16].

Environmental conditions within the RCEM are transient. However, the Musculus and Kattke model assumes constant boundary conditions. Therefore, average air temperature and density values during the first 2ms of ammonia injection serve as model inputs. Fuel evaporation and combustion only impact in-cylinder conditions slightly because global equivalence ratios within the RCEM are extremely low. In addition, the slow piston movement (~ 1000 rpm) and the fact that ammonia injects close to TDC lead to small changes in in-cylinder conditions during the injection. Figure 5.9 shows injection velocities and in-cylinder density for the experiments in OP4. The in-cylinder density varies between 43.6 kg/m^3 and 45.4 kg/m^3 during the first 2ms of injection, which is within a deviation of $\sim 2\%$ from the mean density during this period of 44.5 kg/m^3 . In addition, the flat piston and large crevices avoid generating charge motion [112]. Therefore, transient effects are

negligible.

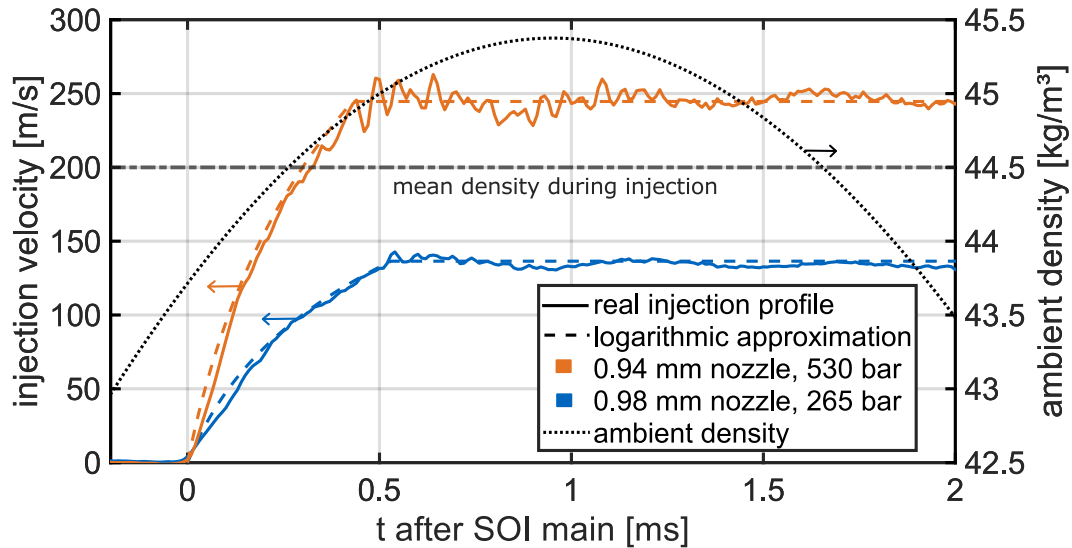


Figure 5.9: Approximated injection velocity profiles vs. injection velocity profile from experimental volume flux measurements for the three nozzles investigated at OP4.

Table 5.1 lists the model input parameters. A literature value of $C_a = 0.81$ is used, as no momentum flow rate measurements could be made [8]. The model relies on logarithmic injection velocity ramp-ups over time that approximate the actual shape of the injector behavior reasonably well (see Figure 5.9). Validation experiments with two different injectors show that the model validity is independent of the injector and nozzle employed. Chapter 8 presents the model validation.

Table 5.1: 1-D spray model input parameters.

average ambient temperature during injection T_a [K]	915
average ambient density during injection ρ_a [kg/m ³]	44.5
fuel density at 265 bar ρ_f [kg/m ³]	630
fuel density at 530 bar ρ_f [kg/m ³]	647
fuel temperature T_f [K]	293
<u>0.94 mm Nozzle</u>	
spray angle Θ [°]	24
absolute injection pressure P_{inj} [bar]	530
nozzle diameter d [mm]	0.94
area contraction coefficient C_a [–]	0.81
discharge coefficient C_d [–]	0.55
<u>0.98 mm Nozzle</u>	
spray angle Θ [°]	25.5
absolute injection pressure P_{inj} [bar]	265
nozzle diameter d [m]	0.98
area contraction coefficient C_a [–]	0.81
discharge coefficient C_d [–]	0.51

6 Ignition and Pilot Interaction Requirements

First, experimental proof showing the feasibility of the HPDF combustion process using ammonia as the main fuel is required. Therefore, the following chapter conducts extensive parameter studies to determine suitable conditions for the HPDF combustion of ammonia. For this purpose, HRRs are analyzed from experiments without optical access using an aluminum piston. This approach enables swift parameter variations over a wide range of operating conditions. First, a variation of diesel and ammonia's temporal and spatial interaction for two pilot sizes at OP4 determines suitable geometric arrangements and relative injection timings. Subsequently, charge conditions are varied from low to full-load conditions. The final section investigates pilot amount and injection duration effects using two different diesel nozzles. In this chapter, the 0.94 mm ammonia nozzle is used with a relative injection pressure of 405 bar (i.e. 530 bar at OP4, see Table 4.2).

6.1 Geometrical Arrangement and Injection Timing

The experiments presented in this section vary the interaction angle α and relative injection timing for two different pilot amounts of 10 mg and 5 mg (see Table 4.3). The range of timings and angles investigated in this work is small compared to similar investigations on methane/diesel HPDF combustion (see [111]), as the minimum necessary interaction between the fuel sprays for ammonia ignition is higher than for methane. Therefore, the investigated relative injection timings range from $-1000 \mu\text{s}$ (ammonia first) to $+1500 \mu\text{s}$ (diesel first), and the interaction angles range from $\alpha = -22.5^\circ$ (converging) to $\alpha = 15^\circ$ (diverging). The data set consists of 149 experi-

ments, including at least two repetitions for each case that showed successful ignition. Although the total number of repetitions for each data point is low, significant trends and the effects of spray interaction on the combustion of ammonia emerge clearly. The black dots contained in the figures of this section mark tested combinations. White areas indicate cases in which ignition failed at least once. Such cases are henceforth termed as misfiring. The operating conditions investigated in this section correspond to OP4 (125 bar, 920 K).

Figure 6.1 shows the relative burnout rate of the cases investigated. The relative burnout rates are normalized with the data point indicated by the star, which showed the highest absolute burnout rate. This data point was obtained with a 10 mg pilot, $\alpha = -7.5^\circ$ and a relative injection timing of $+500 \mu\text{s}$. Misfiring occurs for insufficient interaction of the two fuel sprays or when diesel strongly interacts with ammonia before ignition. Insufficient interaction occurs for positive relative injection timings, i.e. relatively earlier diesel injections, combined with diverging or strongly converging (-22.5°) spray configurations. For negative relative injection timings (ammonia first) and negative, converging interaction angles, ammonia strongly influences the diesel spray and inhibits its ignition. While the 10 mg diesel pilot ignites the ammonia spray at an interaction angle of $\alpha = -7.5^\circ$ consistently, the region of misfiring is wider for the smaller 5 mg pilot. While some strongly delayed ignitions were observed in this area for the 5 mg pilot, complete quenching also occurred. This quenching results from the strong interaction between diesel and ammonia. The interaction leads to lower air entrainment into the diesel spray. Instead, ammonia is entrained, cooling the mixture due to its lower temperature, high enthalpy of evaporation, and heat capacity. In addition to this physical effect, ammonia increases the ignition delay times of n-heptane kinetically [97].

Previous studies on methane/diesel HPDF combustion [70, 111] showed no misfiring at full-load charge conditions (OP4). The observations made with methane at low-load conditions (OP1) were similar to the observations made with ammonia for OP4 in this work. However, even at low-load conditions, ignition of the natural gas jet was still possible for a broader range of interaction angles and relative injection timings than for ammonia, despite smaller

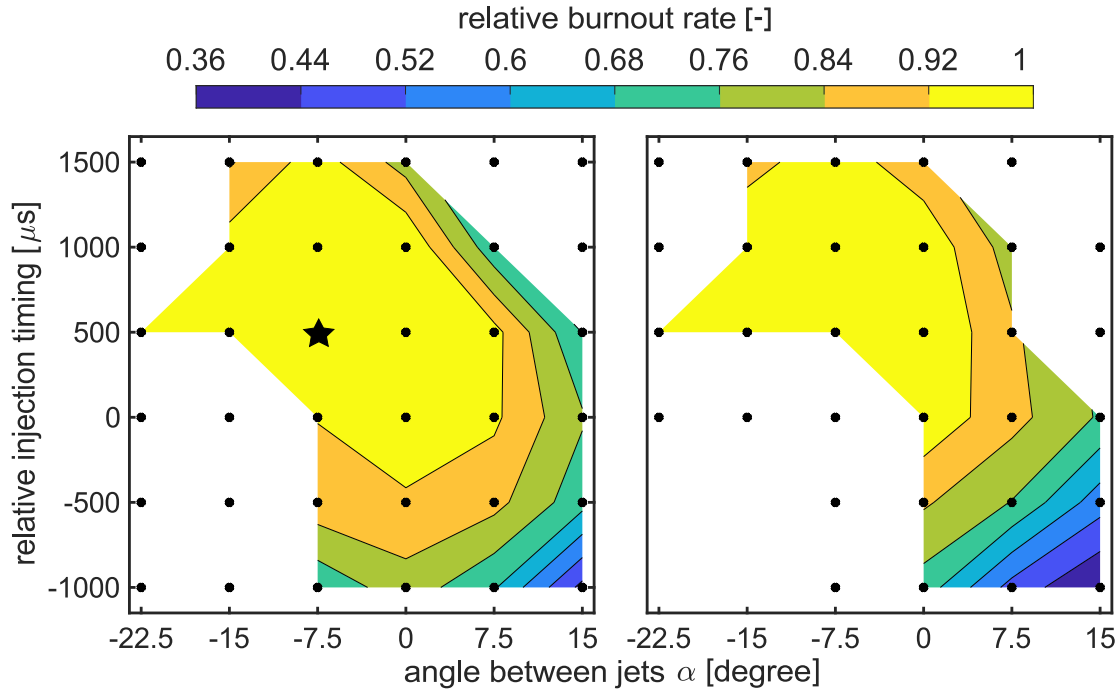


Figure 6.1: Relative burnout rate for different interaction angles α and relative injection timings for 10 mg (left) and 5 mg (right) diesel pilots.

diesel pilots. The small range of interaction cases in which ammonia ignition occurs suggests that a larger minimum amount of energy must be delivered to ammonia sprays than to methane jets to initiate the main ignition.

The relative burnout rate is high for parallel or converging sprays and moderately advanced diesel injections. These conditions permit undisturbed diesel pilot ignition followed by strong interaction with the ammonia spray. While the relative burnout rate for the 5 mg pilots is lower than for the 10 mg pilots with negative relative injection timings, it is similarly high for positive relative injection timings. For the investigated conditions, the effect of altering the spatial and temporal interaction of the two sprays is far larger than that of increasing pilot amount (compare left and right subfigures of Figure 6.1). The relative burnout rate for strongly advanced pilot injections is even slightly higher for smaller pilots. This higher burnout rate might be explained by a slower penetration of the diesel pilot, as the injector needle does not fully

open due to the low injection duration of the 5 mg pilot injection.

Figure 6.2 shows pilot (top), main (middle), and relative (bottom) ignition delays for the same parameter space (see Section 5.1 for the ignition delay’s definition). Pilot ignition delays are similar for advanced diesel injections and diverging sprays, as undisturbed pilot ignition is possible. Ammonia deteriorates diesel ignition for parallel or converging sprays combined with a negative relative injection timing (ammonia first). Therefore, pilot ignition delay increases until ignition is completely inhibited for very strong interaction and misfiring occurs. Particularly high pilot ignition delays occur for simultaneous injection of both fuels. The tip region of gaseous jets and liquid fuel sprays consists of a leading vortex, in which less air is entrained [125, 126]. The interaction of diesel with the fuel-rich ammonia head vortex increases the inhibiting effect of ammonia on diesel ignition. Similar behavior of the pilot ignition delay has been observed at low-load conditions (OP1) for methane/diesel HPDF combustion [111].

Due to strong spatial spray interaction, main ignition delays are short for converging sprays and advanced diesel injections. A strong correlation between main ignition delay and relative burnout rate (Figure 6.1) shows that early ammonia ignition is necessary to achieve high burnout rates for the conditions investigated. Quenching of the ammonia spray flame on the cylinder wall might limit the burnout rates if ignition does not occur early enough. The quenching might be weaker for real engines, as the walls are not as cold as the RCEM’s walls. In addition, neighboring sprays may prevent lean-out of ammonia sprays by decreasing air entrainment into the sprays. Instead, hot combustion products of neighboring sprays may entrain, leading to an increased reactivity. Furthermore, increasing the pilot fuel amount decreases the main ignition delay.

Relative ignition delays are generally shorter for stronger spray interaction. As expected, the relative ignition delay increases approximately with the difference in time between the two injections for positive relative injection timings (diesel first). The relative ignition delay mainly depends on the interaction angle α and not the relative injection timing for negative relative injection timings. Therefore, the ignition process of diesel and the subsequent transi-

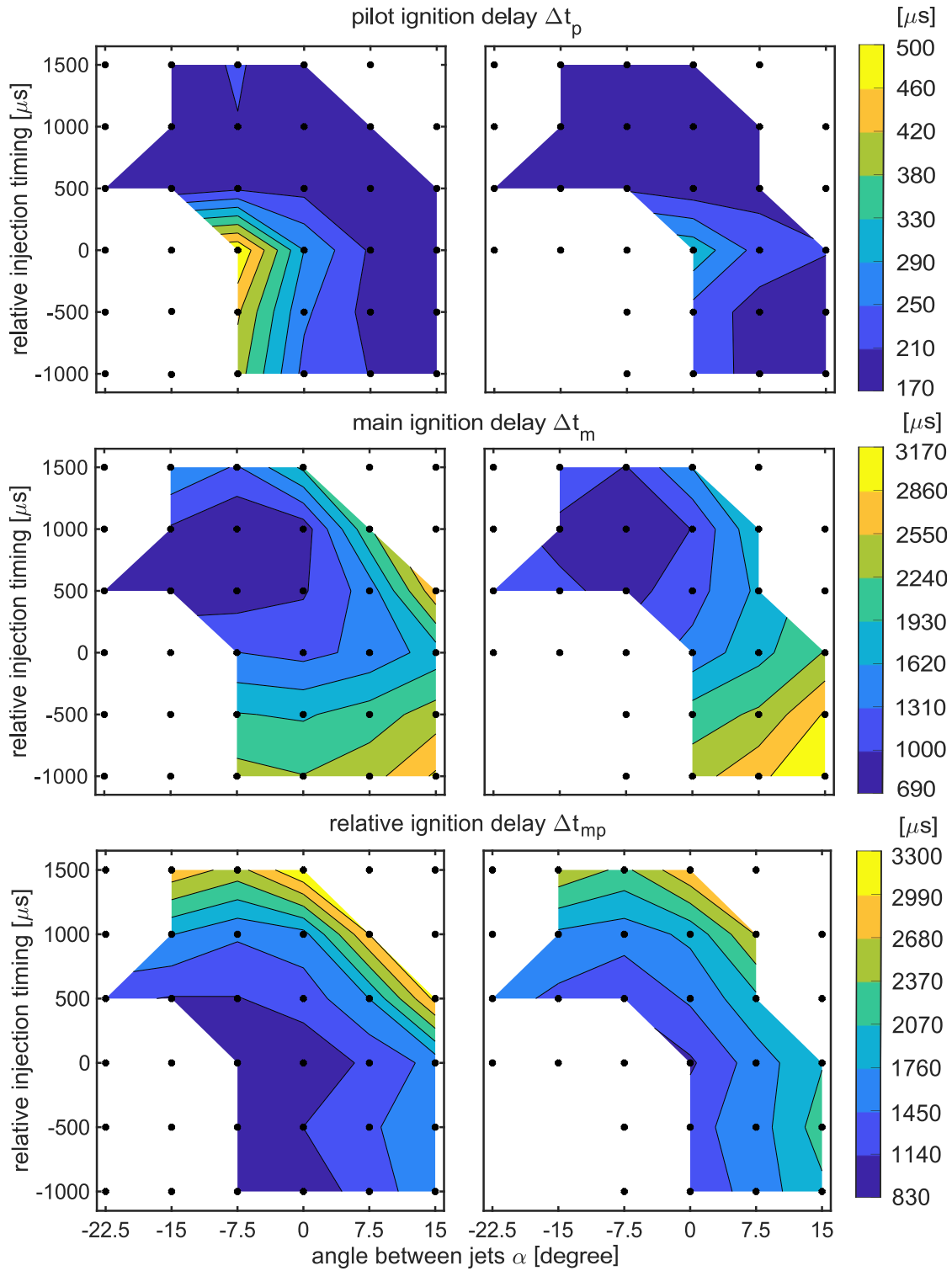


Figure 6.2: Pilot, main, and relative ignition delay for different interaction angles α and relative injection timings for 10 mg (left) and 5 mg (right) diesel pilot injections.

tion to ammonia combustion is only mildly affected by a change in the relative injection timing. However, the relative burnout rate (see Figure 6.1) decreases with decreasing relative injection timings. These two trends suggest that a significant part of the unburned ammonia for earlier ammonia injections results from the region downstream of the ignition location. The flame cannot cover the entire spray region before the earlier injected fuel becomes too lean to burn or interacts with the cold walls.

6.2 Charge Conditions

The investigations in this section fix the parameters varied in Section 6.1 to isolate the influence of charge conditions: The configuration with an interaction angle of $\alpha = -7.5^\circ$, and a slightly advanced 10 mg diesel pilot ($+500 \mu\text{s}$) injection is used. This configuration yields the highest burnout rates observed and is marked by a star in Figure 6.1. Further advanced diesel pilots show similar burnout rates. However, due to thermodynamic considerations, strongly advanced diesel injections might not be desirable when operating a full-scale engine. The experiments are repeated three times each. Instead of discussing key figures, such as ignition delays, the focus shifts to discussing the HRRs directly, as different operating conditions influence the key figures, e.g. by a higher degree of premixing of the diesel pilot at less reactive conditions that causes HRRs to exceed the main ignition threshold. Figure 6.3 presents the apparent HRRs relative to the start of injection (SOI) of ammonia for OP1, OP2, OP3, and OP4.

While ammonia successfully ignites for OP2 - OP4, its ignition fails for OP1. Although diesel injection starts before ammonia injection, the evaporating ammonia spray inhibits diesel ignition completely for OP1. In this case, the ammonia spray might outrun the diesel pilot during the longer pilot ignition delay and deteriorate pilot ignition. Ignition of the pilot injection causes the first peaks of the HRRs of OP2 - OP4. This first peak shifts backward at less reactive charge conditions due to longer ignition delays. The combustion of ammonia mainly causes the second, more prominent peak. While the pilot peak HRRs slightly increase for less reactive charge conditions due to increased

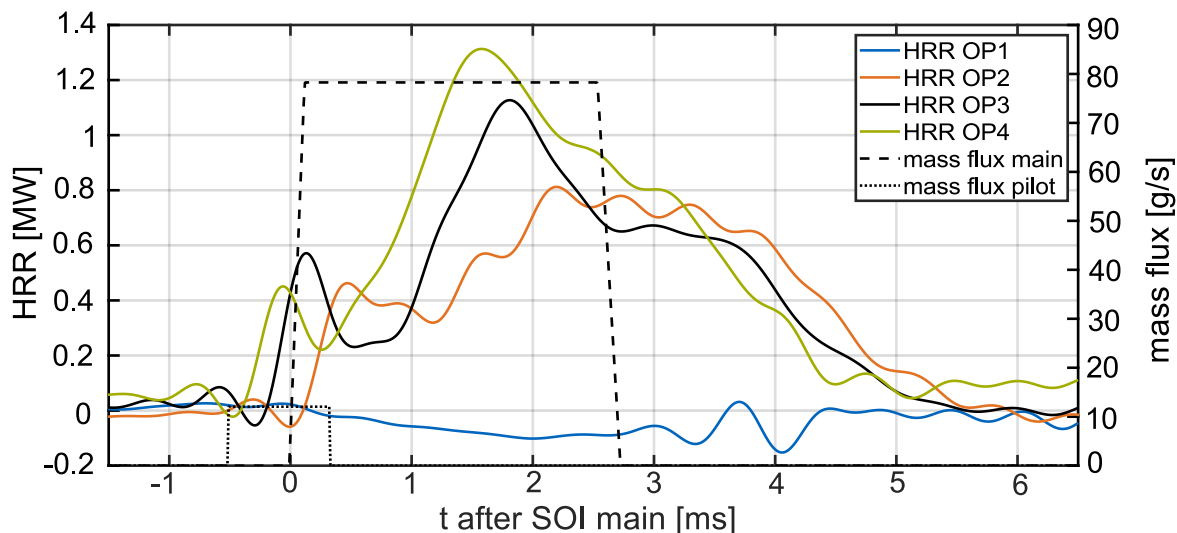


Figure 6.3: Fuel mass flux and averaged apparent HRRs for different operating points with slightly advanced ($+500 \mu\text{s}$) 10 mg diesel injections and converging sprays ($\alpha = -7.5^\circ$).

premixing, the main peaks of the HRRs decrease. In addition, the main combustion shifts more backward than what is to be expected only from longer pilot ignition delays. The observed behavior suggests strong deterioration of ammonia HPDF combustion at part-load conditions.

6.3 Pilot Characteristics

Figure 6.4 shows HRRs and corresponding diesel injection mass fluxes resulting from experiments with different piloting strategies (see Table 4.3). The HRRs shown are based on three repetitions each and obtained at OP4 with $\alpha = -7.5^\circ$ and slightly advanced $+500 \mu\text{s}$ diesel pilot injections. This interaction case shows fast ammonia ignition and high conversion rates (see Section 6.1).

The larger $200 \mu\text{m}$ nozzle leads to a faster rise of the HRR and a broader profile, indicating more diffusive combustion compared to the $110 \mu\text{m}$ nozzle. In particular, the two 5 mg diesel pilot injections illustrate that the shorter injection with a higher mass flux leads to a steeper rise of the HRR, i.e.

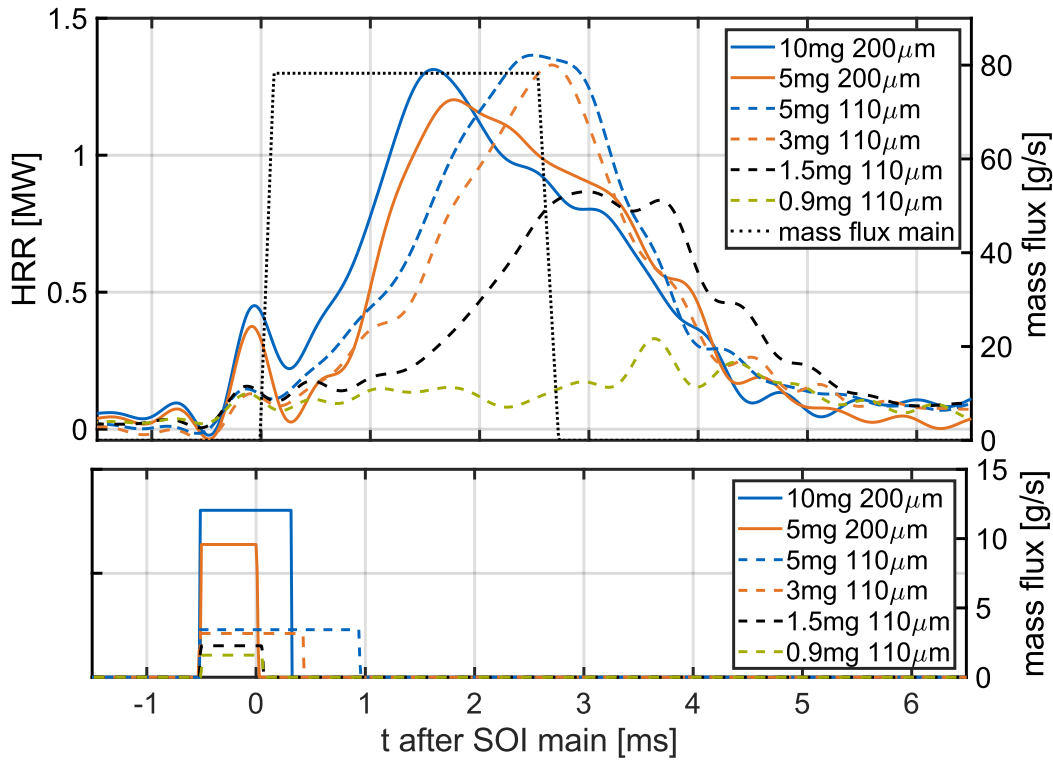


Figure 6.4: Diesel mass fluxes (bottom), ammonia mass flux (top), and averaged apparent HRRs (top) for different, slightly advanced ($+500 \mu\text{s}$) diesel pilots at OP4 and converging sprays ($\alpha = -7.5^\circ$).

a more intense onset of ammonia combustion. While the ignition delay is lower for the larger nozzle, the overall combustion duration is shorter for the smaller diesel nozzle. One of the two HRR shapes obtained with the 5 mg diesel pilot injection might be favored depending on the desired combustion characteristics. The HRRs obtained with 10 mg and 5 mg $200 \mu\text{m}$ injections are similar, apart from the expected faster rise in HRR when employing a larger pilot. Ammonia ignites for pilots as small as 1.5 mg, which equals a fraction of 1.6 % of the total injected LHV. However, a reduction of the pilot fuel mass below 3 mg (LHV fraction of 3.2 %) leads to a slow rise of the HRR, as quenching on the cylinder wall and lean-out of the ammonia spray become more significant. Therefore, only a smaller fraction of the heat release of the other cases is observed for the 1.5 mg pilot. Although some combustion occurs, no clear peak HRR can be identified for the 1 mg injection.

Apart from the injected mass, the investigated diesel injection scenarios differ in various properties, such as penetration, spray angle, and injection duration. Therefore, an unambiguous explanation for the observed combustion behavior is impossible. Although the presented findings are specific to the investigated interaction case and operating point, the study shows that the pilot characteristics significantly influence the ammonia spray's combustion behavior.

The presented results reveal that the combustion characteristics of ammonia sprays depend significantly on the interaction with the diesel pilot during the ignition phase. Therefore, the combustion behavior is sensitive to pilot size, timing, and spatial interaction. This behavior constitutes a vital difference to more reactive fuels, such as methane, where HRR characteristics are mainly correlated to the degree of premixing before ignition of the main fuel [70]. The following chapters will explain the observed behavior using optical imaging techniques.

7 Optical Characterization

This chapter provides deeper insight into the combustion process via optical studies. The unique CL features of the ammonia flame (e.g. NH^* and NH_2^* emissions) allow spectroscopic measurements to distinguish between the combustion of carbon-based pilot fuels and ammonia. In addition, SG, OH^* CL, and NL imaging results complement the spectroscopic measurements by enabling a spatial allocation of the flame's emissions. Furthermore, the data obtained serves as a basis to interpret the luminosity observed during combustion and reveals the suitability of different wavelength ranges for CL measurements of diesel-piloted ammonia spray flames.

The chapter is structured as follows: The first section discusses temporally and spatially integrated spectra to reveal which species contribute significantly to the observable natural flame emissions. Then, time-resolved flame spectra are discussed in context with SG, OH^* CL, and NL images to characterize the combustion process with a focus on flame transition. Finally, background corrected NH^* , OH^* , NH_2^* , and broadband luminosity intensity evolutions are extracted from the spectra and discussed in context with the HRR.

Each case is repeated three times for each measurement technique. The HRRs are averaged over all experiments conducted for the combustion case, while the spectroscopic data is averaged over the three experiments conducted for each grating. The 2D imaging data is taken from the cases with the HRRs most similar to the averaged HRRs. The spatial and temporal interaction remain fixed at an interaction angle of $\alpha = -7.5^\circ$, and a slightly advanced 5 mg diesel pilot (+500 μs). The optical studies use the smaller 5 mg diesel pilot injection, which produces less soot and increases the quality of the flame emission spectra and SG images obtained. The chapter investigates the charge conditions corresponding to OP3 (98 bar, 865 K) and OP4 (125 bar, 920 K). The lower soot production of experiments at OP3 enables the investigation of

flame emissions in the UV and VIS range. In contrast, experiments obtained at OP4 can only be investigated in the UV range, where soot luminosity is weak. The timings in this chapter refer to the start of diesel injection. The 0.94 mm ammonia nozzle is used with an injection pressure of 530 bar (see Table 4.2).

7.1 Integral Flame Spectra

Spatially and temporally integrating the flame emissions results in well-defined spectra suitable for identifying individual peaks and the corresponding species. This procedure creates a basis for discussing the temporal evolution of the spectra in more detail in subsequent sections. Figure 7.1 shows the integral flame emissions obtained by temporal and spatial integration during an experiment at OP3. While the spatial integration is conducted over the entire combustion chamber for diesel, the combustion chamber region starting from 20 mm downstream of the diesel nozzle is considered for the ammonia spectra to exclude the influence of diesel combustion due to injector dripping. The diesel spectrum is obtained by temporally integrating up to 900 μs after SOI. In comparison, the ammonia spectrum results from integrating between 1600 μs to 6000 μs after SOI (of diesel). As diesel is injected before ammonia, diesel combustion progresses undisturbed at first. Subsequently, the sprays interact, and both fuels burn simultaneously from approximately 900 μs to 1600 μs after SOI. This flame transition period is not included in the analysis conducted in this section and is discussed in more detail in the next section. Figure 7.2 shows the corresponding HRRs and injection mass fluxes.

The UV range of the ammonia flame spectrum shown in Figure 7.1 b (grating 3, left part) and c (grating 2) consists of the distinct NH^* (A-X (0,0)) peak system at 336 nm and the OH^* (A-X (0,0)/(1,1)) peak system at around 308 nm superimposed on weak broadband radiation. A weak peak visible at 282 nm results from OH^* (A-X(1,0)). Continuous broadband CL is observed for wavelengths longer than 400 nm (see Figure 7.1 b). A possible source for this radiation is the CL of NO_2^* .

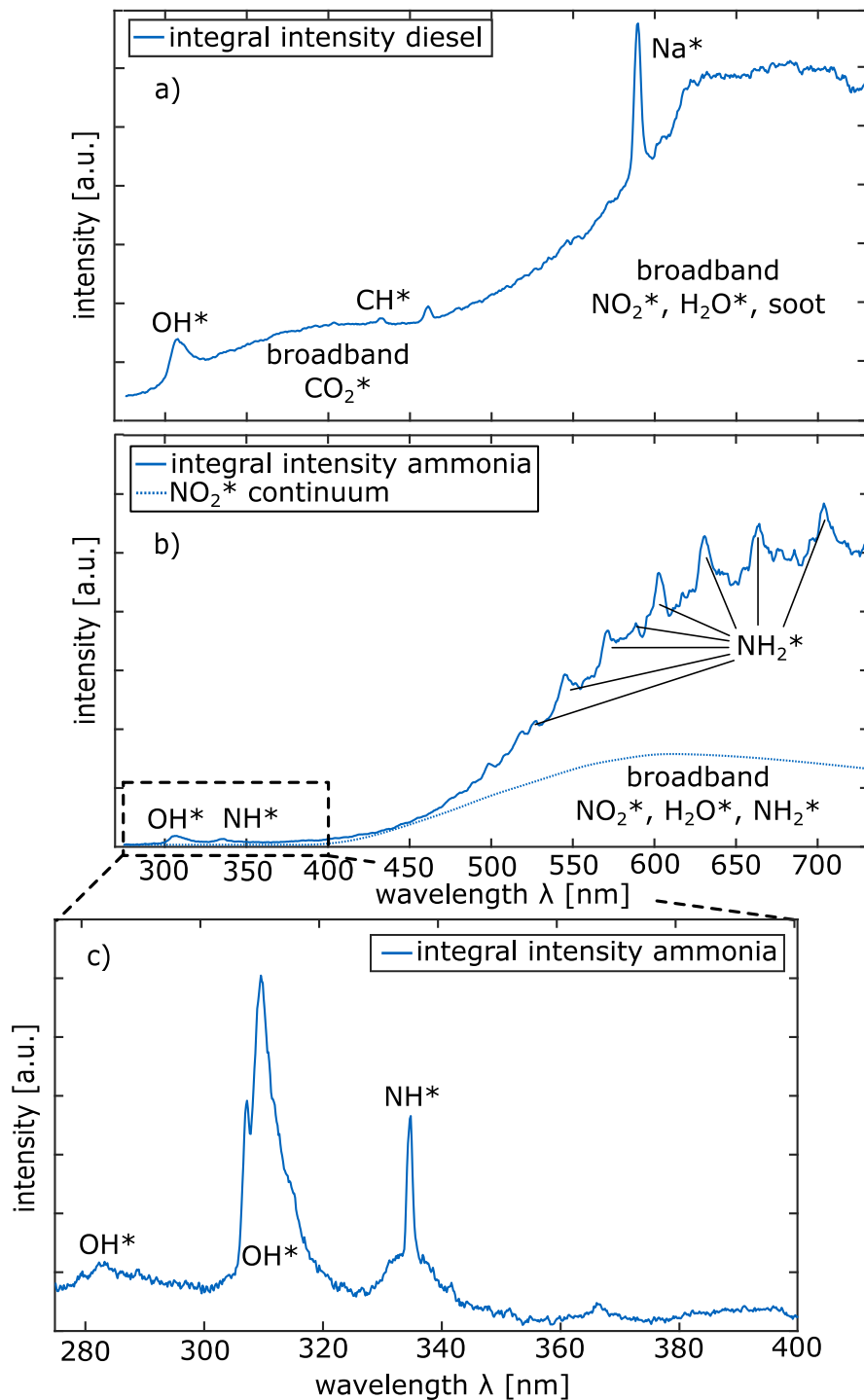


Figure 7.1: Spatially and temporally integrated spectra obtained at OP3. (a) and (b) were obtained using grating 3, while (c) was obtained using grating 2. (b) and (c) are obtained by temporal integration from 1600–6000 μ s after SOI, while (a) is integrated until 900 μ s after SOI.

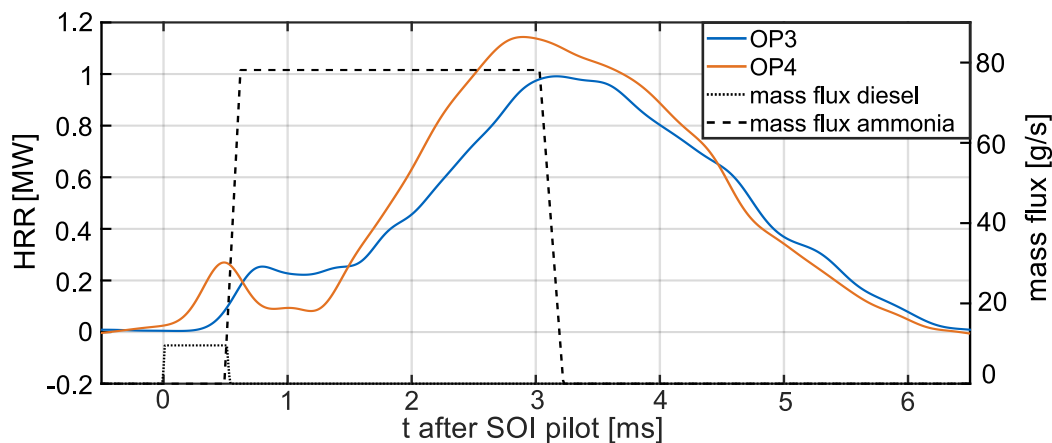


Figure 7.2: HRR and mass fluxes of the investigated combustion cases featuring a slightly advanced diesel pilot injection (+500 μ s).

The approach by Sheehe and Jackson [127] is adopted to test whether NO_2^* can explain the broadband emissions observed for the ammonia flame. For this purpose, the NO_2^* intensity distribution presented by [128] is compared to the spectrum obtained in this work (see Figure 7.1 b). The NO_2^* intensity distribution is fitted to the ammonia flame emission spectrum so that the NO_2^* emissions do not exceed the ammonia flame emission intensity at any wavelength. As a result, the NO_2^* intensity distribution fits well in a range from 400 nm to approximately 450 nm. However, the ammonia flame's broadband emissions are more intense for wavelengths above 450 nm than to be expected if only NO_2^* was contributing to its flame emissions. Therefore, the maximum possible contribution of NO_2^* to the flame luminosity during ammonia combustion is small. The broadband emissions unaccounted for by NO_2^* may be attributed to H_2O^* and NH_2^* [91]. In addition, the NH_2^* peaks of the ammonia α band superimpose on the broadband spectrum.

In addition to the OH^* (A-X (0,0)/(1,1)) peak system, the diesel spectrum (Figure 7.1 a) shows more intense broadband radiation in the UV range. This radiation arises from HCO (Vaidya's hydrocarbon flame bands), HCHO (Emeleus's cool flame bands), and CO_2^* [13, 129, 130]. A weak CH^* peak (A-X (0,0)) is visible at 432 nm. The highly bright sodium D-line at 589 nm arises from sodium impurities in the diesel fuel. An additional peak at approximately 460 nm could not be identified and is thought to be caused by other impurities

in the diesel fuel. Similar to the ammonia case, broadband emissions at longer wavelengths arise from NO_2^* and H_2O^* . In addition, weak soot luminosity occurs. The absence of distinct features of diesel combustion in the ammonia emission spectra clearly shows that the ammonia combustion phase starting from $1600\ \mu\text{s}$ after SOI, in which the major part of heat release occurs (see Figure 7.2), is not directly supported by diesel fuel combustion. However, hot diesel combustion products, e.g. located on the spray edges, may still influence the ammonia spray's combustion.

7.2 Temporal and Spatial Evolution of Flame Emissions

This section discusses the temporal and spatial evolution of flame emissions to improve the understanding of the ongoing processes. Figure 7.3 and Figure 7.4 show the temporal evolution of SG, OH^* CL and NL images during combustion for $t = 700 - 1600\ \mu\text{s}$ and $t = 2000 - 5000\ \mu\text{s}$, respectively. In addition, Figure 7.5 presents the corresponding temporal evolution of flame spectra. While SG and OH^* CL images are taken simultaneously, NL and spectroscopy imaging can only be performed one at a time, which requires sequential experiments. The combustion chamber conditions correspond to OP3.

First weak NL occurs during diesel ignition at $t = 700\ \mu\text{s}$ (see Figure 7.3). The flame spectra (see Figure 7.5 a) indicate first broadband CL with only weak OH^* luminosity at $t = 750\ \mu\text{s}$, which hints at cool flame ignition chemistry contributing to the flame emissions observed. However, as experiments are averaged over three repetitions and the camera's exposure time was set to $t = 40\ \mu\text{s}$, no isolated spectrum containing only cool flame chemistry is obtained. Subsequently, flame emission intensity increases, and the corresponding peaks (e.g. OH^* , CH^* , and the sodium D-line) become more prominent in the spectra. At $t = 850\ \mu\text{s}$, both OH^* CL and NL encompass the entire diesel spray. Although the ammonia spray starts interacting with the diesel spray at approximately $t = 750\ \mu\text{s}$, no sign of ammonia-specific flame emissions, such as NH^* and NH_2^* , can be observed in the spectra until $t = 1000\ \mu\text{s}$.

7.2 Temporal and Spatial Evolution of Flame Emissions

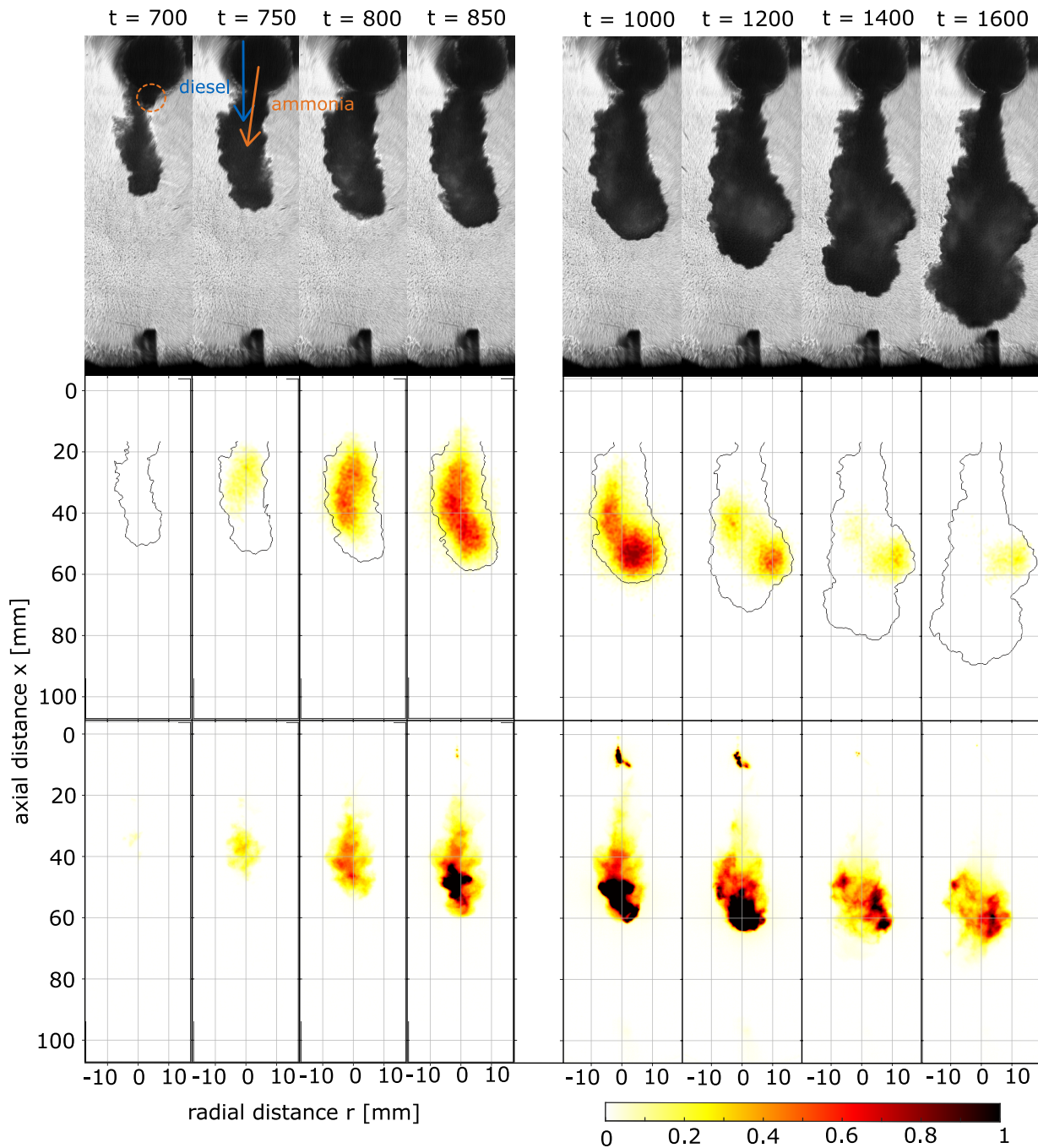


Figure 7.3: SG (top), OH* CL with overlaid SG contours (middle) and NL (bottom) imaging at OP3. The left section contains images taken during pilot ignition ($t = 700 - 850$ μs after SOI). The right section contains images taken during the flame transition from diesel to ammonia ($t = 1000 - 1600$ μs after SOI).

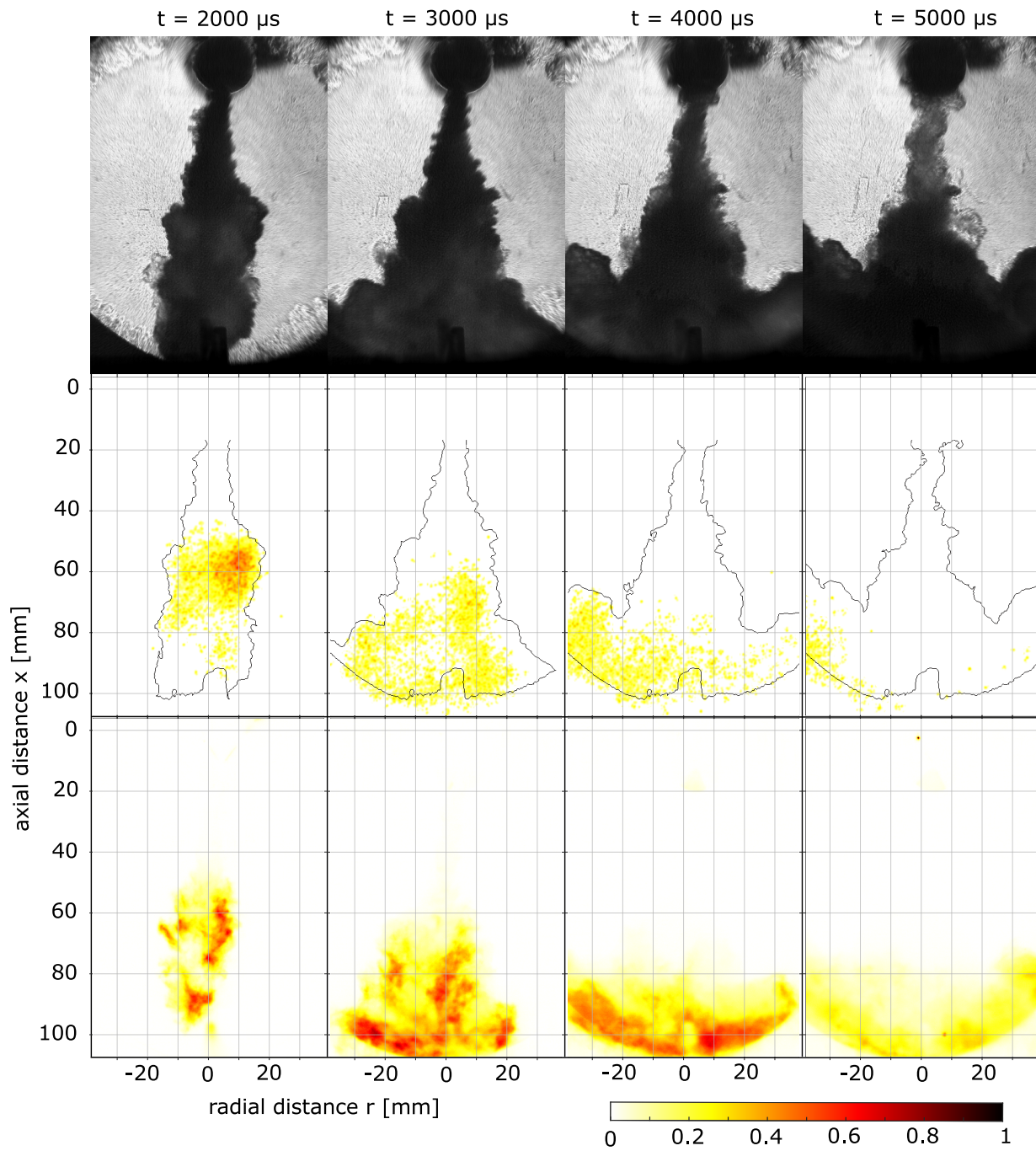


Figure 7.4: SG (top), OH^* CL with overlaid SG contours (middle) and NL (bottom) imaging at OP3. OH^* intensities are γ -corrected ($\gamma = 0.4$). The images are taken during the main fuel combustion phase, in which ammonia is burning ($t = 2000 - 5000 \mu\text{s}$ after SOI).

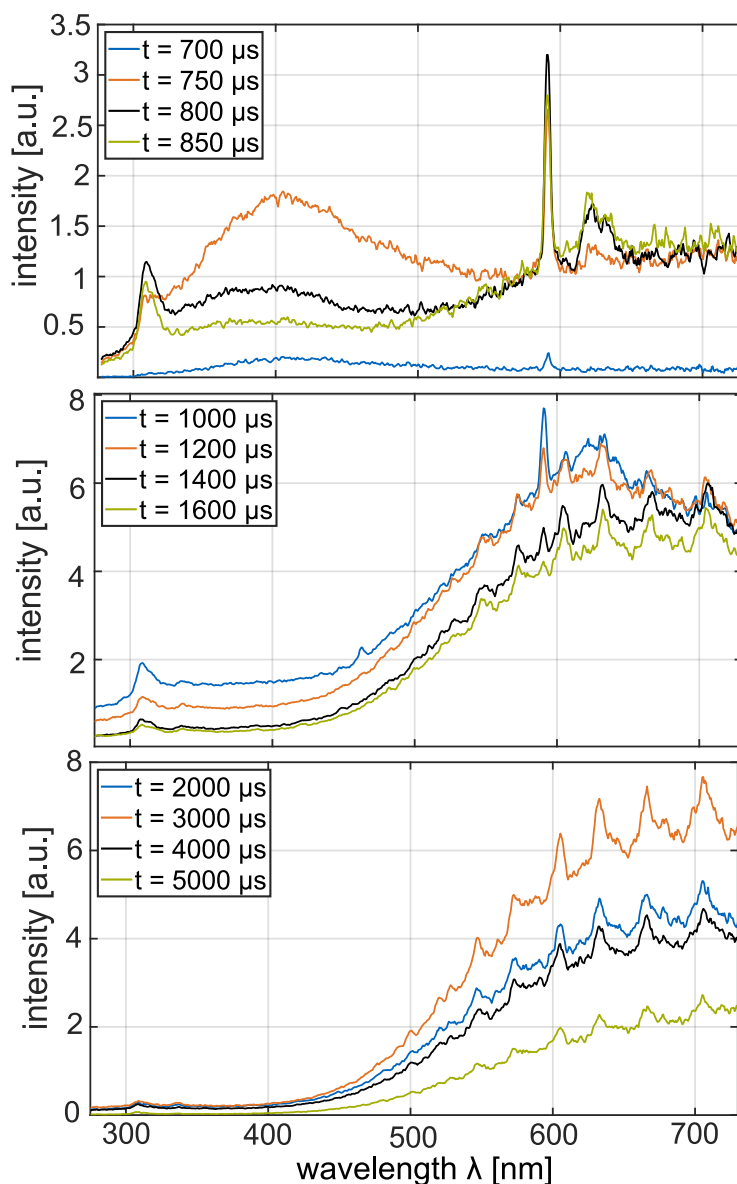


Figure 7.5: Spatially integrated flame emission spectra at different times during diesel pilot ignition (a), the flame transition from diesel to ammonia (b), and ammonia combustion (c) at OP3.

At $t = 1000 \mu\text{s}$, NH^* and NH_2^* peaks first emerge on the spectra (see Figure 7.5 b). Simultaneously, OH^* CL decreases, reflected both in the spectra and the OH^* CL images. The decrease starts at $t = 1000 \mu\text{s}$ on the side, where ammonia interacts with the diesel cloud first (right), before an intense reduction of the CL in almost the entire spray occurs. At $t = 1600 \mu\text{s}$, intense

OH* CL is restricted to a small pocket of gases on the sides of the spray, which most likely contains diesel combustion products. The emission spectra from $t = 1000 \mu\text{s}$ to $t = 1600 \mu\text{s}$ show a decrease in overall intensity. The UV emission intensity drops to particularly low levels. The emergence of the NH₂* peaks and the decline of the sodium D-line mark the shift from diesel to ammonia combustion. The OH* CL and NL locations indicate that the flame does not encompass the ammonia spray tip in this combustion phase. Instead, the reaction zone location changes only slightly during the flame transition process while the ammonia spray penetrates into the combustion chamber. Therefore, unburned ammonia emissions may originate in the spray tip region. This behavior is attributed to the low ignitability of ammonia. In addition, the tip region features the typical fuel-rich head vortex, which shows particularly poor mixture formation, resulting in slower evaporation and lower temperatures [16, 125]. Furthermore, the HRR does not increase significantly between $t = 1000 - 1600 \mu\text{s}$, indicating slow and limited ammonia combustion in this phase. In contrast to recent spectroscopic studies burning ammonia and a second, carbon-containing fuel [89–91], the recorded spectra lack CN* peaks (e.g. B-X(0,0) and B-X(1,1) around 388 nm) during the entire combustion event. As CN originates from interactions between carbon- and nitrogen-containing fuels, the lack of its flame emissions hints at low rates of inter-species reactions between ammonia and diesel for the combustion process investigated in this work. The NH* peak is weak during the flame transition and subsequent phases. The low relative intensity of the NH* peak compared to the diesel background radiation intensity in the respective wavelength range may prohibit its use as a flame marker for optical combustion diagnostics.

During later combustion phases, the flame spectra do not show major qualitative changes apart from different intensities (see Figure 7.5 c). The UV emissions, in particular OH* CL, become weaker, while the peak intensity of visible broadband CL is reached between $t = 2000 \mu\text{s}$ and $t = 3000 \mu\text{s}$. Both OH* CL and NL drift off from the injector until and after the end of injection at $t = 3200 \mu\text{s}$ (see Figure 7.4). Therefore, combustion progresses close to the cylinder wall, and more air entrains up to the flame front. As a result, average equivalence ratios become leaner, and combustion temperatures drop. This lack of flame stabilization shows that the spray stabilization mechanisms

introduced in Section 2.3 are inhibited by ammonia's physical properties (see Section 3.2). Section 8 investigates the observed lack of flame stabilization in more detail. As OH^* CL gradually weakens, it cannot be detected reliably for later combustion phases, while NL still permits proper observation of the combustion event.

Apart from improving the understanding of the HPDF combustion process, the insights obtained in this section help choose suitable methods for future optical investigations of diesel-piloted ammonia combustion. Focusing on wavelengths that capture NH_2^* CL is suggested for cases with low soot formation, as they offer a strong signal, mainly from the flame front during ammonia combustion. Although UV flame emissions are much stronger during pilot combustion, cases with strongly sooting diesel combustion might require observing wavelengths in the UV range. The best option available is the observation of established OH^* CL wavelengths (around 308 nm), as they offer the strongest absolute and relative signal during ammonia combustion. Observing the wavelengths relevant for NH^* CL (around 336 nm) is not recommended, as diesel UV broadband emissions are strong relative to the intensity of the narrow NH^* peak in this range.

7.3 Temporal Evolution of Background Corrected Intensities

Isolating the contribution of single species to flame emissions enables a profound discussion of their evolution during combustion. The data presented in this section is derived according to the procedure described in Section 5.2.3.

Figure 7.6 a shows the temporal evolution of background corrected intensities of OH^* , NH_2^* , and broadband luminosity in the lower reactivity case OP3. Each intensity is normalized with its highest value. OH^* and broadband luminosity rise sharply after diesel ignition at $t \approx 750 \mu\text{s}$, with broadband luminosity reaching its first peak slightly earlier. Both intensities start declining almost immediately, as pilot injection ends at $t = 520 \mu\text{s}$, and no new diesel fuel is supplied to the reaction zone. At $t \approx 900 \mu\text{s}$, NH_2^* intensity increases

as ammonia starts reacting. Starting from $t \approx 1600 \mu\text{s}$, broadband luminosity and NH_2^* intensity correlate strongly, indicating that the flame luminosity results from ammonia combustion only. Therefore, the background corrected intensities corroborate the findings inferred from the raw spectra presented in Section 7.1 and 7.2. After a short pure pilot combustion phase, the flame transition occurs in which both fuels contribute to combustion. However, the heat release during this transition phase is low (see Figure 7.2). The main part of heat release occurs during ammonia-only combustion.

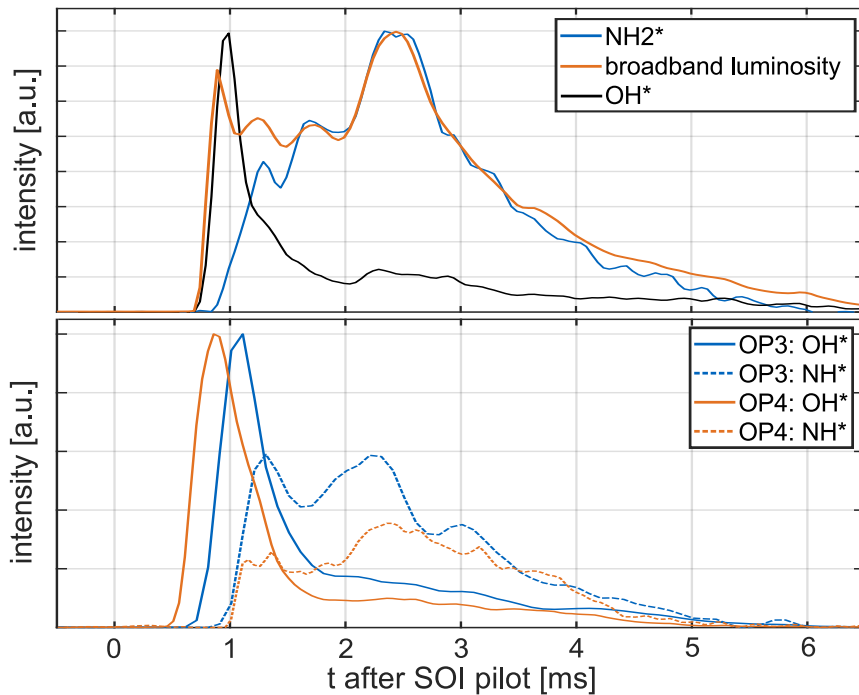


Figure 7.6: Temporal evolution of background corrected CL intensities. Top: OH^* , NH_2^* , and broadband luminosity for OP3. Bottom: OH^* and NH^* for OP3 and OP4.

Furthermore, the strong correlation between NH_2^* peak intensity and broadband luminosity suggests that a significant part of the ammonia flame emissions results from NH_2^* under the conditions investigated. The correlation is particularly strong in the time interval $t \approx 1600 - 3300 \mu\text{s}$. Afterward, broadband luminosity intensity increases relative to the NH_2^* intensity, which indicates the increasing importance of other flame emissions, such as NO_2^* CL. NH_2 mainly occurs close to the flame front, as converting ammonia to NH_2 via hydrogen abstraction is generally the first step of most ammonia

oxidation mechanisms [131]. Therefore, the visible flame emissions of the ammonia spray flame are a suitable indicator for the flame front during ammonia combustion. The findings align with a recent study on visible ammonia flame emissions from atmospheric burner flames. Weng et al. [123] found that NH_2^* radiation is the main source of CL at the flame front for fuel-rich and fuel-lean flames. In the post-flame zone, NH_2^* is the main contributor to flame emissions for fuel-rich flames, while NO_2^* radiation is the most important contributor under fuel-lean conditions. Equivalence ratios are non-uniform for spray combustion and subject to temporal and spatial variations. However, the general trend as combustion progresses and the lift-off length increases is a shift from conditions that show more NH_2^* radiation (high equivalence ratios, smaller amount of gas in post-flame zone) to conditions that show more NO_2^* CL (lower equivalence ratios, more gas in post-flame zone). In full engines, the pressure and temperature rise due to combustion usually leads to ongoing reactions in the burned charge, e.g. caused by shifts in the chemical equilibrium. Owing to the low fuel mass supplied by the single-hole injectors, this pressure rise due to combustion is low in the RCEM. Therefore, practical engines may show more intense chemiluminescence in the burned zone.

Figure 7.6 b shows the background corrected OH^* and NH^* intensities of both operating points investigated. The intensities are obtained by analyzing the UV spectra (grating 2), as sooting diesel pilot combustion at OP4 prohibits the investigation of longer wavelengths. As different image intensifier gains impede the direct comparability of the intensities of the two operating points, both intensities are normalized with the highest value of OH^* intensity occurring for the respective operating point.

The pilot ignition delay is shorter for OP4 due to more reactive conditions, which results in an earlier onset of OH^* CL and heat release (see Figure 7.2). The HRR of OP4 shows a more prolonged delay between pilot combustion and ammonia combustion due to the earlier pilot ignition. While the shape of OH^* CL intensity is similar for both cases, the absolute OH^* intensity was much higher for OP4 due to higher temperatures. Higher combustion temperatures in OP4 result from higher air temperature and higher equivalence ratios due to less mixing of fuel and air during the shorter ignition delay. A slightly

earlier onset of NH^* emissions for OP3 can be attributed to lower charge air density and the resulting faster spray penetration, as is apparent from well-known spray penetration correlations (e.g. [8, 47]). NH^* CL intensity is lower for OP4 than OH^* intensity due to the more intense OH^* CL mentioned above. Both NH^* intensities peak twice, directly after ammonia ignition and before the peak HRR. While the second peak is expected based on ammonia combustion intensity, the first peak is thought to result from increased NH production as entrained diesel combustion products lead to higher combustion temperatures [101]. Furthermore, the high OH concentration produced during diesel combustion increases NH concentration via the reaction $\text{NH}_2 + \text{OH} \rightarrow \text{NH} + \text{H}_2\text{O}$ [90]. As expected, temperature, pressure, equivalence ratio, and strain rate variations prohibit any direct correlation between HRR and CL intensity.

8 Mixture Formation and Flame Stabilization

The optical investigations introduced in Section 7 reveal that ammonia sprays fail to stabilize at a certain distance from the injector nozzle. This section investigates the spray stabilization behavior in more detail. For this purpose, experiments with different injection pressures and spray velocities are conducted, and the resulting lift-off length evolutions are analyzed. Furthermore, 1-D spray model results reveal equivalence ratios and temperatures in the ammonia sprays, which helps to interpret the results.

The first section validates the spray model against experimental data for gaseous penetration and stationary liquid length for two different ammonia nozzles. Then, the experimentally determined lift-off length evolutions are presented and discussed. The subsequent section shows the equivalence ratio and temperature distributions within the ammonia sprays employed. Subsequently, the effect of the determined temperature and equivalence ratio distributions on ammonia's flame stabilization behavior is scrutinized. The final subsection discusses the implications of non-stabilized ammonia flames on combustion characteristics and pollutant formation behavior. The high dependency of ammonia spray combustion on pilot interaction observed in Chapter 7 is highlighted in particular.

8.1 Mixture Formation Model Validation

This section compares gaseous penetration and liquid length predictions with experimental results to validate the 1-D model. The validation is conducted at OP4 for the 0.94 mm and the 0.98 mm ammonia nozzle at injection pressures

of 530 bar and 265 bar, respectively (see Table 4.2). The injection configuration used for the 0.94 mm nozzle matches the configurations used in Chapters 6 and 7. The configuration used for the 0.98 mm nozzle represents the case with the lowest injection pressure used for the combustion experiments in this chapter (see Section 8.2).

The maximum gaseous penetration curve (obtained by SG) and the maximum liquid penetration over time (obtained by MS) are measured three times each and compared with the modeled penetration and stationary liquid length for the two test cases presented. Owing to the blocking of the optical trajectory by the injector body, it was possible to determine gaseous penetration only after reaching a penetration of 18 mm. Liquid penetration could be determined only after reaching more than approximately 25 mm, as the laser sheet did not extend over the entire combustion chamber to avoid laser reflections onto the camera sensor. The combustion chamber is filled with air, as no ignition occurred under the conditions investigated.

Figure 8.1 shows that the experimental and model results correlate well for both test cases. Liquid penetration reaches stationary values after penetrating similarly to gaseous penetration in the early injection phases. Although predicted in the literature (e.g. [16]), liquid over-penetration over the stationary value owing to a fuel-rich head vortex is not observed, which correlates with other experimental observations [118, 132]. Because of turbulence, the experimentally determined liquid length shows fluctuations around its stationary value. Overall, the correlation sufficiently validates the spray model for the conditions investigated. The spray model can be applied to different injection pressures, as injection pressure does not influence mixture composition at a specific position under diesel-like conditions [48, 52, 105]. The injection pressure does, however, influence the temporal evolution of equivalence ratios in sprays. The model provides spray properties that are not readily accessible via experimental means, such as equivalence ratio and temperature distributions within the spray. These properties explain ammonia spray combustion behavior in Section 8.4.

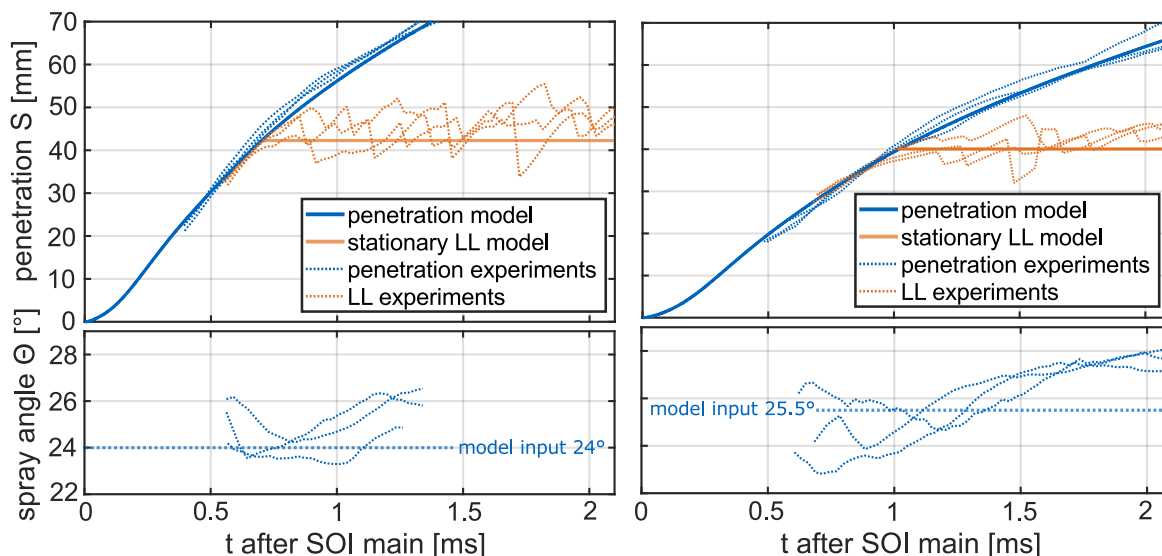


Figure 8.1: Experimental results at OP4 for ammonia penetration, liquid length, and spray angle, as well as model predictions for penetration and stationary liquid length for the 0.94 mm nozzle at 530 bar with an injection mass of 210 mg (left) and the 0.98 mm nozzle at 265 bar with an injection mass of 125 mg (right).

8.2 Combustion Experiments

The combustion experiments presented in this chapter employ injection pressures and injection masses of 265 bar/125 mg, 360 bar/160 mg, 460 bar/190 mg, and 560 bar/220 mg to evaluate the influence of spray velocities on the lift-off length evolution. The experiments use the 0.98 mm nozzle to inject ammonia 0.5 ms after a 5 mg diesel pilot injection for 2.7 ms with a slightly converging spray interaction angle of $\alpha = -7.5^\circ$ at OP4.

Figure 8.2 shows superimposed SG and OH* CL images of a diesel-piloted ammonia combustion case. The superposition of OH* and SG images allows the direct spatial correlation of information contained in both images. Diesel is injected first (at $t = -500 \mu\text{s}$) and emits soot luminosity and OH* radiation after auto-ignition. As a result of converging spray angles, the ammonia spray is covered by the diesel cloud. It is barely visible until its penetration exceeds the penetration of diesel at $t = 804 \mu\text{s}$.

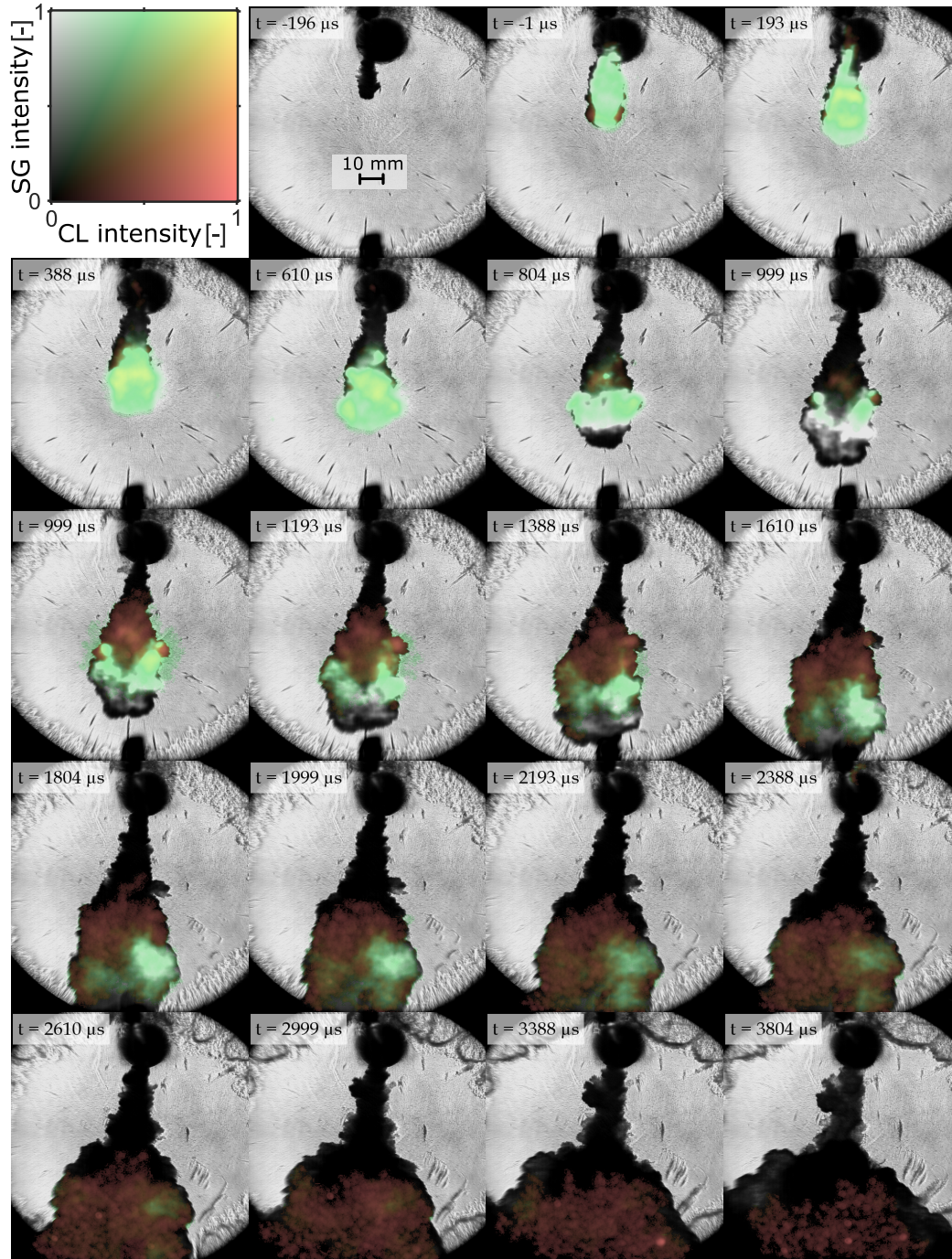


Figure 8.2: Simultaneously acquired and superimposed SG and CL images of diesel-piloted ammonia combustion at OP4 with 190 mg ammonia (injection pressure of 460 bar, 0.98 mm nozzle).

The burning ammonia spray impinges on the cylinder wall at $t = 1804 \mu\text{s}$. After the end of ammonia injection at $t = 2700 \mu\text{s}$, OH^* intensity slowly declines. Owing to different OH^* intensities during combustion, the images are brightness-corrected to render the combustion event visible at all times (see Section 5.2.2). Brightness is corrected by potentiating each pixel's intensity value with 0.5 at $t < 1000 \mu\text{s}$ and 0.3 at $t > 1000 \mu\text{s}$. The image taken at $t = 999 \mu\text{s}$ is shown after correction with both values in Figure 8.2 for illustration purposes.

Figure 8.3 shows HRRs, mean OH^* intensities, lift-off lengths, and parametrized injection mass fluxes of diesel and ammonia for the four cases investigated. The results are based on two repetitions for the 190 mg and 220 mg cases and three repetitions for the 125 mg and 160 mg cases. Due to lower spray velocities, the heat release is strongly delayed for the lower injection pressures, as the ammonia sprays only interact with diesel products after some time. The time of maximum HRR coincides with the first contact of ammonia with the cylinder wall, which hints at quenching effects (see Figure 8.2).

The mean OH^* CL intensities of all pixels within the region shown are normalized with their highest value during combustion. The CL intensity increases after the start of diesel combustion until its maximum value is reached. Subsequently, due to interaction with the ammonia spray and increasing diesel burnout, OH^* intensity decreases until it stabilizes at a much lower level during ammonia combustion. The decline of the CL intensity is faster at higher injection pressure and accompanied by a faster rise in HRR. This faster rise indicates earlier and more intense interaction between diesel and ammonia at higher injection pressures. OH^* intensity eventually fades out when the HRRs decline.

The lift-off lengths are examined to evaluate the spray stabilization behavior. This examination is only possible after the strong OH^* intensity caused by diesel combustion has declined. Therefore, Figure 8.3 only shows lift-off lengths after $t = 1000 \mu\text{s}$ to $t = 2000 \mu\text{s}$, depending on the combustion case. For all four ammonia injection pressures, the lift-off length increases almost linearly over time, even after the end of ammonia injection, until the OH^*

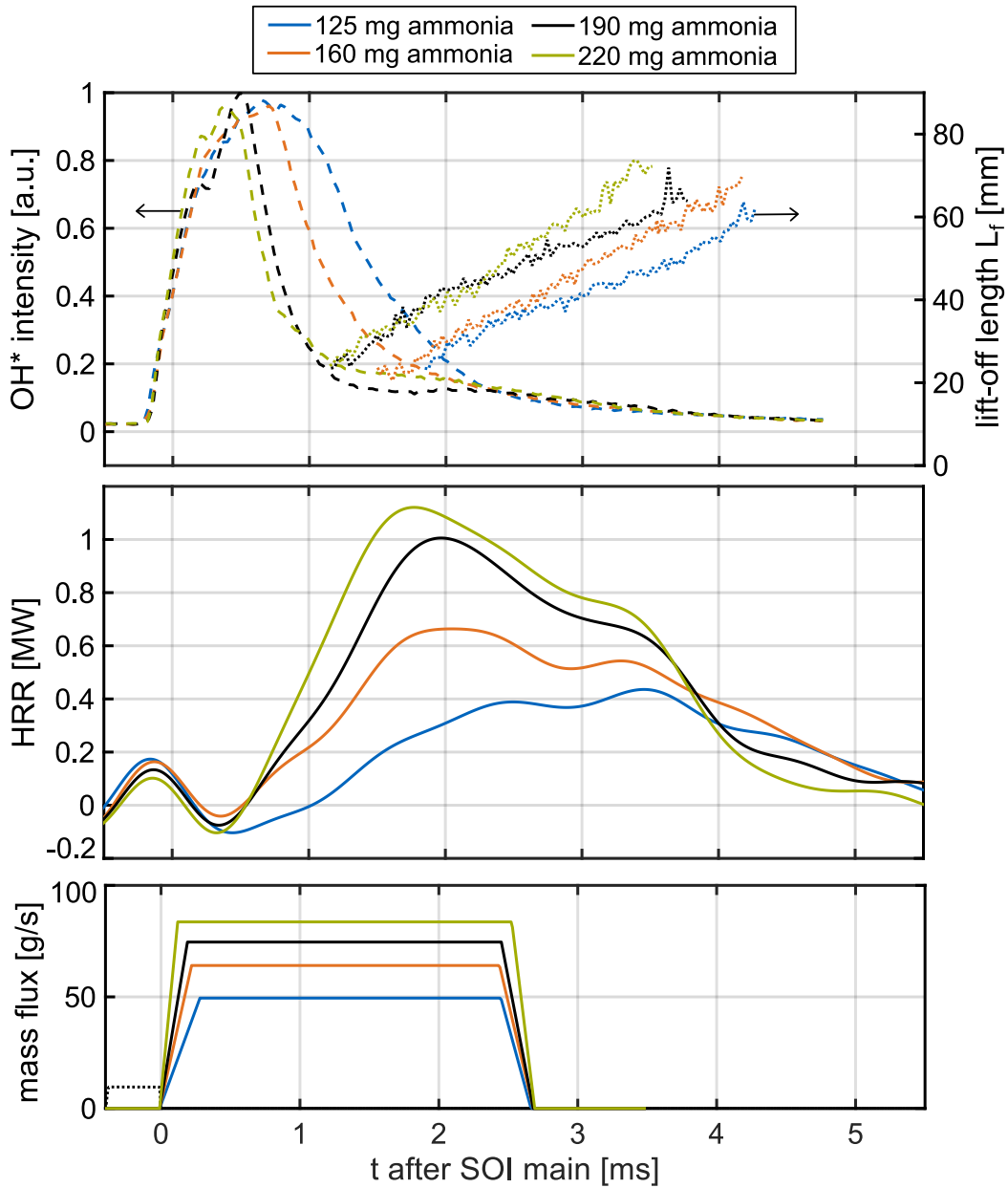


Figure 8.3: Normalized mean OH* intensities (top), lift-off length evolutions (top), averaged HRRs (middle), and parametrized injection mass fluxes of diesel and ammonia (bottom) for ammonia mass and injection pressures of 125 mg/265 bar, 160 mg/360 bar, 190 mg/460 bar and 220 mg/560 bar.

intensities become too weak to be detected reliably. The increase in lift-off length is slightly faster for higher ammonia injection pressures. This contin-

uous increase indicates that diesel-piloted single ammonia spray flames cannot stabilize under engine-relevant conditions and time frames. However, the blow-off is slow, and combustion is not completely quenched. The drift velocity of the flame front increases from approximately 15 m/s at 265 bar to 18 m/s at 560 bar. This increase is much less than expected based on the increase in injection velocity, which is proportional to the square root of the relative injection pressure according to Bernoulli's equation. When assuming a counter-pressure of 125 bar, the injection velocity increases by 76% when increasing the injection pressure from 265 bar to 560 bar. The 76% also closely match the experimentally determined increase in injection mass from 125 mg to 220 mg when increasing the injection pressure from 265 bar to 560 bar.

8.3 Mixture Formation

Figure 8.4 shows modeled ammonia spray equivalence ratios, gas phase temperature contours, as well as center line and radially averaged values along the spray axis. The results are valid for stationary, non-reacting ammonia sprays, which approximate the state within the examined ammonia sprays up to their lift-off length. The results are valid independent of injection pressure as argued in Section 8.1. Therefore, all experimental conditions employed in Section 8.2 are covered. The maximum depicted axial distance from the nozzle exit of 80 mm is close to the maximum observed lift-off length (see Figure 8.3). Complete vaporization occurs for equivalence ratios of $\phi = 3.17$. On the spray axis, this equivalence ratio is reached at a distance of 40 mm from the nozzle exit, which determines the liquid length (see Section 8.1). When considering the radially averaged equivalence ratio, stoichiometric conditions are already reached at a distance of 31 mm from the nozzle exit, which is significantly upstream of the liquid length. However, central regions remain fuel-rich further downstream. The kink, which is visible in the center line equivalence ratio at 15 mm, results from the completion of the transition from a top-hat profile to a fully developed jet (see Section 5.3). Vaporization occurs at 361 K, while stoichiometric conditions are reached at 640 K. Even at equivalence ratios of only $\phi = 0.1$, the temperature does not exceed 877 K, which is below the minimum

auto-ignition temperature of ammonia of 924 K (see Table 3.1). Generally, regions near the nozzle exit are cold and may not have evaporated. Therefore, significant heat input is required to reach reactive conditions. Further downstream, the spray quickly becomes leaner, which results in significant thermal ballast due to the additional air entrainment. As a result, product temperatures after or during combustion decrease.

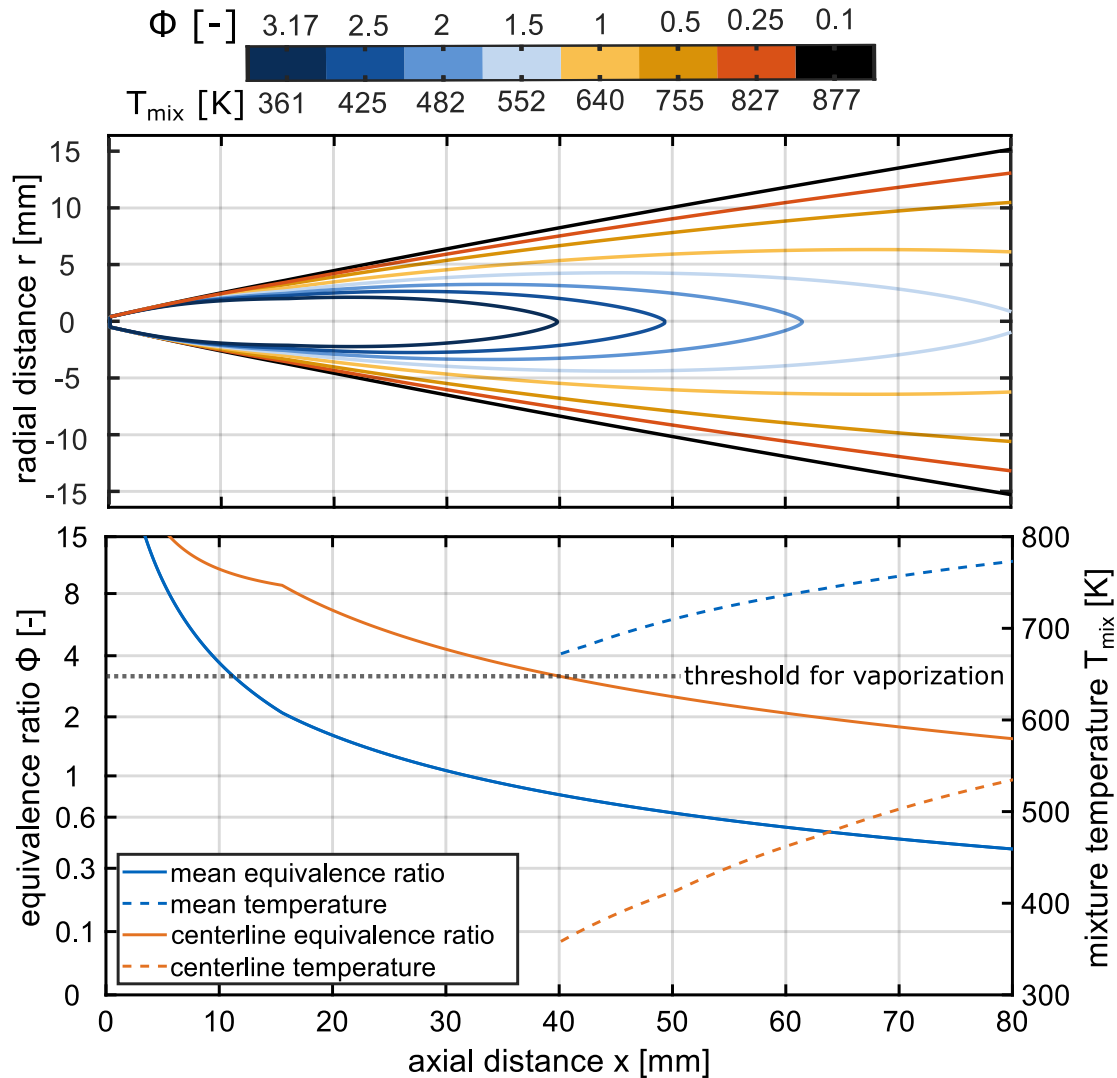


Figure 8.4: Modeled equivalence ratio contours and temperature contours (top), as well as center line and radially averaged equivalence ratios and gas phase temperatures (bottom) for the ammonia sprays examined.

Furthermore, the conservation of momentum yields a mixture velocity for each equivalence ratio. The stoichiometric air demand of ammonia is $6.05 \text{ kg}_{\text{air}}/\text{kg}_{\text{fuel}}$ (see Table 3.1). Therefore, the average convective jet velocity at stoichiometric conditions can be estimated by dividing the ammonia injection velocity by 7.05 (see Figure 5.9). This calculation results in an average stoichiometric mixture velocity of approximately 20 m/s and 35.2 m/s at injection pressures of 265 bar and 560 bar, respectively. Therefore, average convective jet velocities at stoichiometric conditions are only slightly higher than the flame front drift velocity for the low injection pressure case. However, the flame drift velocity does not increase adequately with increasing convective jet velocities due to higher injection pressures. This discrepancy suggests that additional effects apart from triple flame propagation must slow the flame drift down. This simple estimate neglects the intense turbulent flow in sprays. These effects cause the local flow velocity to differ significantly from the mean flow velocity. DNS simulations by Tagliante et al. [73] even show that triple flames in the shear layer of diesel sprays do not propagate preferentially in the upstream direction as turbulence strongly distorts the flow field. Therefore, a potential contribution of triple flame propagation to flame stabilization is unlikely.

8.4 Spray Stabilization by Auto-Ignition

A linear and slow increase of lift-off lengths has already been observed for diesel sprays ignited by laser-induced plasma upstream of their naturally occurring lift-off length [133]. From their findings, Picket et al. suggest a stabilization mechanism based on auto-ignition by re-entrainment of combustion products, owing to turbulent mixing at the jet edges (see Sections 2.3 and 3.2). The information on equivalence ratios and temperatures within the ammonia sprays (see Figure 8.4) provides insight into the mechanisms inhibiting flame stabilization for the sprays investigated in this chapter in more detail than based only on theoretical considerations (see Section 3.2). The range between approximately 20 mm and 70 mm is of particular interest, as the flame's lift-off length evolution covers it. In this range, the thermodynamic states within

the investigated sprays reveal two mechanisms that inhibit flame stabilization by auto-ignition, schematically depicted in Figure 8.5.

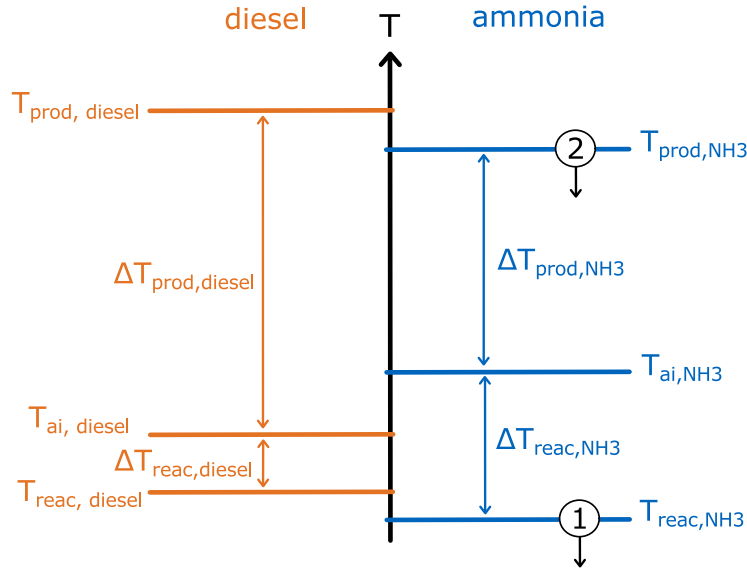


Figure 8.5: Temperature constraints for flame stabilization by auto-ignition for diesel and ammonia. ①: cold educts, owing to high latent heat of vaporization and low air entrainment in upstream regions of the spray. ②: low product temperature, owing to lean equivalence ratios in downstream regions of the spray. Adapted from [17].

First, in regions close to the nozzle exit, evaporative cooling leads to low reactant temperatures $T_{\text{reac,NH}_3}$ due to the large latent heat of vaporization. Due to the high auto-ignition temperature of ammonia, the temperature difference to the auto-ignition temperature $\Delta T_{\text{reac,NH}_3}$ is high. As a result, the amount of hot combustion products that has to be re-entrained into the spray to reach this temperature exceeds the stationary supply, and the flame starts drifting downstream. Second, thermal ballast increases in regions downstream of stoichiometric conditions, which lowers the product temperature $T_{\text{prod,NH}_3}$. Therefore, $\Delta T_{\text{prod,NH}_3}$ decreases and, once again, the mixing requirements for auto-ignition increase. Although reactant temperatures are higher for these longer lift-off lengths, the flame still cannot stabilize. The drifting lift-off length observed in the experimental results (see Section 8.2) covers lift-off lengths between 20 mm and 70 mm. This range includes the near-nozzle regions, where

cold gases and liquid ammonia prevail, and downstream regions, where radially averaged equivalence ratios are lower than $\phi = 0.5$. Therefore, it is unlikely that ammonia sprays would stabilize by auto-ignition further downstream, as equivalence ratios and product temperatures would decrease further. For comparison, Figure 8.5 also includes the states within a diesel spray at an arbitrary lift-off length. The diesel states show a lower auto-ignition temperature and hotter product and reactant temperatures. This configuration enables the hotter reactants to reach auto-ignition temperature with much less entrainment of hot combustion products for the same charge air temperature. Increasing charge air temperatures increases both reactant and product temperature. Therefore, above a certain air temperature, ammonia sprays will stabilize.

The presence of diesel products from pilot combustion will result in a small reservoir of hot diesel products with a temperature that exceeds $T_{\text{prod,NH}_3}$. Therefore, in the experiments conducted, flame stabilization is facilitated compared to pure ammonia spray combustion. As ammonia sprays could not stabilize in the experiments, pure ammonia sprays will also not stabilize under the investigated conditions without diesel products. Investigations in the same RCEM, which used methanol or methane as main fuels for HPDF combustion, observed attached flames with no significant changes in lift-off lengths during combustion, even at less reactive charge conditions of only 75 bar and 780 K [70, 134].

8.5 Implications on Combustion Characteristics and Pollutant Formation

The lack of a self-sustained, stabilized flame explains the high dependence of ammonia spray combustion on interaction with the diesel pilot injection observed in Chapter 6. While the flame of more reactive fuels, such as methane and methanol, spreads upstream and attaches to the injector independently of the ignition location [70, 134], ammonia combustion depends on the ignition location and the presence of hot combustion product reservoirs originating from earlier combustion phases. These combustion product reservoirs may

originate from pilot fuel combustion, as well as from earlier ammonia combustion itself. For example, parallel or diverging spray angles α result in a different location of diesel combustion products during ammonia injection, where less interaction with the ammonia spray occurs. Therefore, a smaller amount of hot combustion products is available for mixing with ammonia. The detrimental effect of smaller pilot amounts can be explained by similar reasoning. Lower compression ratios inherently increase mixing requirements due to lower mixture temperatures. In summary, ammonia spray combustion is path-dependent under the investigated conditions; earlier combustion phases influence later phases. In contrast, more reactive fuels propagate upstream after pilot ignition and attach to the injector, which eliminates the influence of the earlier combustion phases, making the process path-independent.

The observed gradual blow-off leads to high lift-off lengths in later combustion phases. As a result, the regions upstream of the lift-off length remain unburned or partially unburned, which favors high unburned ammonia emissions. As fuel mass in the spray increases with the square of the distance to the nozzle exit [135], the extensive lift-off lengths cause a high potential for unburned fuel in the wake of ammonia sprays. Unburned fuel emissions originating in the wake of diesel fuel sprays present an issue for low-temperature diesel combustion, where high lift-off lengths occur [59]. Furthermore, combustion shifts to lean conditions for higher lift-off lengths, which may be unfavorable in the case of ammonia combustion, as fuel-rich conditions cause lower NO emissions (see Section 3.4). In addition, the greenhouse gas N_2O may originate in low-temperature regions, i.e. the wake of the fuel spray [136] and the lifted lean reaction zone.

Based on the presented results, a diesel fuel post- or intermediate injection is suggested to reduce unburned ammonia emissions by supporting burnout in the wake of the ammonia spray. Chapter 9 investigates this new combustion strategy in detail. Furthermore, preheating ammonia before injection offers the possibility of reducing liquid length and obtaining hotter fuel/air mixtures at the same distance from the nozzle exit. For an increase in fuel temperature of only 50 K, from 293 K to 343 K, the mixing-limited model predicts a decrease of liquid length of about 20% under the conditions investigated. Increasing fuel

temperature on liquid length is powerful when ammonia is used as fuel, as the temperature at which vaporization occurs is low (e.g. 361 K at the conditions investigated). The effect of preheating ammonia is discussed using a $\Phi - T$ map in Section 3.4. As observed by [133], measures that reduce natural lift-off length might reduce the velocity at which the ammonia flame is blown off, even if no flame stabilization is possible within the space and time available. Therefore, if the same mechanism as for diesel combustion determines ammonia spray stabilization behavior, measures that reduce lift-off length cause a slower blow-off or even a stabilized ammonia flame. The results presented in Section 8.2 indicate that a lower injection pressure, which reduces the natural lift-off length, decreases blow-off velocity. However, the decrease in velocity is lower than the decrease in convective jet velocities. In particular, higher charge air temperatures during ammonia injection will facilitate the ammonia flame's stabilization behavior by increasing product and educt temperatures, which decreases the mixing requirements to undergo auto-ignition substantially. Therefore, large heavy-duty engines, featuring high compression ratios and charge air temperatures, may perform much better using ammonia as fuel than smaller engines with less reactive charge conditions.

While the investigations in this work employ single-nozzle injectors, engines employ multi-jet injectors. As a result, additional effects might facilitate spray stabilization compared to the RCEM. The proximity of a diesel spray to its neighboring sprays influences the lift-off length [74, 137]. In addition, lift-off lengths decrease continuously during injection (e.g. [74, 75]). This decrease results from the entrainment of burned gases in the spray and the general pressure and temperature rise due to combustion.

9 Diesel Fuel Post-Injections

The lack of flame stabilization of ammonia spray flames analyzed in Chapter 8 leads to excessive lift-off lengths at the end of injection (EOI). Therefore, the potential for unburned ammonia emissions in the wake region of ammonia sprays is significant. This chapter explores diesel fuel post-injections (PIs) as a measure to reduce unburned ammonia emissions originating in the ammonia spray wake region.

The first section characterizes the diesel-piloted combustion of ammonia sprays with diesel PIs by analyzing superimposed SG images, OH* CL images and HRRs. Then, the influence of PIs on the ammonia conversion rate is presented. The final section discusses the effect of PIs on pollutant formation. All results presented in this section are obtained at OP4 (125 bar, 920 K) using the 0.75 mm and the 0.98 mm ammonia nozzles at injection pressures of 435 bar and 265 bar, respectively (see Table 4.2).

9.1 Lift-Off Length Evolution

Figure 9.1 shows combined SG and CL images of the combustion events for the 0.75 mm nozzle using 435 bar injection pressure. One case is without PI, while the other three cases feature different PI timings (starting at $t = 1.2$ ms, $t = 2.2$ ms, $t = 3.2$ ms). The experiments use 5 mg diesel fuel pilot injections via the 0.2 mm nozzle followed by a 125 mg ammonia injection with 435 bar after 0.5 ms. In this section, the PI amount is also 5 mg. The spray interaction angle is $\alpha = -7.5^\circ$. The post- or intermediate injection at $t = 1.2$ ms is centered on the ammonia injection. For the PI at $t = 2.2$ ms, EOI ammonia and EOI diesel coincide. The late PI at $t = 3.2$ ms starts after EOI ammonia.

After ignition by the diesel pilot injection, the ammonia flame gradually drifts

9.1 Lift-Off Length Evolution

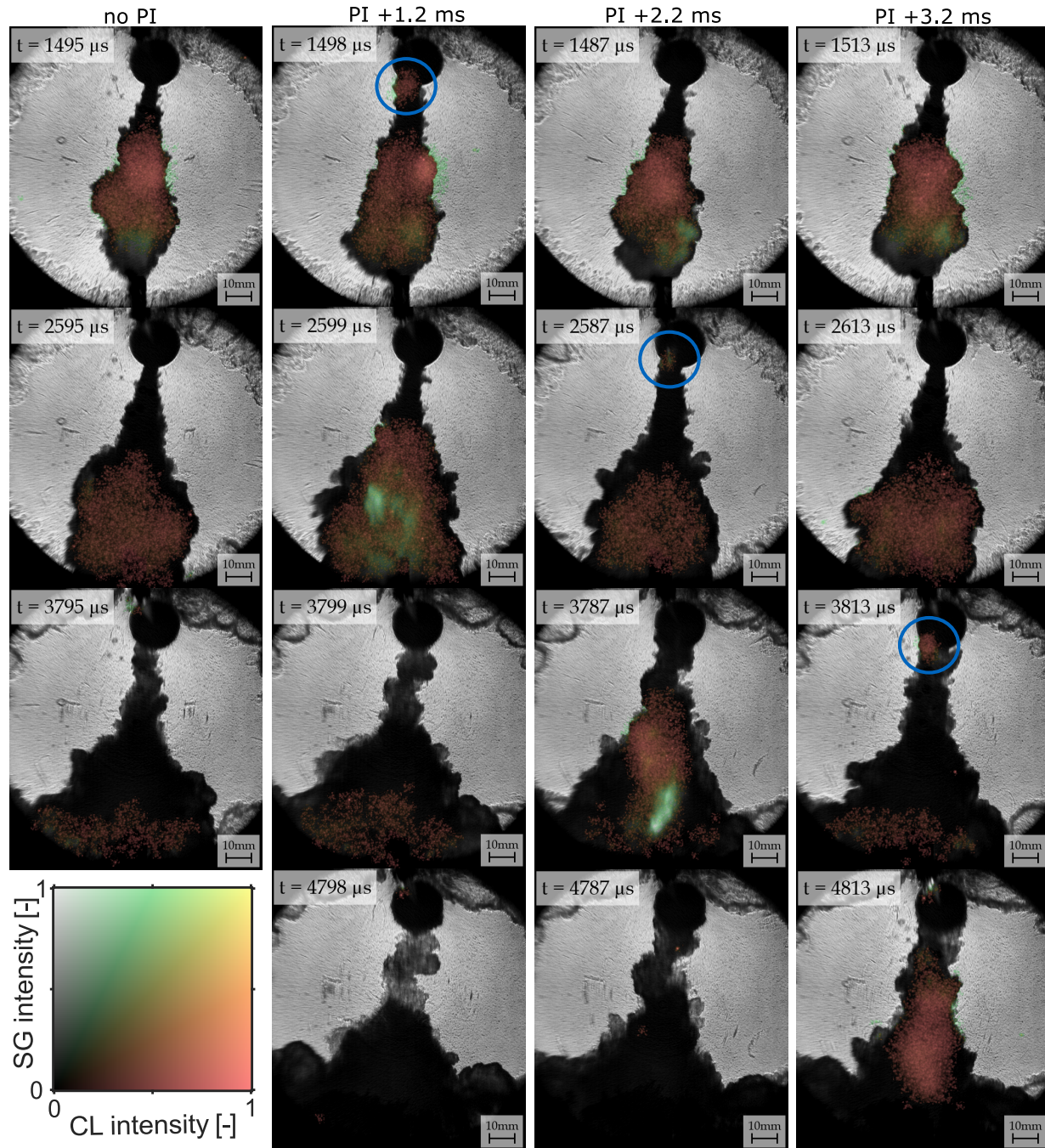


Figure 9.1: Combined SG and CL images of four diesel fuel injection cases with an ammonia injection via the 0.75 mm nozzle. Left: No PI, middle left: PI at $t = 1.2$ ms, middle right: PI at $t = 2.2$ ms, right: PI at $t = 3.2$ ms. Blue circles indicate the first occurrence of OH* CL due to the PI.

off, increasing the lift-off length. Without any PI, this increase continues, even after EOI at $t = 2.7$ ms (see Figure 9.1, left column). The timings of the first three rows shown in Figure 9.1 correspond to the first frames, where OH^* radiation from the three different PI timings is visible ($t = 1.5$ ms for the PI at $t = 1.2$ ms, $t = 2.6$ ms for the PI at $t = 2.2$ ms and $t = 3.8$ ms for the PI at $t = 3.2$ ms). The flame drifts off again after the PI ignites the ammonia spray close to the nozzle. This drift leads to lower flame lift-off lengths during combustion after the PI.

Figure 9.2 shows the HRRs, mass fluxes, and lift-off lengths corresponding to the four combustion cases introduced above. All HRRs show at least two distinct peaks. The first peak results from diesel pilot combustion, while the second, more prominent peak is mainly due to ammonia combustion. In some cases, the combustion due to the diesel PI superimposes this second peak. After each PI, HRRs increase significantly. This effect is particularly strong for the two earlier PI timings, where the interaction with the ammonia spray is stronger and more additional ammonia combustion is induced. The lift-off lengths generally increase in an almost linear manner. During each PI, the lift-off lengths drop before increasing again.

9.2 Ammonia Conversion

This section uses the conversion rates introduced in Section 4.4 to discuss the effect of PIs on ammonia conversion. Figure 9.3 shows averaged ammonia conversion rates for a series of PI timings and a reference case without PI. The error bars indicate the measured ranges of conversion rates. The right part of Figure 9.3 shows the results obtained with the 0.75 mm nozzle, which correspond to the SG and CL images in Figure 9.1 and the HRRs and lift-off lengths in Figure 9.2. The left part shows results obtained with the 0.98 mm nozzle, 265 bar injection pressure, and 125 mg ammonia (see Table 4.2). Three additional PI timings are investigated for the 0.98 mm nozzle. The diesel pilot injection in the reference case without PI is twice as large as the pilot injection in cases with PIs (10 mg) to compare ammonia conversion rates with the same amount of diesel fuel injected. The ammonia conversion rate increases for all

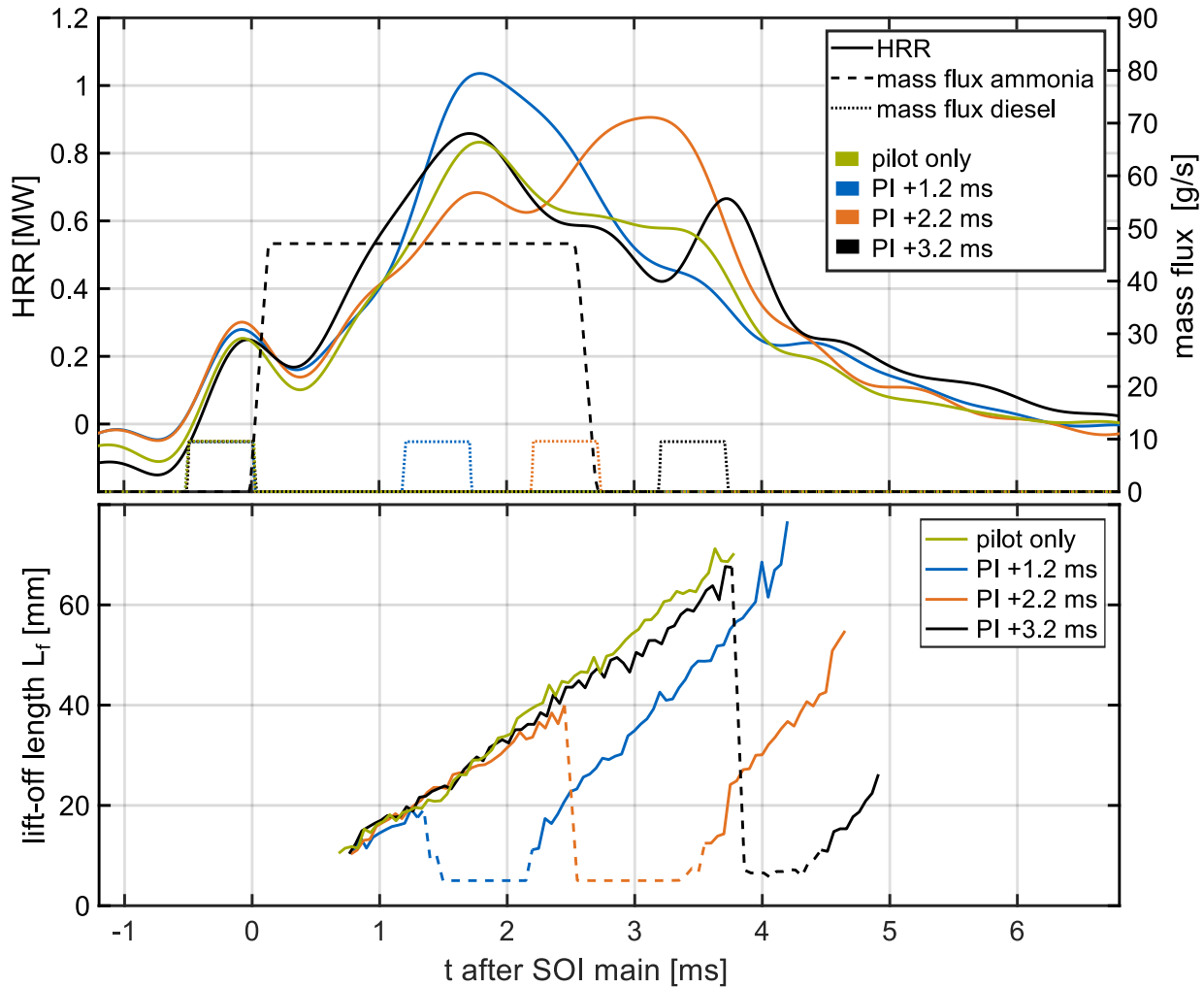


Figure 9.2: HRRs and fuel mass fluxes (top), as well as lift-off lengths (bottom) of four different diesel fuel injection cases with an ammonia main injection via the 0.75 mm nozzle.

PIs investigated compared to the reference case without PI. Early PIs or intermediate injections have a smaller effect on reducing unburned ammonia emissions. For both injection cases, the maximum conversion rates occur for PIs that start at $t = 2.2$ ms and end almost simultaneously with EOI ammonia at $t = 2.7$ ms. For this timing, the ammonia lift-off is reduced close to zero at EOI. For the higher injection pressure case using the 0.75 mm nozzle, a smaller reduction of unburned ammonia is observed for the latest PI timing. This effect results from weaker interaction of the late diesel PI with ammonia due to higher injection pressure and higher spray velocities of the ammonia

spray in this case.

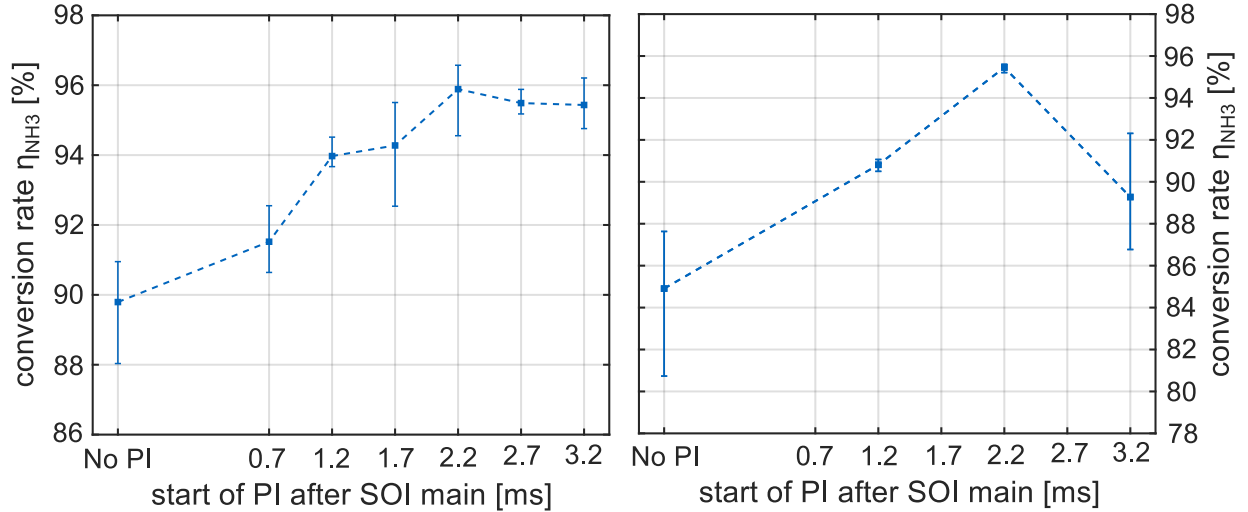


Figure 9.3: Conversion rate of ammonia for different diesel injection cases (left: 0.98 mm nozzle with an injection pressure of 265 bar, right: 0.75 mm nozzle operated with 435 bar). The case without PI features a 10 mg diesel pilot injection, while cases with PI feature a 5 mg diesel pilot followed by a 5 mg PI.

The effect of different PI amounts (3 mg, 5 mg and 10 mg) on ammonia conversion is evaluated in Figure 9.4 for injection case A. The PI timing is constant at $t = 2.2$ ms, which is the most effective (see above). The conversion rates differ only slightly between the cases. Besides the smaller diesel amount, smaller PIs lack momentum, as the needle does not fully open. Therefore, small PIs will not penetrate into the ammonia spray as quickly and thoroughly as larger PIs.

The results suggest that the reduction in unburned ammonia is not only due to additional diesel fuel supporting ammonia combustion, but rather due to the reduction of the ammonia lift-off length. Therefore, PIs that reduce the lift-off length close to zero during EOI ammonia have the strongest impact independent of their size.

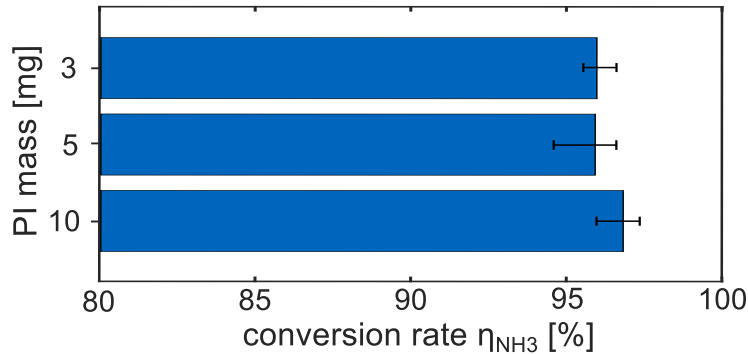


Figure 9.4: Ammonia conversion rates for three different diesel fuel PI amounts (0.98 mm nozzle). The PI starts at $t = 2.2$ ms after SOI ammonia.

9.3 Pollutant Formation

To investigate the effect of PIs on pollutant formation, the injection case with a 5 mg pilot injection followed by a 5 mg diesel PI at $t = 2.2$ ms, which reduce unburned ammonia emissions the most (see Section 9.2), is compared to cases with pilot injections only (5 mg and 10 mg). Figure 9.5 shows the corresponding production rates of NO, NO₂, NO_x, N₂O, as well as HRRs and fuel mass fluxes for the two nozzles examined in this chapter. The HRRs generally rise faster for the larger 10 mg pilot injection. The faster initial rise is due to the larger amount of diesel. In addition, the main peak due to ammonia combustion also occurs earlier. This behavior indicates that the onset of ammonia combustion is facilitated by larger pilot amounts, as already shown in Section 6 for a broader range of pilot injection characteristics. The PIs cause an additional peak in HRR shortly after their injection. Peak HRRs are generally higher and earlier for the 0.75 mm nozzle operated with higher injection pressures, although injection duration and supplied LHV are kept constant. This effect is due to an earlier and more intense interaction of the ammonia spray with diesel combustion products. The ammonia spray injected with a higher injection pressure will penetrate faster, and its interaction with the earlier injected diesel pilot increases. During later combustion phases, when the ammonia flame is significantly lifted from the nozzle, the faster velocity of

the ammonia injected with higher pressure will enable the ammonia to reach the combustion zone earlier, reducing the combustion duration. In addition, increased turbulence and better atomization might facilitate combustion for the higher injection pressure employed with the 0.75 mm nozzle.

NO_x emissions are lower for the 0.75 mm nozzle if no PIs are employed. If PIs are employed, NO_2 emissions increase for both injectors. This increase is more prominent for the 0.75 mm nozzle, where NO_2 emissions rise by a factor of approximately 4. As NO emissions decrease slightly for the cases with PIs, the overall increase in NO_x emissions is small for the 0.98 mm nozzle. In contrast, overall NO_x emissions increase for the 0.75 mm nozzle. PIs do not significantly influence N_2O emissions.

The main mechanism for NO_2 formation in combustion systems is NO oxidation. Adding small quantities of hydrocarbon fuels to NO -containing mixtures at low to intermediate temperatures promotes this conversion [138–140]. Long-chained alkanes are particularly effective in oxidizing NO to NO_2 due to a high rate of production of hydroperoxyl radicals (HO_2) [139, 140]. The PI of diesel in the wake of the ammonia spray can supply the required HO_2 radicals to the NO formed by ammonia combustion. As the PI occurs late, lower charge temperatures during the expansion stroke facilitate the conversion of NO to NO_2 . In addition, the ammonia/air mixture is cooler than the ambient charge temperature due to the high enthalpy of ammonia vaporization.

The additional NO_x formed when using PIs cannot result from diesel combustion, as the 10 mg pilot injection, which burns under higher temperatures closer to TDC, showed less NO_x emissions compared to the case with 5 mg smaller pilot and a 5 mg PI. NO_x emissions mainly form in lean combustion zones for ammonia combustion, as apparent from the $\Phi - T$ maps presented in Section 3.4. Therefore, the additional diesel PI must lead to lean combustion of ammonia or the ammonia/diesel mixture, particularly for the 0.75 mm nozzle. It is well known from low-temperature diesel combustion that mixtures in the wake region lean out rapidly after EOI [59]. Figure 9.6 shows average equivalence ratios in the ammonia spray region upstream of the lift-off length at EOI and the fuel mass in this region. The quantities are obtained using the 1-D spray model presented in Section 5.3. The input parameters used in

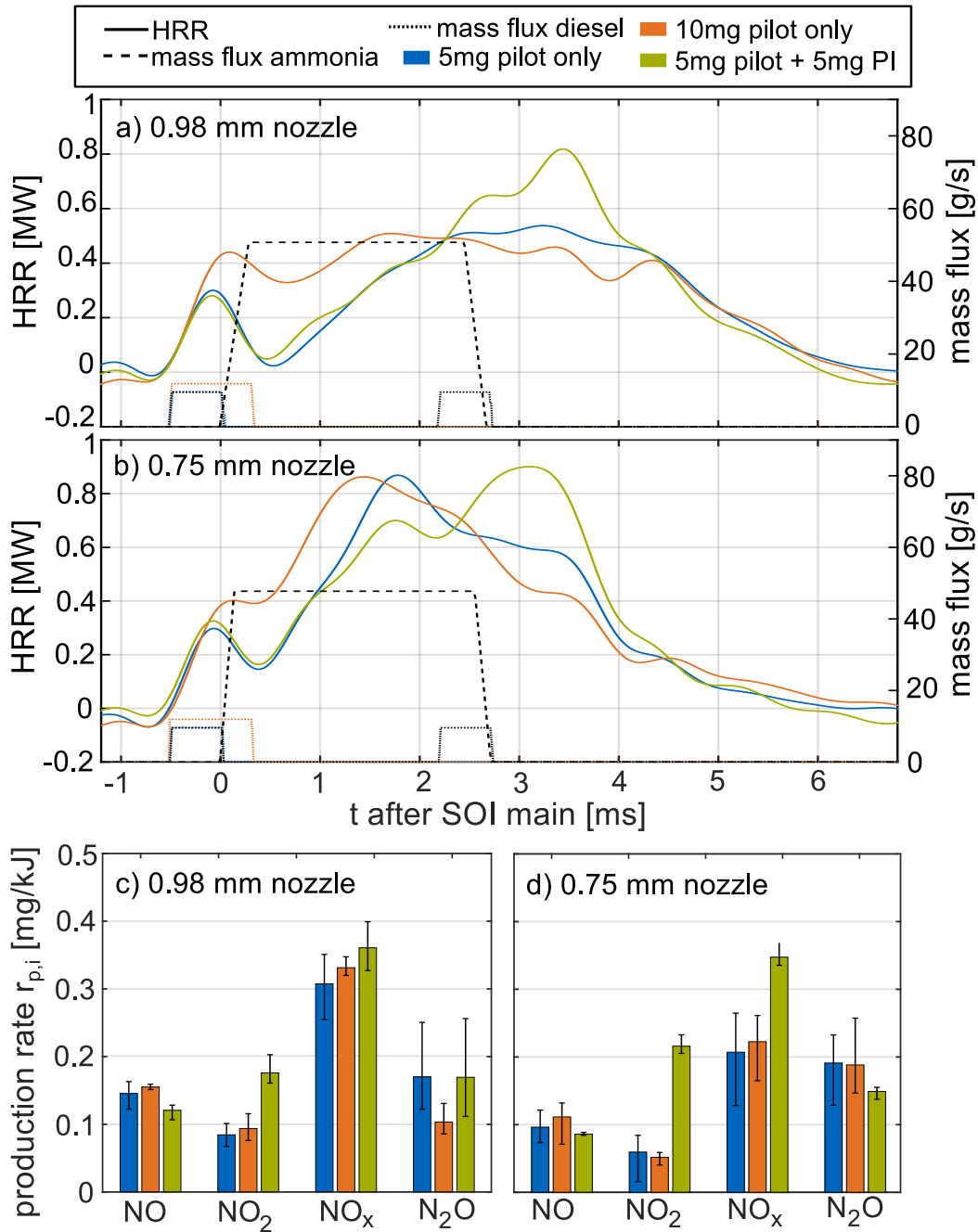


Figure 9.5: Production rates, HRRs, and fuel injection mass fluxes for 5 mg (blue) and 10 mg (orange) pilot injections without PIs, and for a 5 mg pilot injection followed by a 5 mg PI at $t = 2.2$ ms (green). (a): HRRs 0.98 mm nozzle, (b): HRRs 0.75 mm nozzle, (c): production rates 0.98 mm nozzle, (d): production rates 0.75 mm nozzle.

this section are listed in Appendix B. The lift-off length of the injection case using the 0.75 mm nozzle at EOI ammonia is approximately 50 mm (see Figure 9.2), while the reaction zone of the 0.98 mm is only lifted about 40 mm from the nozzle exit at EOI (see Figure 8.3). The absolute ammonia mass in the considered regions is similar for both cases. First, the fuel mass increases as the ammonia spray penetrates into the considered volume. The stationary value (at $t \approx 1$ ms) is initially exceeded due to the jet head vortex. As the injection mass flux ramp-down begins, the fuel mass in the considered volume starts to decrease. Under stationary conditions, the average equivalence ratio in the considered volume is slightly lean for the 0.75 mm nozzle ($\Phi = 0.82$), while it is fuel-rich for the 0.98 mm nozzle ($\Phi = 1.34$). The fuel mixtures become leaner during the injection rate ramp-down. The average mixture is significantly lean for the 0.75 mm nozzle at EOI ammonia ($\Phi = 0.64$), while it is close to stoichiometry for the 0.98 mm nozzle ($\Phi = 0.99$). The diesel PI will mix with the ammonia in the wake region and increase its equivalence ratio. However, the average mixture remains lean, even when adding the entire 5 mg diesel of the PI to the ammonia in the wake region of the 0.75 mm nozzle case.

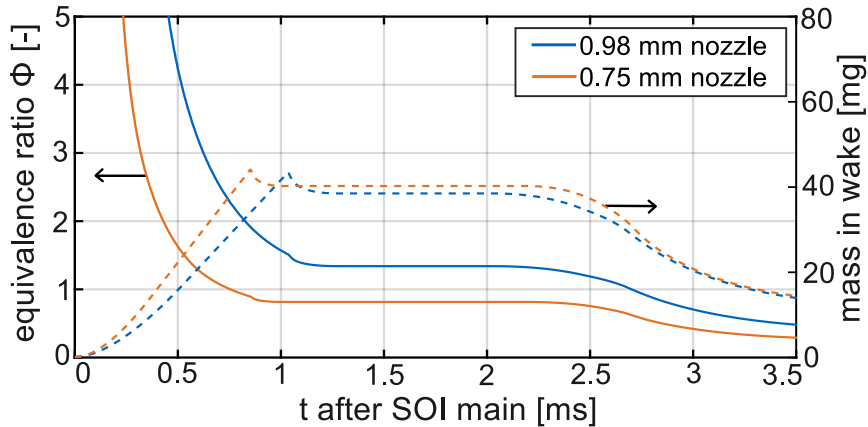


Figure 9.6: Ammonia mass and equivalence ratios over time in the spray volume between nozzle exit and lift-off length at EOI (40 mm for the 0.98 mm nozzle, 50 mm for the 0.75 mm nozzle).

PIs increase the ammonia conversion rate by approximately 10% for the 0.98 mm nozzle, corresponding to 12.5 mg of ammonia. Therefore, a significant fraction of the ammonia in the wake region (30 mg at $t \approx 2.7$ ms) remains unburned if no PIs are employed. If this ammonia is burned addi-

tionally due to PIs, its combustion is lean and causes the observed increase in NO_x emissions. Although pollutant formation depends on the local mixture composition, which is subject to radial and axial gradients in sprays, as well as to turbulent fluctuations, the estimate conducted in this section shows that the potential for additional NO_x formation in the wake region is higher for the injection case using the 0.75 mm nozzle compared to the 0.98 mm nozzle case due to lower average equivalence ratios.

10 Summary and Conclusions

This study investigates the diesel-piloted combustion of ammonia sprays under conditions relevant to internal combustion engines. Using ammonia as engine fuel lowers CO₂ emissions and reduces the climate impact of transportation or power generation. The high-pressure direct injection of ammonia sprays potentially decreases unburned ammonia emissions and increases efficiency compared to other combustion processes. However, the physical properties of ammonia pose considerable challenges for using it as fuel for high-pressure direct injection. Scrutinizing the impact of ammonia's physical properties and combustion chemistry on mixture formation, flame stabilization, and pollutant formation reveals the following key challenges:

- Ammonia/air mixtures are cold and unreactive.
- Flame stabilization is impeded.
- Air pollutants form in fuel-lean conditions already at low temperatures.

However, $\Phi - T$ maps indicate that slightly fuel-rich combustion minimizes air pollutant formation during combustion. Therefore, optimum combustion strategies for ammonia sprays should aim at higher charge temperatures and more fuel-rich conditions compared to conventional fuels.

Initial experiments with single ammonia sprays ignited by diesel pilot injections in a rapid compression-expansion machine (RCEM) confirm the feasibility of the combustion process by analyzing the heat release rates (HRRs). A systematic variation of the temporal and spatial interaction of the ammonia and pilot spray reveals that combustion with high conversion rates requires a strong interaction between pilot fuel and ammonia. However, even at full-load conditions, the pilot fuel's ignition is suppressed if it interacts too

strongly with ammonia before ignition. The adverse effect of part-load conditions is particularly prominent, and misfiring of ammonia occurs at low-load conditions. Varying pilot characteristics strongly impact ammonia combustion, e.g. small pilots delay the heat release of ammonia. The comparison with methane combustion from previous studies under similar conditions by Fink et al. [70, 111] highlights the comparably high importance of ammonia's interaction with the pilot injection.

Spectroscopic investigations unravel the contributions of diesel pilot and ammonia to combustion by revealing the flame's time-resolved spectral footprint. Diesel-related flame emissions disappear before the main share of heat release occurs. Instead, only ammonia-related combustion species (NH_2^* , NH^* , OH^* , NO_2^* , H_2O^*) contribute to the flame emissions during the most intense phase of combustion, which indicates that combustion of residual pilot fuel does not support the ammonia flame. OH^* CL and visible flame emissions, which consist mainly of NH_2^* CL, are identified as suitable flame markers for optical studies investigating ammonia spray combustion.

The optical studies reveal that the ammonia spray flame cannot stabilize at a fixed distance from the nozzle exit under the conditions investigated. Instead, the ammonia lift-off length increases linearly after its ignition by the diesel pilot injection. The drift velocity of the flame only changes slightly with increasing spray velocities, indicating some inertia inhibiting the flame's drift off. A validated mixing limited 1-D spray model yields temperature and equivalence ratio distributions within the examined ammonia sprays. The model reveals that two states within the ammonia spray inhibit flame stabilization by the flame stabilization mechanism observed for diesel sprays, which is the re-entrainment of hot combustion products followed by auto-ignition:

- Close to the nozzle, mixture temperatures are low, owing to the high latent heat of vaporization.
- At larger distances from the nozzle exit, equivalence ratios drop below stoichiometry, and product temperatures decrease.

The lack of a stabilized flame explains the strong dependence of ammo-

nia spray combustion on pilot characteristics and interaction compared to methane. While the flame of more reactive fuels stabilizes at a fixed distance after ignition by the pilot, the ammonia flame drifts downstream starting from the ignition location. Therefore, all later combustion phases depend on the ignition location for ammonia.

The drift off of the flame causes extensive lift-off lengths during later stages of combustion, which creates considerable potential for unburned ammonia emissions. This observation motivates diesel fuel post-injections (PIs) that induce combustion of the ammonia spray's wake region. The PIs reduce unburned ammonia emissions by up to 2/3 independent of their size. Optical imaging and PI parameter variations reveal that the emission reduction results from an induced reduction of the ammonia spray flame's lift-off length during the end of ammonia injection. Therefore, PIs that reduce the lift-off length to zero at the end of ammonia injection show the most significant effect. The 1-D spray model reveals that the wake region is particularly lean, which explains increasing NO_x emissions when using PIs.

In summary, the investigated pilot-ignited high-pressure direct injection combustion of ammonia is feasible. Large heavy-duty engines featuring high combustion temperatures and long residence times are particularly suitable to overcome the presented challenges.

Bibliography

- [1] V. Scharl, T. Sattelmayer, Ignition and combustion characteristics of diesel piloted ammonia injections, *Fuel Communications* 11 (2022) 100068. doi:10.1016/j.jfueco.2022.100068.
- [2] V. Scharl, T. Lackovic, T. Sattelmayer, Characterization of ammonia spray combustion and mixture formation under high-pressure, direct injection conditions, *Fuel* 333 (2023) 126454. doi:10.1016/j.fuel.2022.126454.
- [3] V. Scharl, T. Sattelmayer, Spectroscopic investigation of diesel-piloted ammonia spray combustion, *Fuel* 358 (2024) 130201. doi:10.1016/j.fuel.2023.130201.
- [4] V. Scharl, T. Sattelmayer, Investigation of post-injections for emission reduction of diesel-piloted ammonia spray combustion, in: 30th CIMAC Congress Busan, 2023.
- [5] K. Stenzel, H. Arndt, P. Thorau, V. Scharl, T. Sattelmayer, Ammoniamot - experimental investigations of an ammonia dual-fuel combustion process for decarbonization of the maritime sector, in: The future of large engines, Forschungszentrum für Verbrennungsmotoren und Thermodynamik Rostock GmbH, Rostock, Germany, September 2022.
- [6] D. Krnac, B. Manickam, P. Holand, V. Scharl, T. Sattelmayer, Ammonia-diesel dual-fuel combustion simulation using a tabulated chemistry approach, in: 19th Symposium Sustainable Mobility, Transport and Power Generation, Graz, Austria, 2023.
- [7] C. Baumgarten, Mixture formation in internal combustion engine,

- Springer eBook Collection Engineering, Springer Berlin Heidelberg, Berlin, 2006. doi:10.1007/3-540-30836-9.
- [8] J. Naber, D. L. Siebers, Effects of gas density and vaporization on penetration and dispersion of diesel sprays: Technical paper 960034, in: SAE Technical Paper Series, SAE International, 1996. doi:10.4271/960034.
- [9] J. E. Dec, A conceptual model of DI diesel combustion based on laser-sheet imaging, in: SAE Technical Paper Series, SAE Technical Paper Series, SAE International 400 Commonwealth Drive, Warrendale, PA, United States, 1997. doi:10.4271/970873.
- [10] T. Poinsot, D. Veynante, Theoretical and numerical combustion, 2nd Edition, Edwards, Philadelphia, Pa., 2005.
- [11] L. M. Pickett, S. Kook, H. Persson, Ö. Andersson, Diesel fuel jet lift-off stabilization in the presence of laser-induced plasma ignition, Proceedings of the Combustion Institute 32 (2) (2009) 2793–2800. doi:10.1016/j.proci.2008.06.082.
- [12] P. A. Tipler, Physik: Für Wissenschaftler und Ingenieure, 7th Edition, Springer Link Bücher, Springer Spektrum, Berlin, 2015. doi:10.1007/978-3-642-54166-7.
- [13] A. Gaydon, The spectroscopy of flames, Springer Netherlands, Dordrecht, 1974.
- [14] C. Tornatore, L. Marchitto, P. Sabia, M. de Joannon, Ammonia as green fuel in internal combustion engines: State-of-the-art and future perspectives, Frontiers in Mechanical Engineering 8 (2022). doi:10.3389/fmech.2022.944201.
- [15] F. Mayinger, O. Feldmann (Eds.), Optical Measurements: Techniques and Applications, second corrected and revised edition Edition, Springer eBook Collection, Springer, Berlin and Heidelberg, 2001. doi:10.1007/978-3-642-56443-7.

- [16] M. P. B. Musculus, K. Kattke, Entrainment waves in diesel jets, *SAE International Journal of Engines* 2 (1) (2009) 1170–1193. doi:10.4271/2009-01-1355.
- [17] H. Persson, Ö. Andersson, R. Egnell, Fuel effects on flame lift-off under diesel conditions, *Combustion and Flame* 158 (1) (2011) 91–97. doi:10.1016/j.combustflame.2010.07.020.
- [18] P. Linstrom, Nist chemistry webbook, nist standard reference database 69. doi:10.18434/T4D303.
- [19] S. Verhelst, J. W. G. Turner, L. Sileghem, J. Vancoillie, Methanol as a fuel for internal combustion engines, *Progress in Energy and Combustion Science* 70 (2019) 43–88. doi:10.1016/j.pecs.2018.10.001.
- [20] S. Dasappa, H. Sridhar, G. Sridhar, P. Paul, H. Mukunda, Biomass gasification - a substitute to fossil fuel for heat application, *Biomass and Bioenergy* 25 (6) (2003) 637–649. doi:10.1016/S0961-9534(03)00059-X.
- [21] C. Zamfirescu, I. Dincer, Ammonia as a green fuel and hydrogen source for vehicular applications, *Fuel Processing Technology* 90 (5) (2009) 729–737. doi:10.1016/j.fuproc.2009.02.004.
- [22] IPCS, international programme on Chemical Safety, Chemical safety information from intergovernmental organizations, World Health Organization, Canadian Centre for Occupational Health and Safety. Inter-Organization Programme for the Sound Management of Chemicals, Geneva, Switzerland, 2018.
- [23] B. S. Higgins, C. J. Mueller, D. L. Siebers, Measurements of fuel effects on liquid-phase penetration in di sprays, in: *SAE Technical Paper Series*, SAE International, 1999. doi:10.4271/1999-01-0519.
- [24] Energy Transitions Commission, The first wave. a blueprint for commercial-scale zero-emission shipping pilots: A special report by the energy transitions commission for the getting to zero coalition (2020).

- [25] International Energy Agency - IEA, The future of hydrogen: technology report (2019).
URL <https://www.iea.org/reports/the-future-of-hydrogen>
- [26] A. Valera-Medina, F. Amer-Hatem, A. K. Azad, I. C. Dedoussi, M. de Joannon, R. X. Fernandes, P. Glarborg, H. Hashemi, X. He, S. Mashruk, J. McGowan, C. Mounaim-Rouselle, A. Ortiz-Prado, A. Ortiz-Valera, I. Rossetti, B. Shu, M. Yehia, H. Xiao, M. Costa, Review on ammonia as a potential fuel: From synthesis to economics, *Energy & Fuels* 9 (35) (2021) 6964–7029. doi:10.1021/acs.energyfuels.0c03685.
- [27] Nick Ash and Tim Scarbrough, Sailing on solar (2019).
- [28] American Bureau of Shipping, Ammonia as marine fuel: sustainability whitepaper.
URL <https://absinfo.eagle.org/acton/media/16130/sustainability-whitepaper-ammonia-as-marine-fuel>
- [29] A. Sánchez, E. Castellano, M. Martín, P. Vega, Evaluating ammonia as green fuel for power generation: A thermo-chemical perspective, *Applied Energy* 293 (2021) 116956. doi:10.1016/j.apenergy.2021.116956.
- [30] J. S. Cardoso, V. Silva, R. C. Rocha, M. J. Hall, M. Costa, D. Eusébio, Ammonia as an energy vector: Current and future prospects for low-carbon fuel applications in internal combustion engines, *Journal of Cleaner Production* 296 (2021) 126562. doi:10.1016/j.jclepro.2021.126562.
- [31] G. Vesper, Taking the pressure off, *Nature Energy* 3 (12) (2018) 1025–1026. doi:10.1038/s41560-018-0293-y.
- [32] J. T. Gray, E. Dimitroff, N. T. Meckel, R. D. Quillian, Ammonia fuel - engine compatibility and combustion: Technical paper 660156, in: SAE Technical Paper Series, Vol. 75, SAE International, 1966, pp. 660002–660164. doi:10.4271/660156.
- [33] K. Bro, P. S. Pedersen, Alternative diesel engine fuels: An experimental investigation of methanol, ethanol, methane and ammonia in a DI diesel

- engine with pilot injection: Technical paper 770794, in: SAE Technical Paper Series, SAE International, 1977. doi:10.4271/770794.
- [34] E. S. Starkman, G. E. James, H. K. Newhall, Ammonia as a diesel engine fuel: Theory and application: Technical paper 670946, SAE Transactions (1968) 3193–3212, <http://www.jstor.org/stable/44562852>.
- [35] M.-C. Chiong, C. T. Chong, J.-H. Ng, S. Mashruk, W. W. F. Chong, N. A. Samiran, G. R. Mong, A. Valera-Medina, Advancements of combustion technologies in the ammonia-fuelled engines, *Energy Conversion and Management* 244 (2021) 114460. doi:10.1016/j.enconman.2021.114460.
- [36] K. B. Hodgins, P. G. Hill, P. Ouellette, P. Hung, Directly injected natural gas fueling of diesel engines, in: SAE Technical Paper Series, SAE International, 1996. doi:10.4271/961671.
- [37] G. P. McTaggart-Cowan, W. K. Bushe, S. N. Rogak, P. G. Hill, S. R. Munshi, Injection parameter effects on a direct injected, pilot ignited, heavy duty natural gas engine with EGR, in: SAE Technical Paper Series, SAE International, 2003. doi:10.4271/2003-01-3089.
- [38] Y. Wang, H. Wang, X. Meng, J. Tian, Y. Wang, W. Long, S. Li, Combustion characteristics of high pressure direct-injected methanol ignited by diesel in a constant volume combustion chamber, *Fuel* 254 (2019) 115598. doi:10.1016/j.fuel.2019.06.006.
- [39] Y. Dong, O. Kaario, G. Hassan, O. Ranta, M. Larmi, B. Johansson, High-pressure direct injection of methanol and pilot diesel: A non-premixed dual-fuel engine concept, *Fuel* 277 (2020) 117932. doi:10.1016/j.fuel.2020.117932.
- [40] M. Saccullo, T. Benham, I. Denbratt, Dual fuel methanol and diesel direct injection hd single cylinder engine tests, in: SAE Technical Paper Series, SAE International, 2018. doi:10.4271/2018-01-0259.
- [41] G. P. Merker, *Grundlagen Verbrennungsmotoren: Funktionsweise und Alternative Antriebssysteme Verbrennung, Messtechnik und Simulation*,

- 9th Edition, ATZ/MTZ-Fachbuch Ser, Springer Fachmedien Wiesbaden GmbH, Wiesbaden, 2019.
URL <https://ebookcentral.proquest.com/lib/kxp/detail.action?docID=5724728>
- [42] K. Mollenhauer, H. Tschöke, Handbuch Dieselmotoren, 3rd Edition, Springer eBook Collection, Springer Berlin Heidelberg, Berlin, 2007. doi:10.1007/978-3-540-72165-9.
- [43] A. H. Lefebvre, V. G. McDonell, Atomization and sprays, second edition Edition, Combustion, Taylor & Francis CRC Press, Boca Raton, 2017. doi:10.1201/9781315120911.
- [44] J. S. Turner, The ‘starting plume’ in neutral surroundings, Journal of Fluid Mechanics 13 (3) (1962) 356–368. doi:10.1017/S0022112062000762.
- [45] S. S. Sazhin, G. Feng, M. R. Heikal, A model for fuel spray penetration, Fuel 80 (15) (2001) 2171–2180. doi:10.1016/S0016-2361(01)00098-9.
- [46] Y. Wakuri, M. Fujii, T. Amitani, R. Tsuneya, Studies on the penetration of fuel spray in a diesel engine, Bulletin of JSME 3 (9) (1960) 123–130. doi:10.1299/jsme1958.3.123.
- [47] H. Hiroyasu, M. Arai, Structures of fuel sprays in diesel engines, SAE Transactions (Vol. 99) (1990) 1050–1061. doi:10.4271/900475.
- [48] D. L. Siebers, Liquid-phase fuel penetration in diesel sprays, SAE Transactions, Journal of Engines (107) (1998) 1205–1227. doi:10.4271/980809.
- [49] D. B. Spalding, Some fundamentals of combustion, Butterworths Scientific Publications, New York: Academic Press, London, 1955.
- [50] A. Doudou, Turbulent flow study of an isothermal diesel spray injected by a common rail system, Fuel 84 (2-3) (2005) 287–298. doi:10.1016/j.fuel.2004.06.032.

- [51] J. Pastor, J. Javierlopez, J. Garcia, A 1D model for the description of mixing-controlled inert diesel sprays, *Fuel* 87 (13-14) (2008) 2871–2885. doi:10.1016/j.fuel.2008.04.017.
- [52] L. M. Pickett, J. Manin, C. L. Genzale, D. L. Siebers, M. P. B. Musculus, C. A. Idicheria, Relationship between diesel fuel spray vapor penetration/dispersion and local fuel mixture fraction, *SAE International Journal of Engines* 4 (1) (2011) 764–799. doi:10.4271/2011-01-0686.
- [53] C. A. Idicheria, L. M. Pickett, Formaldehyde visualization near lift-off location in a diesel jet, in: *SAE Technical Paper Series*, SAE Technical Paper Series, SAE International 400 Commonwealth Drive, Warrendale, PA, United States, 2006. doi:10.4271/2006-01-3434.
- [54] G. Bruneaux, Combustion structure of free and wall-impinging diesel jets by simultaneous laser-induced fluorescence of formaldehyde, polyaromatic hydrocarbons, and hydroxides, *International Journal of Engine Research* 9 (3) (2008) 249–265. doi:10.1243/14680874JER00108.
- [55] H. Kosaka, T. Aizawa, T. Kamimoto, Two-dimensional imaging of ignition and soot formation processes in a diesel flame, *International Journal of Engine Research* 6 (1) (2005) 21–42. doi:10.1243/146808705X7347.
- [56] M. P. Musculus, P. C. Miles, L. M. Pickett, Conceptual models for partially premixed low-temperature diesel combustion, *Progress in Energy and Combustion Science* 39 (2-3) (2013) 246–283. doi:10.1016/j.pecs.2012.09.001.
- [57] J. Heywood, *Internal combustion engine fundamentals*, 2nd Edition, McGraw-Hill Education and McGraw Hill, New York, N.Y., 2019.
- [58] L. M. Pickett, D. L. Siebers, Soot in diesel fuel jets: effects of ambient temperature, ambient density, and injection pressure, *Combustion and Flame* 138 (1-2) (2004) 114–135. doi:10.1016/j.combustflame.2004.04.006.
- [59] M. P. B. Musculus, T. Lachaux, L. M. Pickett, C. A. Idicheria, End-of-injection over-mixing and unburned hydrocarbon emissions in low-temperature-combustion diesel engines: Technical paper 2007-01-0907,

- in: SAE Technical Paper Series, SAE International, 2007. doi:10.4271/2007-01-0907.
- [60] A. M. Rothrock, C. D. Waldron, Effect of nozzle design on fuel spray and flame formation in a high-speed compression-ignition engine: Report no.: Naca-tr-561.
- [61] D. L. Siebers, B. Higgins, Flame lift-off on direct-injection diesel sprays under quiescent conditions, in: SAE Technical Paper Series, SAE International, 2001. doi:10.4271/2001-01-0530.
- [62] B. Higgins, D. L. Siebers, Measurement of the flame lift-off location on DI diesel sprays using OH chemiluminescence, in: SAE Technical Paper Series, SAE International, 2001. doi:10.4271/2001-01-0918.
- [63] D. L. Siebers, B. Higgins, L. Pickett, Flame lift-off on direct-injection diesel fuel jets: Oxygen concentration effects, in: SAE Technical Paper Series, SAE International, 2002. doi:10.4271/2002-01-0890.
- [64] F. Tagliante-Saracino, Combined study by direct numerical simulation and optical diagnostics of the flame stabilization in a diesel spray, Dissertation, Université Paris-Saclay, Paris (2019).
- [65] L. M. Pickett, D. L. Siebers, C. A. Idicheria, Relationship between ignition processes and the lift-off length of diesel fuel jets, in: SAE Technical Paper Series, SAE International, 2005. doi:10.4271/2005-01-3843.
- [66] R. Venugopal, J. Abraham, A review of fundamental studies relevant to flame lift-off in diesel jets, SAE Transactions 2007 (116) 132–151.
URL <https://www.jstor.org/stable/44699269>
- [67] K. K. Kuo, Principles of combustion, second edition Edition, John Wiley & Sons Inc, Hoboken, New Jersey, 2005.
- [68] K. M. Lyons, Toward an understanding of the stabilization mechanisms of lifted turbulent jet flames: Experiments, Progress in Energy and Combustion Science 33 (2) (2007) 211–231. doi:10.1016/j.pecs.2006.11.001.

- [69] G. R. Ruetsch, L. Vervisch, A. Liñán, Effects of heat release on triple flames, *Physics of Fluids* 7 (6) (1995) 1447–1454. doi:10.1063/1.868531.
- [70] G. Fink, M. Jud, T. Sattelmayer, Fundamental study of diesel-piloted natural gas direct injection under different operating conditions, *Journal of Engineering for Gas Turbines and Power* 141 (9) (2019). doi:10.1115/1.4043643.
- [71] P. Rorimpandey, H. L. Yip, A. Srna, G. Zhai, A. Wehrfritz, S. Kook, E. R. Hawkes, Q. N. Chan, Hydrogen-diesel dual-fuel direct-injection (H2DDI) combustion under compression-ignition engine conditions, *International Journal of Hydrogen Energy* 48 (2) (2023) 766–783. doi:10.1016/j.ijhydene.2022.09.241.
- [72] H. L. Yip, A. Srna, G. Zhai, A. Wehrfritz, S. Kook, E. R. Hawkes, Q. N. Chan, Laser-induced plasma-ignited hydrogen jet combustion in engine-relevant conditions, *International Journal of Hydrogen Energy* 48 (4) (2023) 1568–1581. doi:10.1016/j.ijhydene.2022.09.296.
- [73] F. Tagliante, T. Poinso, L. M. Pickett, P. Pepiot, L.-M. Malbec, G. Bruneaux, C. Angelberger, A conceptual model of the flame stabilization mechanisms for a lifted diesel-type flame based on direct numerical simulation and experiments, *Combustion and Flame* 201 (2019) 65–77. doi:10.1016/j.combustflame.2018.12.007.
- [74] C. Chartier, U. Aronsson, Ö. Andersson, R. Egnell, B. Johansson, Influence of jet–jet interactions on the lift-off length in an optical heavy-duty diesel engine, *Fuel* 112 (2013) 311–318. doi:10.1016/j.fuel.2013.05.021.
- [75] M. Lundgren, A. Matamis, Z. Wang, P. Garcia Valladolid, M. Richter, O. Andersson, A. Andersson, Lift-off lengths in an optical heavy-duty engine operated at high load with low and high octane number fuels, in: *SAE Technical Paper Series*, SAE International, 2018. doi:10.4271/2018-01-0245.

- [76] K. Akihama, Y. Takatori, K. Inagaki, S. Sasaki, A. M. Dean, Mechanism of the smokeless rich diesel combustion by reducing temperature: Sae technical paper 2001-01-0655, in: SAE Technical Paper Series, SAE International, 2001. doi:10.4271/2001-01-0655.
- [77] T. Kitamura, T. Ito, J. Senda, H. Fujimoto, Mechanism of smokeless diesel combustion with oxygenated fuels based on the dependence of the equivalence ration and temperature on soot particle formation, International Journal of Engine Research 3 (4) (2002) 223–248. doi:10.1243/146808702762230923.
- [78] F. Tao, R. Reitz, D. Foster, Revisit of diesel reference fuel (n-heptane) mechanism applied to multidimensional diesel ignition and combustion simulations, Seventeenth International Multidimensional Engine Modeling User's Group Meeting at the SAE Congress, Detroit, Michigan (2007).
- [79] A. Egerton, The ammonia flame, Nature 89 (1912) 270. doi:10.1038/089270a0.
- [80] T. Fiala, Radiation from high pressure hydrogen-oxygen flames and its use in assessing rocket combustion instability, Dissertation, Technical University of Munich, Munich, Germany (2015-03-17).
- [81] M. Lauer, T. Sattelmayer, On the adequacy of chemiluminescence as a measure for heat release in turbulent flames with mixture gradients, Journal of Engineering for Gas Turbines and Power 132 (6) (2010). doi:10.1115/1.4000126.
- [82] J. Ballester, T. García-Armingol, Diagnostic techniques for the monitoring and control of practical flames, Progress in Energy and Combustion Science 36 (4) (2010) 375–411. doi:10.1016/j.pecs.2009.11.005.
- [83] H. Fujimoto, K. Kurata, G. Asai, J. Senda, OH radical generation and soot formation/oxidation in DI diesel engine, in: SAE Technical Paper Series, SAE International, 1998. doi:10.4271/982630.
- [84] J. V. Pastor, J. M. García-Oliver, A. García, C. Micó, R. Durrett, A spectroscopy study of gasoline partially premixed compression ignition

- spark assisted combustion, *Applied Energy* 104 (2013) 568–575. doi:10.1016/j.apenergy.2012.11.030.
- [85] A. Srna, R. Bombach, K. Herrmann, G. Bruneaux, Characterization of the spectral signature of dual-fuel combustion luminosity: implications for evaluation of natural luminosity imaging, *Applied Physics B* 125 (7) (2019). doi:10.1007/s00340-019-7222-z.
- [86] E. Mancaruso, B. M. Vaglieco, Spectroscopic measurements of premixed combustion in diesel engine, *Fuel* 90 (2) (2011) 511–520. doi:10.1016/j.fuel.2010.09.052.
- [87] N. Wang, T. Li, X. Zhou, Z. Zhang, R. Chen, S. Li, High-pressure spray and combustion characteristics of ammonia jets under diesel-like conditions, *The Proceedings of the International symposium on diagnostics and modeling of combustion in internal combustion engines* 2022.10 (0) (2022) B7–1. doi:10.1299/jmsesdm.2022.10.B7-1.
- [88] S. Wüthrich, P. Cartier, P. Süess, B. Schneider, P. Obrecht, K. Herrmann, Optical investigation and thermodynamic analysis of premixed ammonia dual-fuel combustion initiated by dodecane pilot fuel, *Fuel Communications* 12 (2022) 100074. doi:10.1016/j.jfueco.2022.100074.
- [89] X. Zhu, A. A. Khateeb, W. L. Roberts, T. F. Guiberti, Chemiluminescence signature of premixed ammonia-methane-air flames, *Combustion and Flame* 231 (2021) 111508. doi:10.1016/j.combustflame.2021.111508.
- [90] S. Mashruk, M. O. Viguera-Zuniga, M. E. Tejada-del Cueto, H. Xiao, C. Yu, U. Maas, A. Valera-Medina, Combustion features of CH₄/NH₃/H₂ ternary blends, *International Journal of Hydrogen Energy* 47 (70) (2022) 30315–30327. doi:10.1016/j.ijhydene.2022.03.254.
- [91] Y. Ichikawa, Y. Niki, K. Takasaki, H. Kobayashi, A. Miyanagi, Experimental study of combustion process of NH₃ stratified spray using imaging methods for NH₃ fueled large two-stroke marine engine,

- Applications in Energy and Combustion Science 13 (2023) 100119. doi:10.1016/j.jaecs.2023.100119.
- [92] M. Saccullo, A. Nygren, T. Benham, I. Denbratt, Alcohol flexible hd single cylinder diesel engine tests with separate dual high pressure direct fuel injection, Fuel 294 (2021) 120478. doi:10.1016/j.fuel.2021.120478.
- [93] T. Stocker, L. Alexander, M. Allen (Eds.), Climate change 2013: The physical science basis ; Working Group I contribution to the fifth assessment report of the Intergovernmental Panel on Climate Change, WMO IPCC, Geneva, 2014. doi:10.1017/CB09781107415324.
- [94] Y. Fang, K. Zhang, X. Ma, Y. Zhang, L. Xu, Y. Li, S. Shuai, Droplet measurement of high-pressure liquid ammonia injection using PDPA, in: Y. Fang, K. Zhang, X. Ma, Y. Zhang, L. Xu, Y. Li, S. Shuai (Eds.), SAE Technical Paper Series, SAE International, 2023. doi:10.4271/2023-01-1637.
- [95] P. Glarborg, J. A. Miller, B. Rusic, S. J. Klippenstein, Modeling nitrogen chemistry in combustion, Progress in Energy and Combustion Science (67) (2018) 31–68. doi:10.1016/j.pecs.2018.01.002.
- [96] H. Kobayashi, A. Hayakawa, K. K. A. Somarathne, E. C. Okafor, Science and technology of ammonia combustion, Proceedings of the Combustion Institute 37 (1) (2019) 109–133. doi:10.1016/j.proci.2018.09.029.
- [97] L. Yu, W. Zhou, Y. Feng, W. Wang, J. Zhu, Y. Qian, X. Lu, The effect of ammonia addition on the low-temperature autoignition of n-heptane: An experimental and modeling study, Combustion and Flame 217 (2020) 4–11. doi:10.1016/j.combustflame.2020.03.019.
- [98] Y. Song, H. Hashemi, J. M. Christensen, C. Zou, P. Marshall, P. Glarborg, Ammonia oxidation at high pressure and intermediate temperatures, Fuel 181 (2016) 358–365. doi:10.1016/j.fuel.2016.04.100.
- [99] R. K. Lyon, D. Benn, Kinetics of the NO-NH₃-O₂ reaction, Symposium (International) on Combustion 17 (1) (1979) 601–610. doi:10.1016/S0082-0784(79)80060-0.

- [100] J. Miller, M. Branch, R. Kee, A chemical kinetic model for the selective reduction of nitric oxide by ammonia, *Combustion and Flame* 43 (1981) 81–98. doi:10.1016/0010-2180(81)90008-0.
- [101] S. J. Klippenstein, L. B. Harding, P. Glarborg, J. A. Miller, The role of NNH in NO formation and control, *Combustion and Flame* 158 (4) (2011) 774–789. doi:10.1016/j.combustflame.2010.12.013.
- [102] J. A. Miller, P. Glarborg, Modelling the formation of N₂O and NO₂ in the thermal De-NO_x process, in: V. I. Goidanskii, F. P. Schäfer, J. P. Toennies, H. K. V. Lotsch, J. Wolfrum, H.-R. Volpp, R. Rannacher, J. Warnatz (Eds.), *Gas Phase Chemical Reaction Systems*, Vol. 61 of Springer Series in Chemical Physics, Springer Berlin Heidelberg, Berlin, Heidelberg, 1996, pp. 318–333. doi:10.1007/978-3-642-80299-7_25.
- [103] E. C. Okafor, K. K. A. Somarathne, R. Ratthanan, A. Hayakawa, T. Kudo, O. Kurata, N. Iki, T. Tsujimura, H. Furutani, H. Kobayashi, Control of NO_x and other emissions in micro gas turbine combustors fuelled with mixtures of methane and ammonia, *Combustion and Flame* 211 (2020) 406–416. doi:10.1016/j.combustflame.2019.10.012.
- [104] E. C. Okafor, H. Yamashita, A. Hayakawa, K. K. A. Somarathne, T. Kudo, T. Tsujimura, M. Uchida, S. Ito, H. Kobayashi, Flame stability and emissions characteristics of liquid ammonia spray co-fired with methane in a single stage swirl combustor, *Fuel* 287 (2021) 119433. doi:10.1016/j.fuel.2020.119433.
- [105] D. L. Siebers, Scaling liquid-phase fuel penetration in diesel sprays based on mixing-limited vaporization: Technical paper 1999-01-0528, in: SAE Technical Paper Series, SAE International, 1999. doi:10.4271/1999-01-0528.
- [106] Y. Zhang, L. Xu, Y. Zhu, S. Xu, X.-S. Bai, Numerical study on liquid ammonia direct injection spray characteristics under engine-relevant conditions, *Applied Energy* 334 (2023) 120680. doi:10.1016/j.apenergy.2023.120680.

- [107] R. Pelé, C. Mounaïm-Rousselle, P. Bréquigny, C. Hespel, J. Bellettre, First study on ammonia spray characteristics with a current GDI engine injector (2021).
URL <https://www.mdpi.com/2673-3994/2/3/15>
- [108] K. A. Pedersen, M. T. Lewandowski, C. Schulze-Netzer, M. Pasternak, T. Løvås, Ammonia in dual-fueled internal combustion engines: Impact on NO_x, N₂O, and soot formation, *Energy & Fuels* (2023). doi:10.1021/acs.energyfuels.3c02549.
- [109] National Research Council, Acute exposure guideline levels for selected airborne chemicals, 6th Edition, National Academies Press, Washington, DC, 2008. doi:10.17226/12018.
- [110] F. Dorer, P. Prechtel, F. Mayinger, Investigation of mixture formation and combustion processes in a hydrogen fueled diesel engine, in: T. O. Saetre (Ed.), *Hydrogen Power: Theoretical and Engineering Solutions*, Springer Netherlands, Dordrecht, 1998, pp. 49–54. doi:10.1007/978-94-015-9054-9_6.
- [111] G. Fink, M. Jud, T. Sattelmayer, Influence of the spatial and temporal interaction between diesel pilot and directly injected natural gas jet on ignition and combustion characteristics, *Journal of Engineering for Gas Turbines and Power* 140 (10) (2018). doi:10.1115/1.4039934.
- [112] D. Lee, S. Hochgreb, Rapid compression machines: Heat transfer and suppression of corner vortex, *Combustion and Flame* 114 (3-4) (1998) 531–545. doi:10.1016/S0010-2180(97)00327-1.
- [113] M. Coppo, C. Negri, N. Wermuth, J. Garcia-Oliver, Powering a greener future: the OMT injector enables high-pressure injection of ammonia and methanol, in: 30th CIMAC Congress Busan, 2023.
- [114] J. Gaucherand, C. Netzer, M. T. Lewandowski, T. Løvås, Modelling of liquid injection of ammonia in a direct injector using reynolds-averaged navier–stokes simulation, in: *Proceedings of the 63rd International Conference of Scandinavian Simulation Society, SIMS 2022*, Trondheim,

- Norway, September 20-21, 2022, Linköping Electronic Conference Proceedings, Linköping University Electronic Press, 2022, pp. 405–412. doi:10.3384/ecp192058.
- [115] G. Fink, Experimental investigation of ignition and combustion of diesel-piloted natural gas jets in a rapid compression-expansion machine, Phd thesis, Technical University of Munich, Munich, Germany (2021).
- [116] K. H. Ryu, G. Zacharakis-Jutz, S.-C. Kong, Effects of fuel compositions on diesel engine performance using ammonia-DME mixtures, in: SAE Technical Paper Series, SAE International, 2013. doi:10.4271/2013-01-1133.
- [117] A. Arnold, F. Dinkelacker, T. Heitzmann, P. Monkhouse, M. Schäfer, V. Sick, J. Wolfrum, W. Hentschel, K.-P. Schindler, DI diesel engine combustion visualized by combined laser techniques, Symposium (International) on Combustion 24 (1) (1992) 1605–1612. doi:10.1016/S0082-0784(06)80187-6.
- [118] R. E. Canaan, J. E. Dec, R. M. Green, D. T. Daly, The influence of fuel volatility on the liquid-phase fuel penetration in a heavy-duty DI diesel engine, in: SAE Technical Paper Series, SAE International, 1998. doi:10.4271/980510.
- [119] C. Arcoumanis, M. Gavaises, B. French, Effect of fuel injection processes on the structure of diesel sprays, in: SAE Technical Paper Series, SAE International, 1997. doi:10.4271/970799.
- [120] M. Jud, G. Fink, T. Sattelmayer, Predicting ignition and combustion of a pilot ignited natural gas jet using numerical simulation based on detailed chemistry, in: Proceedings of the ASME Internal Combustion Engine Fall Technical Conference - 2017, The American Society of Mechanical Engineers, New York, N.Y., 2017. doi:10.1115/ICEF2017-3533.
- [121] M. Jud, C. Wieland, G. Fink, T. Sattelmayer, Numerical analysis of the combustion process in dual-fuel engines with direct injection of natural gas, in: Proceedings of the ASME Internal Combustion Engine Fall

- Technical Conference - 2018, The American Society of Mechanical Engineers, New York, N.Y., 2019. doi:10.1115/ICEF2018-9579.
- [122] R. Payri, F. J. Salvador, J. Gimeno, L. D. Zapata, Diesel nozzle geometry influence on spray liquid-phase fuel penetration in evaporative conditions, *Fuel* 87 (7) (2008) 1165–1176. doi:10.1016/j.fuel.2007.05.058.
- [123] W. Weng, M. Aldén, Z. Li, Visible chemiluminescence of ammonia premixed flames and its application for flame diagnostics, *Proceedings of the Combustion Institute* 39 (4) (2023) 4327–4334. doi:10.1016/j.proci.2022.08.012.
- [124] G. N. Abramovich, L. Schindel, *The theory of turbulent jets: Chapter 5: jet of an incompressible fluid in a coflowing external stream*, MIT Press, Cambridge, Mass., 1963.
- [125] W. Rizk, Experimental studies of the mixing processes and flow configurations in two-cycle engine scavenging, *Proceedings of the Institution of Mechanical Engineers* 172 (1) (1958) 417–437. doi:10.1243/PIME_PROC_1958_172_037_02.
- [126] R. D. Reitz, F. V. BRacco, Ultra-high-speed filming of atomizing jets, *Physics of Fluids* 22 (6) (1979) 1054. doi:10.1063/1.862711.
- [127] S. L. Sheehe, S. I. Jackson, Identification of species from visible and near-infrared spectral emission of a nitromethane-air diffusion flame, *Journal of Molecular Spectroscopy* 364 (2019) 111185. doi:10.1016/j.jms.2019.111185.
- [128] A. Fontijn, C. B. Meyer, H. I. Schiff, Absolute quantum yield measurements of the NO–O reaction and its use as a standard for chemiluminescent reactions, *The Journal of Chemical Physics* 40 (1) (1964) 64–70. doi:10.1063/1.1724895.
- [129] E. Mancaruso, B. M. Vaglieco, Spectroscopic analysis of the phases of premixed combustion in a compression ignition engine fuelled with diesel and ethanol, *Applied Energy* 143 (2015) 164–175. doi:10.1016/j.apenergy.2015.01.031.

- [130] R. Augusta, D. E. Foster, J. B. Gandhi, J. Eng, P. M. Najt, Chemiluminescence measurements of homogeneous charge compression ignition HCCI combustion, in: SAE Technical Paper Series, SAE International, 2006. doi:10.4271/2006-01-1520.
- [131] J. A. Miller, C. T. Bowman, Mechanism and modeling of nitrogen chemistry in combustion, *Progress in Energy and Combustion Science* 15 (4) (1989) 287–338. doi:10.1016/0360-1285(89)90017-8.
- [132] C. Espey, J. E. Dec, The effect of TDC temperature and density on the liquid-phase fuel penetration in a DI diesel engine, in: SAE Technical Paper Series, SAE International, 1995. doi:10.4271/952456.
- [133] L. M. Pickett, S. Kook, H. Persson, Ö. Andersson, Diesel fuel jet lift-off stabilization in the presence of laser-induced plasma ignition, *Proceedings of the Combustion Institute* 32 (2) (2009) 2793–2800. doi:10.1016/j.proci.2008.06.082.
- [134] Statustagung Maritime Technologien: Tagungsband der Statustagung 2018, Vol. 11 of Schriftenreihe Projektträger Jülich, Forschungszentrum Jülich GmbH Zentralbibliothek Verlag, Jülich, 2018.
- [135] B. W. Knox, C. L. Genzale, L. M. Pickett, J. M. Garcia-Oliver, W. Vera-Tudela, Combustion recession after end of injection in diesel sprays, *SAE International Journal of Engines* 8 (2) (2015) 679–695. doi:10.4271/2015-01-0797.
- [136] Y. Ichikawa, Y. Niki, K. Takasaki, H. Kobayashi, A. Miyanagi, NH₃ combustion using three-layer stratified fuel injection for a large two-stroke marine engine: Experimental verification of the concept, *Applications in Energy and Combustion Science* 10 (2022) 100071. doi:10.1016/j.jaecs.2022.100071.
- [137] R. Payri, J. Gimeno, M. Carreres, T. Montiel, Understanding the effect of inter-jet spacing on lift-off length and ignition delay, *Combustion and Flame* 230 (2021) 111423. doi:10.1016/j.combustflame.2021.111423.

- [138] R. K. Lyon, J. A. Cole, J. C. Kramlich, S. L. Chen, The selective reduction of SO₃ to SO₂ and the oxidation of NO to NO₂ by methanol, *Combustion and Flame* 81 (1) (1990) 30–39. doi:10.1016/0010-2180(90)90067-2.
- [139] M. Hori, N. Matsunaga, N. Marinov, P. William, W. Charles, An experimental and kinetic calculation of the promotion effect of hydrocarbons on the NO-NO₂ conversion in a flow reactor, *Symposium (International) on Combustion* 27 (1) (1998) 389–396. doi:10.1016/S0082-0784(98)80427-X.
- [140] T. Faravelli, Kinetic modeling of the interactions between NO and hydrocarbons in the oxidation of hydrocarbons at low temperatures, *Combustion and Flame* 132 (1-2) (2003) 188–207. doi:10.1016/S0010-2180(02)00437-6.

Appendices

A Engineering Correlation on Liquid Lengths of Arbitrary Fuels

The correlation presented by Higgins et al. [23] estimates liquid lengths of arbitrary fuels. While absolute values of liquid lengths will depend on various and often unknown parameters (e.g. nozzle parameters), the correlation enables the comparison of different fuels. The ratio of liquid length to nozzle diameter is defined as follows:

$$\frac{L_{\text{liq}}}{d_0} = k A^\alpha B^\beta, \quad (\text{A.1})$$

where k is a constant depending, e.g. on the injector. The parameter A is the ratio of fuel density to in-cylinder air density:

$$A = \frac{\rho_f}{\rho_a}. \quad (\text{A.2})$$

The parameter B includes effects resulting from the amount of air necessary to vaporize the fuel:

$$B = \frac{c_{p,f,\text{liq}}(T_b - T_f) + h_{\text{vap}}}{c_{p,a}(T_a - T_b)}, \quad (\text{A.3})$$

where $c_{p,\text{liq}}$ is the specific heat at constant pressure, T_b the boiling point temperature, T_f the initial fuel temperature, h_{vap} the latent heat of vaporization of the fuel and T_a the temperature of the in-cylinder gases. Higgins uses

the physical properties at ambient temperature and pressure for the correlation. However, as ammonia is not liquid at ambient conditions, the physical properties of ammonia are taken from the NIST database [18] at ambient temperature and 10 bar. The used physical properties are listed in Table A.1. Air properties are listed in Table A.2 and correspond to OP4 (920 K, 125 bar). Additional model parameters are listed in Table A.2.

Table A.1: Physical properties of ammonia (293 K, 10 bar), diesel (293 K, 1 bar), methanol (293 K, 1 bar). Properties from [18, 19, 22, 23].

Parameters	Ammonia	Diesel	Methanol
h_{vap} [kJ/kg]	1166	256	1101
T_b [K]	298	576	338
ρ_f [kg/m ³]	610	870	792
$c_{p,f,\text{liq}}$ [J/kgK]	4742	3197	2504

Table A.2: Physical properties of air at TDC of OP4 [18] and parameters used for the presented engineering correlation [23].

ρ_a [kg/m ³]	47.4
T_a [K]	920
$c_{p,a}$ [J/kgK]	1138
k [–]	10.5
α [–]	0.58
β [–]	0.59
T_f [K]	293

B Fuel Injection Velocity Profiles

In the following, the inputs used for the spray model simulations conducted in Section 9.3 are presented.

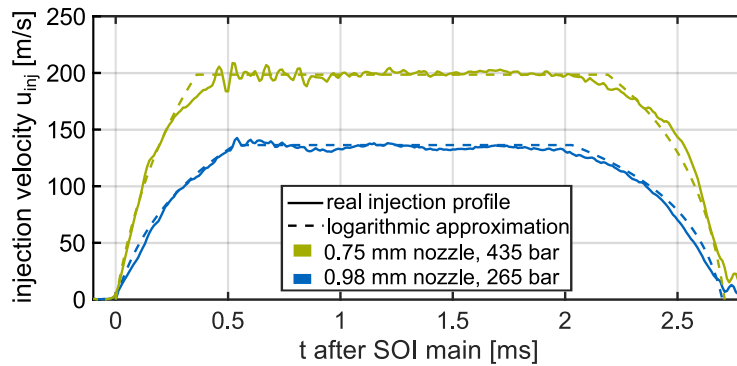


Figure B.1: Approximated injection velocity profiles vs. injection velocity profile from experimental volume flux measurements for the investigations presented in Chapter 9.

Table B.1: 1-D spray model input parameters for the investigations presented in Chapter 9.

Average ambient temperature during injection T_a [K]	915
Average ambient density during injection ρ_a [kg/m ³]	44.5
Fuel density at 265 bar ρ_f [kg/m ³]	630
Fuel density at 435 bar ρ_f [kg/m ³]	641
<u>0.75 mm Nozzle</u>	
Spray angle Θ [°]	24
Absolute injection pressure P_{inj} [bar]	435
Nozzle diameter d [mm]	0.75
Area contraction coefficient C_a [–]	0.81
Discharge coefficient C_d [–]	0.6
<u>0.98 mm Nozzle</u>	
Spray angle Θ [°]	25.5
Absolute injection pressure P_{inj} [bar]	265
Nozzle diameter d [mm]	0.98
Area contraction coefficient C_a [–]	0.81
Discharge coefficient C_d [–]	0.51